

How EEG preprocessing shapes decoding performance

Roman Kessler,^{1*} Alexander Enge,^{1,2} Michael A. Skeide¹

¹ Max Planck Institute for Human Cognitive and Brain Sciences, Leipzig, Germany.

² Humboldt-Universität zu Berlin, Berlin, Germany.

* Corresponding author. Email: rkesslerx@gmail.com

Abstract

EEG preprocessing varies widely between studies, but its impact on classification performance remains poorly understood. To address this gap, we analyzed seven experiments with 40 participants drawn from the public *ERP CORE* dataset. We systematically varied key preprocessing steps, such as filtering, referencing, baseline interval, detrending, and multiple artifact correction steps. Then we performed trial-wise binary classification (i.e., decoding) using neural networks (*EEGNet*), or time-resolved logistic regressions. Our findings demonstrate that preprocessing choices influenced decoding performance considerably. All artifact correction steps reduced decoding performance across experiments and models, while higher high-pass filter cutoffs consistently increased decoding performance. For *EEGNet*, baseline correction further increased decoding performance, and for time-resolved classifiers, linear detrending, and lower low-pass filter cutoffs increased decoding performance. The influence of other preprocessing choices was specific for each experiment or event-related potential component. The current results underline the importance of carefully selecting preprocessing steps for EEG-based decoding. While uncorrected artifacts may increase decoding performance, this comes at the expense of interpretability and model validity, as the model may exploit structured noise rather than the neural signal.

Introduction

The application of classification models to neural data – known as decoding – has become a standard technique in neurosciences including electroencephalography (EEG) research. Unlike univariate approaches, decoding takes advantage of the multidimensionality of the data, facilitating the exploration of basic and translational research questions or the deployment of brain-computer interfaces (BCI). In basic research, decoding can serve as a tool to increase sensitivity¹, to reduce the multidimensional space spanned by electrode voltages to infer the neural representational space and to quantify how cognitive states, perceptual features, or task conditions are reflected in patterns of brain activity over time and space^{2,3}. Translational research uses decoding to better understand individual risk or disease patterns⁴ or to mediate relationships between therapy and clinical outcome⁵. On the other hand, BCI studies aim to maximize decoding performance allowing a user or patient to control a machine or to communicate with the environment^{6,7}.

Although maximizing decoding performance may not always be the primary goal of a study, it is to some degrees important in contexts known to compromise data quality, such as developmental or patient research where motion is common. However, steps to improve decodability must not sacrifice the interpretability and practical utility of the model. Maximizing decodability can be realized at several levels, such as the experimental design, data acquisition, data preprocessing, or the choice of the decoding framework. In the present study, our aim was to illustrate how certain preprocessing choices applied to data derived from common EEG experimental paradigms can increase or decrease decoding performance.

This research question can be addressed in several ways. For example, a many-teams approach⁸⁻¹¹ can examine the analysis strategies of multiple researchers tackling a set of fixed research questions. Each team thus contributes one analysis pipeline. On the other hand, using a multiverse approach^{12,13} one single team contributes many possible pipelines. Unlike a many-teams approach that samples an educated subset of individual preprocessing pipelines (i.e., forking paths) from the community, a multiverse approach allows for a grid search over all possible forking paths by systematically varying each predefined preprocessing step. The multiverse approach is not limited to preprocessing pipelines. It can be applied to any analysis step in a study, such as statistical modeling or the selection of a decoder architecture^{14,15}.

Similar to previous studies^{12,13}, we constructed a multiverse for EEG preprocessing (Fig. 1). We systematically varied ocular and muscle artifact correction using independent component analysis (ICA), low-pass filter (LPF), high-pass filter (HPF), reference, detrending, baseline interval, and the usage of autoreject^{16,17} for artifact rejection. In contrast to previous multiverse studies, we did not examine the impact of preprocessing on event-related potential (ERP) amplitude but on decoding performance. To this end, we analyzed several openly available EEG experiments¹⁸ with classifiers derived from two frameworks. First, we used a neural network-based classifier (EEGNet)¹⁹, that extracts temporal and spatial features for each entire trial to predict the experimental condition, i.e., stimulus or response. Second, we used time-resolved logistic regression classifiers^{20,21}, that use the electrode signals at each time point in isolation to predict the experimental condition.

Our results demonstrate how preprocessing steps influence decoding performance. Narrow filters increased the decoding performance, especially in a time-resolved framework. In contrast, artifact correction steps generally decreased the decoding performance. We discuss promises and pitfalls in EEG preprocessing with respect to decoding analyses.

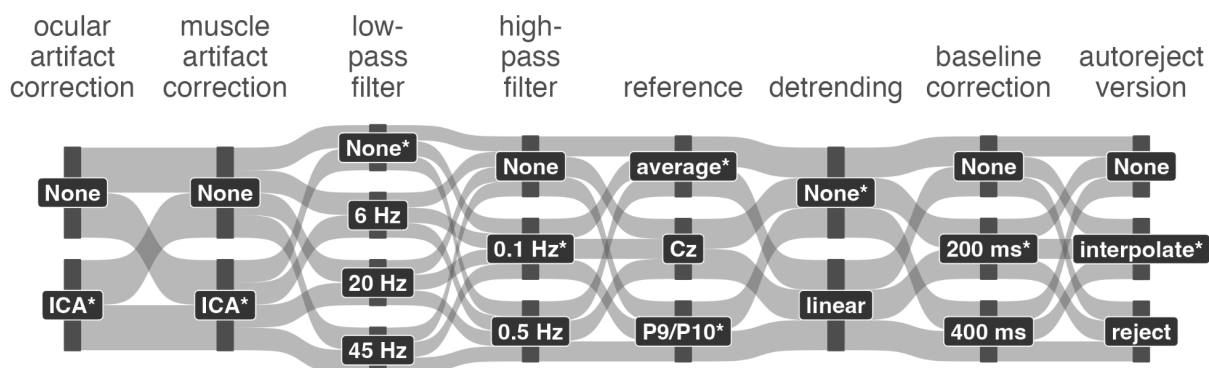


Fig. 1. The multiverse of preprocessing choices. By systematically varying each preprocessing step, the raw data was replicated 2592 times to be preprocessed in unique forking paths. The asterisks indicate processing choices of an *example forking path* used for some analyses, in which the N170 experiment was re-referenced to the average, and all other experiments were re-referenced to P9/P10.

Results

Evoked responses

Grand average evoked responses were computed for each experiment of the *ERP CORE* dataset (Fig. 2) using one example forking path, i.e., one particular preprocessing pipeline (Fig. 1). The time courses of the components closely followed the results of the original study (see ¹⁸ and their Figure 2), despite differences in preprocessing, the inclusion of all participants, and the lack of manual intervention throughout the preprocessing. The components differed in amplitude between experiments. The error-related negativity (ERN) and N400 showed the largest amplitudes, whereas lateralized readiness potential (LRP), mismatch negativity (MMN), and N2pc showed rather small amplitudes. Furthermore, the shapes of the components differed, with N400 and P3 covering large time intervals, while, N2pc for example covered only a short time interval.

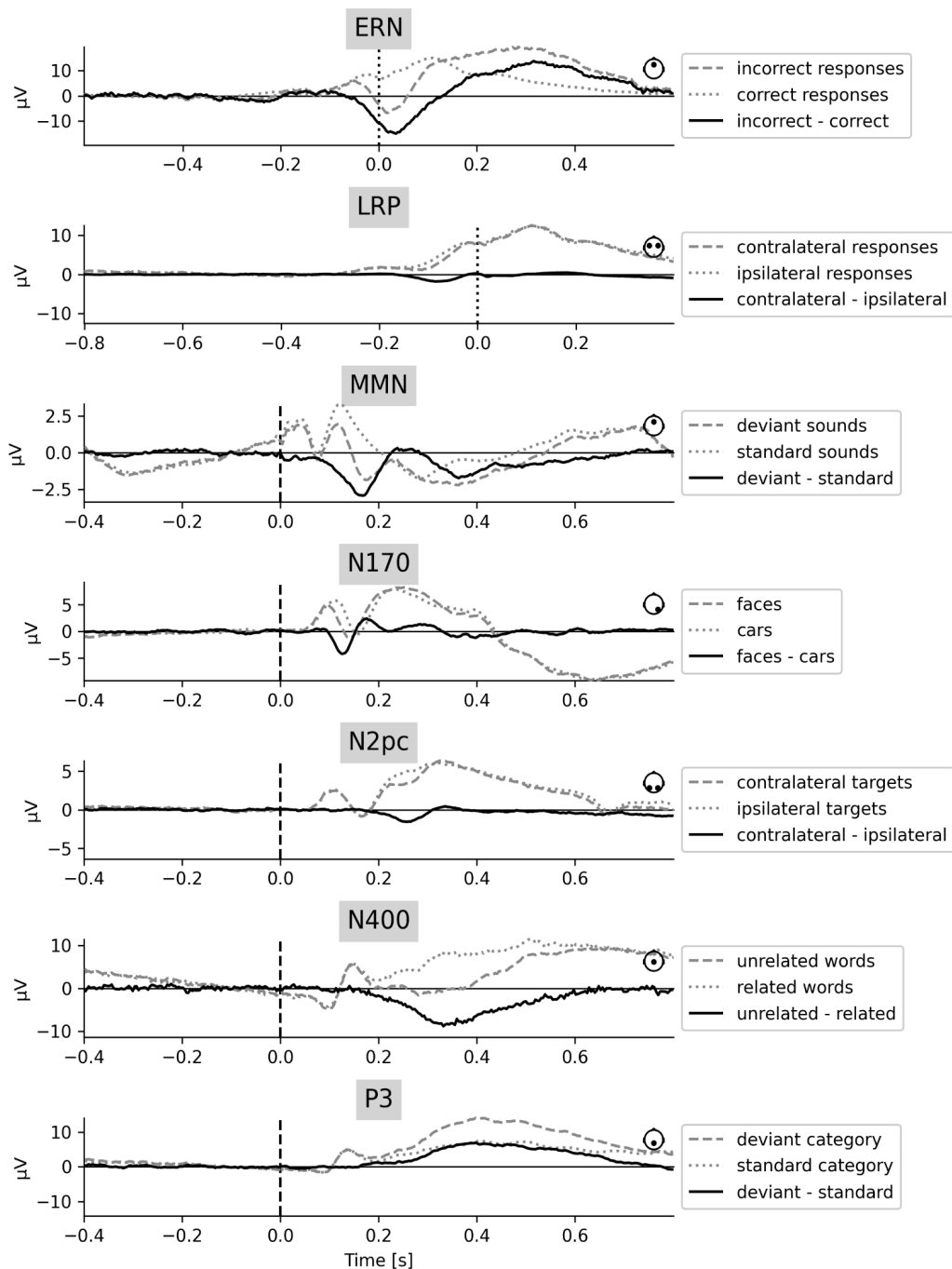


Fig. 2. Grand average evoked responses for each experiment. The data from one example forking path (Fig. 1) were used. The dashed and dotted time courses

represent the average responses to each stimulus category. The solid time course represents the difference between the respective categories, illustrating the respective ERPs. Time series originate either from a single channel, or from two channels, in which case the mean was calculated. The channel positions are indicated by small graphical legends on the right of each plot. Dotted vertical lines indicate response onset (ERN, LRP), and dashed vertical lines indicate stimulus onset (other experiments). Note that the y-axes are scaled differently for each experiment.

Decoding performance

Decoding was performed separately for each forking path using a neural-network based approach (EEGNet) and a time-resolved approach using logistic regression. For EEGNet, we quantified the (balanced) test accuracies of each forking path – averaged across participants – as a measure of decoding performance (Fig. 3A). For time-resolved decoding, we quantified T -sums across participants but within a forking path as a measure of decoding performance (Fig. 3B). Different decoding performances across experiments were observed, with the conditions in ERN being easiest to decode with a median accuracy of roughly 0.85, followed by LRP, followed by all others, and lastly MMN with a median accuracy of roughly 0.57. The ranking of the decoding performances was similar for the neural network-based and the time-resolved approaches. When the time-resolved decoding performance was quantified using the average decoding accuracy over a time window instead of the T -sum (fig. S1), the ranking of the experiments remained similar.

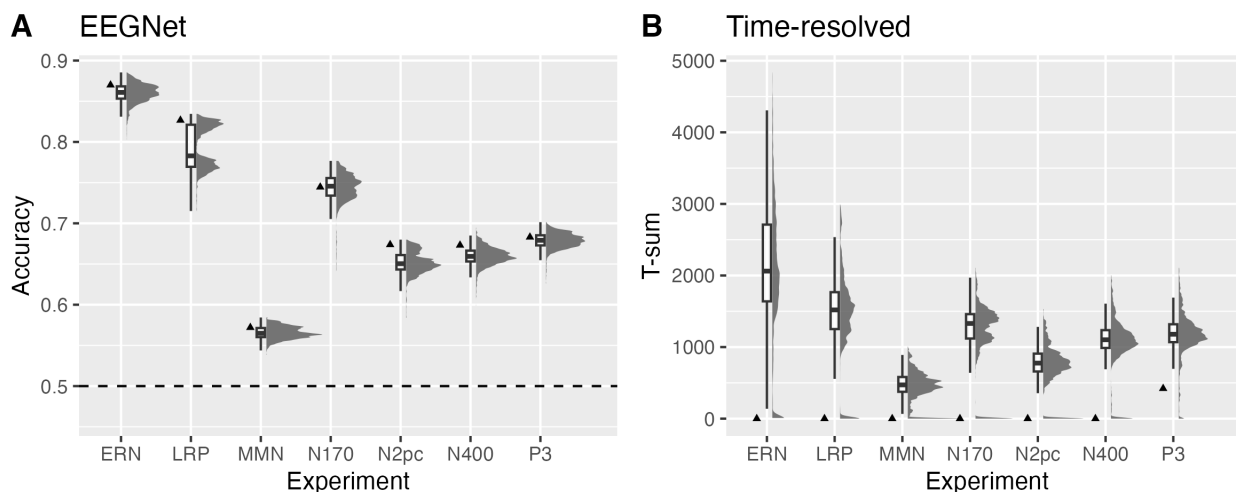


Fig. 3. Overview of decoding performances. (A) EEGNet: (Balanced) Decoding accuracies (y-axis) are plotted for each forking path, averaged across participants, separately for each experiment (x-axis). (B) Time-resolved: T -sums (y-axis) are plotted for each forking path and across participants, separately for each experiment (x-axis). Triangles indicate the forking path without preprocessing. Boxes represent the interquartile range (25th to 75th percentile), with the median indicated by a solid black line. Whiskers extend to the most extreme values within 1.5 times the interquartile range from the lower and upper quartiles.

High ERP amplitudes at single electrodes were not necessarily associated with high decoding performance across the scalp. For example, LRP showed a rather low amplitude at the selected electrodes (Fig. 2), while the decoding performance was rather high (Fig. 3). Although the two measures are not directly comparable, high amplitudes and long duration of ERPs at one electrode could still facilitate decoding performance across all electrodes, as the data underlying the ERP are also incorporated into the classifier, especially if the high amplitudes are the result of low variability between trials. Furthermore, the ranking not only depends on the magnitude and extent of a component, but also on characteristics of the experimental design, such as the number of stimulus repetitions. Note that the T -sum values depend on the data sampling rate, which was held constant between experiments. Therefore, the exact values are rather arbitrary.

We marked the forking path without any preprocessing, i.e., no artifact correction, no filtering, no baseline correction or detrending, and a common online reference Cz (Fig. 3), while keeping the implemented data normalization of the respective decoder (c.f. Methods). For EEGNet, the forking path without preprocessing performed well above average, indicating high flexibility regarding the shape of the features. For time-resolved decoding, unprocessed data performed badly, indicating that at least minimal preprocessing is required for decoding.

Figure 4 illustrates the time-resolved decoding performance of all seven experiments for one single forking path (Fig. 1). Decoding time series revealed large significant clusters, often spanning time windows of over 600 ms. Peak decoding accuracies were roughly between 0.55 (MMN) and 0.7 (ERN). The significant decoding clusters tended to span larger time intervals than the ERPs on selected channels (Fig. 2). Note that exact cluster on- and offsets are not interpretable using the performed cluster mass test²², as compared to a cluster depth test²³.

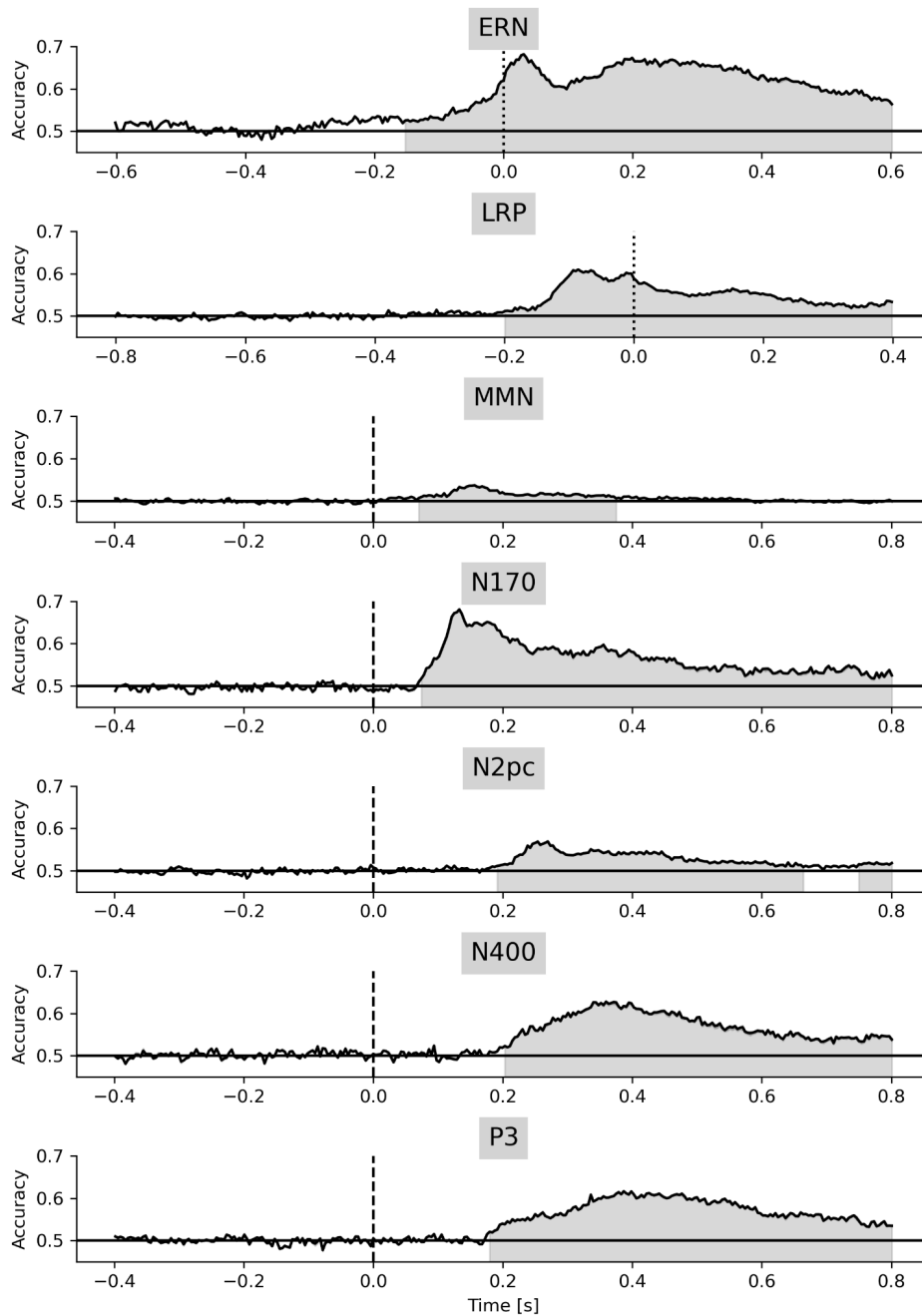


Fig. 4. Time-resolved decoding accuracy for one forking path. (Balanced) Decoding accuracies are illustrated on the y-axis for each time point (x-axis). The horizontal black line represents chance level. One example forking path was used per experiment (Fig. 1). Decoding was performed within each participant, but the decoding time series were averaged across participants. Different experiments are separated in vertical panels. Dotted vertical lines indicate response onset (ERN, LRP), and dashed vertical lines indicate stimulus onset (remaining experiments). Permutation cluster mass tests with a family-wise error rate correction at $\alpha = 0.05$ were performed for each experiment (shaded areas).

Influence of preprocessing choices

For each experiment, we constructed separate linear mixed models (LMMs) using EEGNet decoding accuracies or linear models (LMs) for T -sums derived from time-resolved decoding, describing the decoding performance as a function of all preprocessing steps. One model was fitted per decoding framework and experiment, resulting in seven separate LMMs (EEGNet) and seven separate LMs (time-resolved). Within each model, we then estimated the marginal means for each preprocessing step, i.e., the influence of each choice for a given step on the decoding performance, marginalizing out all other steps. Figure 5 illustrates the marginal means of the main effects for all experiments, both types of decoding models, and for all possible variations of each preprocessing step. The influence – in percent deviation from the marginal mean – of the preprocessing choice on the decoding performance is larger in the time-resolved analysis than in the EEGNet analysis. This is partly due to the deployed T -sum metric and the fact that the time-resolved analysis is performed across participants. See figure S2 for results using average accuracies over time and LMMs for time-resolved decoding.

The impact of most processing steps followed the same direction across experiments (Fig. 5). For example, using artifact correction steps such as ICA or the autoreject package decreased decoding performance in most experiments and decoding frameworks. Furthermore, a high HPF yielded the best decoding performances across experiments and decoding frameworks. In the time-resolved framework, a low LPF further increased decoding performance, while no such trend was observed in the EEGNet framework. The choice of a reference maximizing performance varied between experiments and model types, but its influence was rather weak compared to other preprocessing steps. Linear detrending had a rather positive effect on decoding performance for most experiments and decoding frameworks. Furthermore, a longer time window for baseline correction was beneficial for decoding performance in most experiments. Tables S1 & S2 illustrate results of omnibus F -tests for all preprocessing steps, experiments, and model types. In addition, tables S3 & S4 illustrate the significant pairwise post-hoc tests between factor levels of the main effects.

Two peculiarities emerged, particularly pronounced for EEGNet (Fig. 5A). First, the removal of ocular artifacts was strongly negatively associated with decoding performance in the N2pc experiment. In this experiment, eye movements are expected since the participants might perform involuntary saccades into the visual hemifield of the target, and the target position was decoded (Table 1). Therefore, ocular artifacts are expected to be systematically associated with the class label and thus predictive for the decoder. Accordingly, removing these artifacts reduced decoding performance. Second, removing muscle artifacts was negatively associated with decoding performance, especially in the LRP experiment. In this experiment, left and right hand button presses were decoded (Table 1), and thus systematically different muscle artifacts are expected for the two conditions. These artifacts were predictive and therefore removing them decreased decoding performance.

Further, we analyzed the impact of changing one single preprocessing option at a time compared to the example forking path (Fig. 1) on decoding performance. Figure S3 illustrates, that for most experiments, leaving out artifact correction steps (ICAs, autoreject) increased decoding performance. Similarly, the 6 Hz LPFs increased decoding performance in time-resolved decoding. For the other preprocessing steps, a change

compared to the reference forking path has different consequences for each experiment. The comparison gives insights only in how a punctual substitution of one (but not more) preprocessing step in the reference forking path impacts decoding performance, and is therefore highly dependent on the reference forking path, which in turn varies largely across researchers²⁴. To allow for a simple comparison of individual preprocessing pipelines and their impact on decoding performance, we deployed an online dashboard at <https://multiverse.streamlit.app>.

We ranked all forking paths based on their average decoding performance across participants from best (#1) to worst (#2592), separately for each decoding framework and experiment. Figure S4 & S5 illustrate the individual preprocessing choices of the performance-ranked forking paths and provide more detail on the data points of Figure 3. It turns out that in many experiments analyzed with EEGNet, the forking paths with highest decoding performance did not include muscle artifact correction. Especially in LRP this effect explains the bimodal distributions seen in Figure 3 by suggesting that all forking paths using muscle artifact correction were ranked lower. Furthermore, for EEGNet the forking paths including autoreject showed lower decoding performance. For N2pc, the forking paths with highest decoding performance did not include ocular artifact correction. For time-resolved decoding, a positive effect of detrending and baseline correction on decoding performance was observed in most experiments.

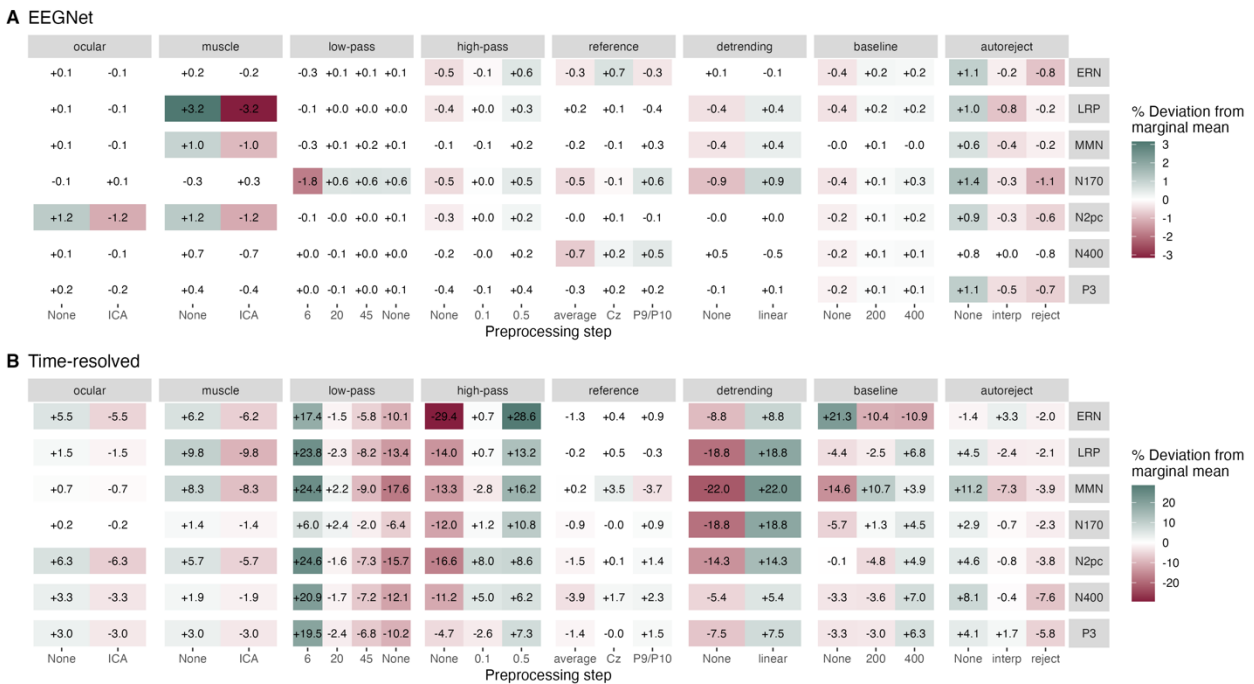


Fig. 5. Influence of preprocessing steps on decoding performance. Percentage deviation from marginal means of either decoding accuracy (EEGNet, **A**) or T -sum (time-resolved, **B**) are depicted within each tile. Marginal means for each level (x-axis) of preprocessing step (horizontal panels) are normalized to the mean of the respective experiment (vertical panels). Each tile therefore shows the percentage differences in relation to this mean value. Only steps with a significant F -test ($p < 0.05$) are colored. Color scales differ in **A** and **B**. *Ocular*: ocular artifact correction; *muscle*: muscle artifact correction; *ICA*: independent component analysis, *low-pass*: low-pass filter in Hertz; *high-pass*: high-pass filter in Hertz;

baseline: baseline interval in milliseconds; *autoreject* version either interpolate (*interp*) or reject artifact-contaminated trials (*reject*).

Interactions between preprocessing choices

We also analyzed two-way interactions between the preprocessing steps. Figure 6 illustrates the interactions related to the N170 experiment within the EEGNet framework as an example. Due to a considerable amount of combinations of experiments and decoding frameworks, we illustrate the remaining interaction results in the Supplements (fig. S6–S18).

Strong interactions can be observed between HPF and detrending (Fig. 6). In many experiments, applying linear detrending made the choice of the HPF less important, i.e., neutralized an adverse choice regarding the HPF cutoff (tables S1 & S2, fig. S6–S18). Similarly, for N170 and other experiments, a combination of neither applying HPF nor baseline correction had negative effects on decoding performance.

Several effects can be observed when using autoreject in the *reject* version, in which noise-contaminated trials were discarded rather than interpolated (c.f. Methods). Decoding performance was lower when autoreject was used, but either HPF, linear detrending, or baseline correction were omitted (Fig. 6, S4 & S5). Presumably, the high electrode voltages – likely present when none of these steps were applied – led to the rejection of many trials, and thus fewer trials were available for model training.

Two pronounced interactions were detected for time-resolved decoding. First, there was an interaction between detrending and baseline correction, with detrending being critical when baseline correction was avoided (fig. S12–S18). Second, although higher-order interactions were not included in the models, forking paths which included neither baseline correction, detrending, nor HPF showed the lowest decoding performance (figs. S4 & S5). Tables S1 & S2 and the corresponding Figures 6 & S6–S18 illustrate all interaction effects for the other experiments and decoding frameworks. Some interactions were common across experiments, while others could only be observed in single experiments.

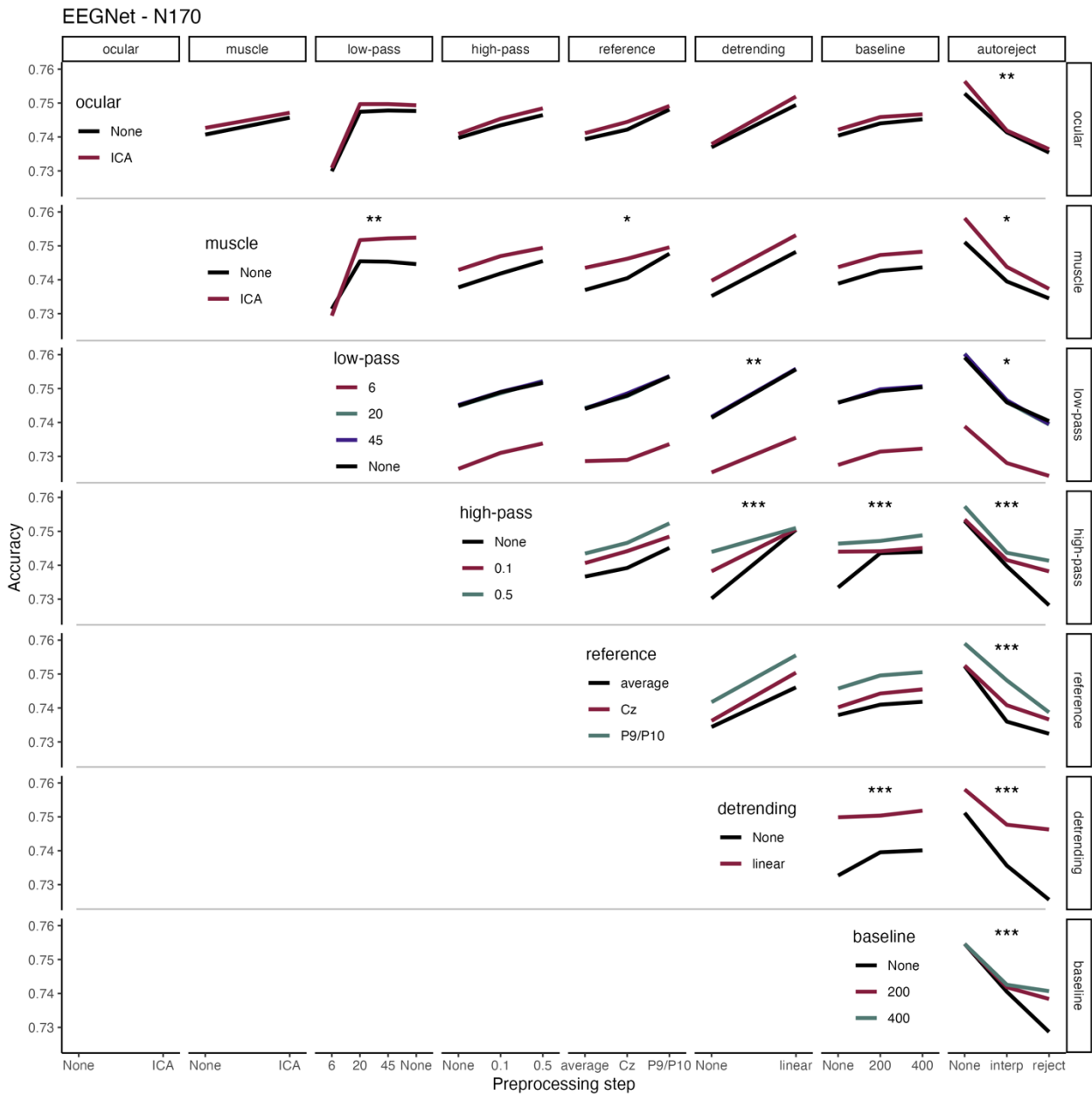


Fig. 6. Interactions between preprocessing steps on decoding performance for the N170 experiment and EEGNet decoding. Horizontal and vertical panels illustrate the different preprocessing steps. The individual preprocessing choices are illustrated on the x-axes and color-coded. The color legends on the diagonal refer to each horizontal panel. (Balanced) Decoding accuracies are shown on the y-axes. Stars indicate the significance (* $p < 0.05$; ** $p < 0.01$; *** $p < 0.001$). *Ocular*: ocular artifact correction; *muscle*: muscle artifact correction; *ICA*: independent component analysis, *low-pass*: low-pass filter in Hertz; *high-pass*: high-pass filter in Hertz; *baseline*: baseline interval in milliseconds; *autoreject* version either interpolate (*interp*) or reject artifact-contaminated trials (*reject*).

Significant clusters in time-resolved decoding

Decoding time series for each forking path and experiment were also visualized individually and ordered according to the total T -sum. Figure S19 illustrates the decoding

accuracy for each time point that fell within a significant cluster. The peak decoding accuracies were mainly in a similar time window and at a similar amplitude, regardless of the forking path. In most experiments, the extent of the significant clusters remained largely similar for the roughly 90 % highest-ranked forking paths (fig. S19). The significant time windows narrowed down or vanished completely for the 10 % lowest-ranked forking paths. Most of the forking paths revealed time windows in which conditions were decoded significantly.

Some decoding time series, especially those corresponding to the higher-ranking forking paths, showed significant clusters extending into the baseline time window, resulting in a baseline artifact. While a certain percentage of false positives was expected across all forking paths in each experiment, some experiments exhibited a higher amount of spurious decodability, extending into baseline periods. Note that one third of forking paths did not use baseline correction (Fig. 1).

We compared forking paths with and without baseline artifact, and scrutinized the distinctive preprocessing steps of these forking paths. Therefore, we defined baseline artifacts as significant clusters extending into the baseline period (table S5). Figure S20 illustrates how many forking paths including a particular version of a preprocessing step led to a baseline artifact in the respective experiment. It turns out that experiments with large ERP components (see Fig. 2) such as ERN, N400, and P3 were more likely to show baseline artifacts. For most experiments linear detrending facilitated a baseline artifact (fig. S20). A low LPF (6 Hz), omitting baseline correction, and in some cases a high HPF (0.5 Hz), increased the likelihood of a baseline artifact (fig. S20). Artifact rejection steps tended to decrease the probability of a baseline artifact in most experiments (fig. S20), highlighting the importance of artifact rejection in rendering the decoding results based on neural signals rather than physiological artifacts. One likely contributor to baseline are the non-causal filters used in the present study, which allow the signal to affect earlier time points²⁵.

Influence of the participant

To demonstrate the variability of EEGNet decoding performance across forking paths (Fig. 3A), we averaged across participants to be consistent with Figure 3B, since the T -sums presented there were calculated across participants. Without averaging, the variability in accuracy was considerably increased, highlighting a large effect of the participant on decoding accuracy compared to the effect of the forking path (fig. S21). The remaining variation in decoding performance in each experiment in Figure 3 can be attributed to the choice of the forking path.

We further analyzed whether decoding performance was associated with participant demographics, but did not find an association between age, sex, or handedness and participant-specific decoding performance according to the LMMs' random intercepts (fig. S22 & S23, Supplementary Text – Influence of the participant in the LMMs). In addition, we correlated the participant-specific random intercepts across experiments, but we only found a significant linear correlation ($r = 0.52$, $p = 0.011$, false discovery rate-corrected) between LRP and N170 in the EEGNet framework (fig. S24 & S25). While the participant's influence on decoding performance is substantial within individual experiments, there is no consistent evidence that the same participant achieves higher decoding performance across multiple paradigms. This aligns nicely with a previous

study, in which a different neural network decoder and a single forking path was used on the very same data set²⁶.

Discussion

In this study, we investigated the influence of EEG preprocessing steps on decoding performance in two different decoding frameworks. For the neural network-based framework (EEGNet), we compared test accuracies of models fitted to differently preprocessed epochs. For the time-resolved framework, we computed cluster-based permutation statistics on the decoding time series across participants for differently preprocessed epochs and quantified decoding performance as the T -sum of the significant clusters. We analyzed seven different experiments separately and modeled the classifier performance as a function of all preprocessing steps.

The results demonstrated, that above chance-level decoding was feasible with most forking paths. For EEGNet, high HPF cutoffs and baseline correction facilitated decoding. For time-resolved classifiers, linear detrending, low LPF cutoffs, and high HPF cutoffs increased decoding performance. All artifact correction steps reduced decoding performance for all experiments and decoding frameworks, likely by removing artifacts that covaried with the experimental condition, but potentially also by removing portions of the neural signal of interest²⁷. Hence, focusing on decoding performance alone is not sufficient to decide on a preprocessing pipeline, but requires further investigation in the light of neural signal versus noise. We also found detrimental combinations of processing steps that decreased decoding performance substantially.

Artifacts spuriously enhance decoding performance

Most artifact corrections led to a decrease in decoding performance. This decrease was particularly pronounced in experiments where artifacts can be expected to covary with stimulus categories, such as ocular artifacts in a visual search task and muscle artifacts in a keystroke task. Despite the decrease in performance, removing artifacts should be of interest when model features are to be interpreted spatially or temporally, such as could be done by means of Shapley values²⁸ or by visualizing weight vectors²⁹. However, removing artifacts may also remove the neural signal of interest²⁷, especially when using the threshold-based ICA employed in the present study. Future studies should further disentangle the influence of artifact correction steps into the unique contribution of the removed artifacts versus unintentionally removed neural signal. In some BCI use cases in which the source of the signal may be less relevant, an analyst may even refrain from removing predictive artifacts.

Compared to classical ERP analysis, decoding uses all channels and time points simultaneously to infer differences between conditions¹. This can lead to a situation in which certain artifacts, while less problematic for ERP analyses in a region of interest, may drive whole-brain decoding and thus inadvertently imply stimulus-related differences. BCI studies have also suggested a drop in decoding performance when various artifact correction methods were applied^{30,31}.

Narrow filtering yields high performance

Filter cutoffs also play an important role for decoding performance. Models using data filtered with high HPF and low LPF cutoffs ranked highest in all experiments using time-resolved decoding. This finding supports using a low LPF cutoff to exclude alpha activity, an influential source of trial-to-trial variability³². However, a low LPF cutoff may inflate the time window of an ERP and thus preclude the interpretation of its timing³³. The same should hold for the temporal interpretation of decoding accuracies. On the other hand, a LPF could partially mitigate a missing muscle artifact rejection step, since muscle artifacts are largely distributed in a frequency spectrum above 15 Hz³⁴.

A high HPF cutoff increased decoding performance in both decoding frameworks. HPFs are important for leveling the signal of each epoch, especially when baseline correction has not been performed. However, HPF cutoffs above approximately 0.3 Hz also come at a cost, introducing artifacts of opposite polarity before and after the ERP³⁵, which in turn compromise the temporal interpretation of decoding performance. Designing more specified filters can decrease such artifacts²⁵, including some of the baseline artifacts seen in the current study. In particular, the use of non-causal filters allows the signal to leak into preceding time points, increasing the likelihood of a baseline artifact. Linear detrending was also positively associated with decoding performance, especially for time-resolved decoding. Before classifier training, the voltage values at each time point and channel were standardized across trials for time-resolved decoding. Random drifts in some electrodes and trials may generate relatively large values – especially at epoch margins – obscuring potentially predictive values of other epochs situated at a much smaller scale at the same electrodes and time points. Only few other decoding studies also removed these remaining drifts from the epochs (e.g., ³⁶).

Detrimental combinations of preprocessing steps

Unlike previous studies^{12,13}, we also allowed for interactions between preprocessing choices. The most common interactions across experiments and decoding frameworks were found between preprocessing steps that level the signal of an epoch to a common range. These include HPF, detrending, and baseline correction. Combining different versions of these steps that do not level the signal to a similar range, i.e., no HPF, no detrending, and no baseline correction, tended to reduce decoding accuracy. Not leveling the signal by means of these preprocessing steps also led to high trial dropout rates when using autoreject.

Furthermore, spurious decodability in baseline periods was observed in many forking paths, leveraged by detrending, a low LPF, a high HPF, or the avoidance of baseline correction. Another study also demonstrated spurious baseline decodability by the combination of a high HPF, baseline correction, and avoidance of robust detrending³⁷. Such effect may also be present in the EEGNet approach, as the baseline was also included in the training of the classifier. We would therefore suggest to also decode from the baseline in the time-resolved framework – and visualize baseline decodability – for the sake of detecting such artifacts. If the baseline period is not decoded in the time-resolved framework, spurious baseline decodability and the likely associated modification in the to-be-interpreted window of the decoding time series might evade detection. Artifact correction steps however decreased the likelihood of baseline artifacts.

'Optimal' preprocessing differs for ERPs and decoding

Previous studies using multiverse-like preprocessing have mainly focused on 'optimal' preprocessing with respect to ERP characteristics such as amplitude. Since one cannot directly distinguish between neural signal and artifacts covarying with the experimental condition, focusing on maximizing amplitude (or similar) has similar limitations as focusing on decoding performance (accuracy or T -sum) alone. Results from multiverse studies need to be enriched with considerations about the origin of the signal, the side effects of individual processing steps in general, and domain knowledge about the processes under investigation. However, multiverse analyses on single outcome metrics are a helpful step towards a better understanding of the impact of preprocessing and, among other possibilities, facilitate the comparison of different study results. The following is a comparison of how different the effects of preprocessing can be on ERP-related measures versus decoding performance.

For example, a study by Delorme³⁸ compared preprocessing pipelines and their influence on the number of significant channels between two conditions in three paradigms (Go/No-go task, face perception task, & active auditory oddball task with button press). Their optimal pipeline was dependent on the software used for preprocessing but mainly comprised a HPF and bad channel interpolation. Other steps either reduced or increased the number of significant channels or did not show any effect. While their study tested a wider range of artifact correction techniques, the different directions of effects on the number of significant channels in the analyzed experiments make comparison more challenging. In our experiments artifact correction rather decreased the decoding performance. Both studies however align on the use of HPFs, as in all datasets, higher HPFs increased the number of significant channels or decoding performance. .

A study by Clayson et al.¹³ employed a multiverse to compare the influence of preprocessing on ERP amplitude for two components, ERN and error-related positivity (Pe), using the Eriksen flanker task³⁹. For ERN, their optimal processing consisted of a 15 Hz LPF and ocular artifact correction with ICA. For Pe, however, their optimal processing in terms of ERP amplitude included a 30 Hz LPF, a 0.1 Hz HPF, and regression-based ocular artifact correction. Our time window for decoding in the ERN experiment spanned the time windows of both components. We however defined a stimulus-locked rather than a response-locked baseline window⁴⁰. In our search space, the optimal LPF cutoff was at 6 Hz for time-resolved decoding. In contrast, for the neural network-based framework, all higher LPF cutoffs (≥ 20 Hz) were equally suitable for decoding. We found the optimal HPF cutoff to be around 0.5 Hz in both of our decoding frameworks, while Clayson et al. did not test beyond 0.1 Hz. Ocular artifact correction played a minor role in decoding, but avoiding this step still resulted in higher decoding performance in our data. While they found a mastoid reference to be beneficial for ERN amplitude compared to an average reference, we did not find a significant improvement (Table S3). However, we found that the Cz reference increased decoding performance (Figure 5, Table S3). Because Cz is close to FCz, which itself shows high ERN amplitude (Fig. 2, Table 1),^{13,18}, subtracting Cz from the remaining electrodes likely injects this signal into the other channels, again limiting potential downstream interpretability of the model weights.

Šoškić et al.¹² analyzed the influence of preprocessing on the effect magnitude in an N400 experiment. The largest effect was obtained with a HPF between 0.01 Hz and 0.1 Hz

(compared to 1 Hz) and a mastoid reference (compared to an average reference). We found the same optimal reference for decoding in the N400 experiment for both neural network-based and time-resolved decoding. However, we found that higher HPFs between 0.1 Hz and 0.5 Hz led to higher accuracies.

Generalizability of the insights from the multiverse

Some of the observed effects of preprocessing on decoding performance were generalizable across experiments, such as the LPF cutoff (time-resolved), baseline correction (EEGNet), or detrending (time-resolved). Some effects were even generalizable across decoding frameworks, such as the HPF cutoffs, or the drop of decoding accuracy by artifact correction steps.

The generalizability of the results to different decoding frameworks remains to be demonstrated in the future. We deliberately used two different decoding frameworks to show similarities and differences regarding the influence of preprocessing using multiverse analyses. However, even changing the decoding model – e.g., to support vector machines in a time-resolved framework, or to different neural networks instead of EEGNet – could change the multiverse results. Decoder hyperparameter optimization may also change the optimal preprocessing choices, but this topic is beyond the scope of the current study. Instead, we used default hyperparameters. Decoder hyperparameter optimization could be added to the multiverse, as could the choice of the decoding model itself be added. One could even treat the multiverse for preprocessing as a kind of grid search-like hyperparameter optimization, if cross-validated and applied to independent test data.

The experiments used in the present study were tailored to ERP-related research questions. ERPs have marked voltage differences in defined channels and time windows, which are likely to also become predictive in decoding. Moreover, the influence of the forking path might be larger if, for example, the experiments included fewer repetitions per stimulus category. Such an effect has been demonstrated previously, illustrating that artifact correction steps have larger effects when a smaller number of trials is analyzed³². Good decoding performance was expected for the well-replicated effects studied here.

However, different kinds of EEG paradigms need different decoding frameworks. For example, for experiments in which the spectral power differences between conditions are analyzed^{41,42}, a decoding framework tailored to frequency decoding is more suited⁴³. Recent experiments are often based on the rapid serial visual presentation (RSVP) structure⁴⁴⁻⁴⁶, in which many different object categories are presented in quick succession to run a large number of trials per object category. These experiments, also employed in the auditory domain^{47,48}, are not directly designed to find well-described ERPs. Instead, the literature describes ERPs only for a small subset of the contrasts that can be constructed between categories included in an RSVP experiment. For example, faces can usually be easily distinguished from other categories in decoding based on the data underlying the N170, but also information from other channels not typically used in characterizing the N170. However, differences between other categories (e.g., computers and cars) are less well-described. A possible explanation is that the differentiation of these categories had little evolutionary relevance, leading to idiosyncratic representation for each participant rather than a systematic and generalizable representation across participants. More dense electrode coverage might be helpful to find such subtle

differences between categories. From this point of view, the decoding accuracies shown in the present N170 experiment presumably represent the upper limit of decoding accuracies that can be expected from such an RSVP experiment at the given number of stimulus repetitions, due to the strong nature of the N170 component. Other contrasts might lead to classifiers with lower accuracy. Importantly, one should not extrapolate the present recommendations based on the multiverse results regarding the N170 experiment – the only object categorization experiment analyzed in the present study – to an RSVP experiment. The reason is that the preprocessing would then be optimized for the face vs. car contrast, but not for the many other contrasts between categories. In fact, any preprocessing prior to multi-class decoding could bias decodability by filtering out the predictive features of one class represented in a particular frequency spectrum. From this perspective, using the data in a rather raw (i.e., not heavily preprocessed) form might be favorable in this particular context, given that the classifier works well with it.

Finally, the multiverse also illustrates the challenge of analytical variability with regard to preprocessing. Although only a subset of possible forking paths would be practically used by an analyst, the variability is still substantial²⁴, offering an analyst sufficient degrees of freedom. Preregistration should be one important building block to increase transparency and avoid the potential for malpractice^{49,50}.

Inflating the multiverse

The constructed multiverse naturally included only a limited subset of preprocessing steps and variations. One could have added any number of additional variations of each analysis step. For example, one could have sampled the filter cutoffs more densely to find a better optimum, rather than just an optimum based on the available choices. Similarly, the effect on decoding performance of using GLM-based rather than subtraction baseline correction, which has been shown to reduce artifacts in the ERP window, could be investigated^{51,52}. Furthermore, a large number of plausible methods have been published for each preprocessing and artifact correction step, such as regression-based methods for ocular artifact correction⁵³, trial-masked robust detrending³⁷, robust averaging⁵⁴, or the application of pretrained classifiers on independent components⁵⁵, to name a few. For this reason, we have made some simple but reasonable choices for each step that were readily available in the *MNE* package, such as threshold-based ICA for ocular artifact correction. It remains to be seen whether these choices could generalize to similar approaches, other software, and other package versions. For artifact rejection tools that remove the respective artifacts more thoroughly – while not removing neural signal of interest²⁷ – we expect the reported effects to be even stronger.

Besides the exact steps performed, previous studies also vary widely in their order of preprocessing steps⁸. Systematically varying the order of the steps however leads to a combinatorial explosion, complicating both computation and interpretation. Furthermore, the interpretation of interactions between preprocessing steps changes depending on their order. Accordingly, such a study needs to be conducted in the future. We have tested one alternative multiverse with a slightly different order of steps, i.e., (1) re-referencing, (2) HPF & LPF, (3) ocular artifact correction, (4) muscle artifact correction, (5) baseline correction & detrending, and (6) autoreject (fig. S26 & S27, Supplementary Text – Alternative order of preprocessing steps). Most effects were qualitatively similar to those presented in the main manuscript.

A wide variety of preprocessing and artifact correction methods are available from the literature and the EEG community, not all of which can be exhaustively addressed in a single multiverse analysis. However, follow-up studies investigating the influence of particular preprocessing steps against reasonable reference pipelines would allow many of them to be tested in a more computationally efficient manner (e.g., ³⁸), and may provide insight into their impact on decoding performance or feature interpretability.

In summary, the present study systematically varied a wide range of EEG preprocessing steps to evaluate their impact on decoding performance. For EEGNet decoding, high high-pass filter cutoffs and baseline correction increased decoding performance, whereas for time-resolved decoding, high high-pass filter cutoffs, low low-pass filter cutoffs, and linear detrending increased decoding performance. Importantly, all artifact removal steps decreased decoding performance, likely due to covariation between artifacts and experimental condition, effectively reducing the proportion of non-neural features which spuriously enhanced decoding performance. The influence of other preprocessing steps varied depending on the experimental paradigm. We suggest to carefully select EEG preprocessing steps for decoding, as selecting steps that maximize decoding performance is associated with limitations in downstream feature interpretability.

Materials and Methods

Data sets

We used the openly available ERP CORE dataset¹⁸ (<https://osf.io/thsgq/>). 40 participants underwent six different EEG experiments to identify the following seven event-related potential (ERP) components: error-related negativity (ERN), lateralized readiness potential (LRP), auditory oddball-related mismatch negativity (MMN), face-related N170, visual search-related N2pc (N2 posterior-contralateral), semantics-related N400, and visual oddball-related P3¹⁸. ERN and LRP were assessed using the same paradigm analyzed differently. EEG was recorded using 30 scalp electrodes (fig. S28), along with three electrooculogram (EOG) channels, two positioned lateral to the outer canthus of each eye and one below the right eye¹⁸. For details of the experimental design and paradigms, we refer to Kappenman et al.¹⁸. We will only address changes to their processing or aspects that seem important for the purposes of this study or its reproduction. In the remainder of this article, we will refer to these experiments by the names of the corresponding components (e.g., MMN, N170, etc., as shown in Table 1).

Table 1. Properties of the ERP CORE dataset. The experiments are named after the main component, analyzed with the respective paradigm¹⁸. For each experiment, the conditions and channels used to compute and visualize the ERPs are shown, with the second condition being subtracted from the first condition. For decoding, the trials of experiments LRP and N2pc were assigned to different conditions.

experiment/ component	paradigm	conditions		channels evoked
		evoked	decoding	
ERN	Eriksen flanker task ³⁹	incorrect & correct responses	incorrect & correct responses	FCz
LRP	Eriksen flanker task ³⁹	contra- & ipsilateral	left & right responses	C3/C4

		responses		
MMN	passive auditory oddball	deviant & frequent sounds	deviant & frequent sounds	FCz
N170	face perception	faces & cars	faces & cars	PO8
N2pc	visual search	contra- & ipsilateral targets	left & right targets	PO7/PO8
N400	word pair judgment	unrelated & related words	unrelated & related words	CPz
P3	active visual oddball	deviant & frequent category	deviant & frequent category	Pz

Data preparation

Data preprocessing and modeling was done using a high-performance computing cluster of the Max Planck Computing & Data Facility (Garching, Germany). Each experiment was preprocessed using *MNE* (v. 1.6.1)⁵⁶ for Python (v. 3.11.6). Triggers from the raw signal were pruned to retain only relevant events (Table 1). Trials of ERN and LRP were analyzed relative to button press, while all other experiments were analyzed relative to stimulus onset (Table 1). Contrary to Kappenman et al.¹⁸, we used a pre-stimulus instead of a pre-response baseline window in the ERN experiment to minimize systematic differences between conditions in the baseline period⁴⁰.

Decoding was performed using data from all available scalp electrodes, in contrast to ERP analysis, where it is common practice to analyze data from individual electrodes. Hence, conditions relating to hemisphere, i.e., contralateral & ipsilateral hemisphere, cannot be meaningfully integrated into a whole-brain decoding logic. For this reason, we assigned the trials of some experiments into new conditions for decoding. For LRP decoding, trials were sorted into left and right responses. For N2pc decoding, we sorted trials into left and right targets (Table 1).

Stimulus event times were shifted forward by 26 ms to account for the delay of the LCD monitor¹⁸. Data were downsampled from 1024 Hz to 256 Hz. The raw data channels remained in single-ended mode, so no reference was yet applied. The signal from the two horizontal EOG channels was subtracted to form a single horizontal EOG channel⁵⁷. Similarly, the signal from Fp2 was subtracted from the vertical EOG channel, positioned below the right eye, to form a single vertical EOG channel⁵⁷. The data were then temporarily re-referenced to Cz. The final reference electrode was later determined by the respective forking path. These data then entered the multiverse preprocessing.

Multiverse preprocessing

All preprocessing steps were restricted to functions included or closely related to the *MNE* package. Guided by preprocessing steps that were investigated by previous EEG multiverse-like studies^{12,13,38}, we varied ocular artifact correction using ICA, muscle artifact correction using ICA, LPF, HPF, re-referencing, detrending, baseline correction, and artifact correction using autoreject^{16,17}. Figure 1 provides an overview of the different preprocessing steps. A total of 2592 forking paths resulted from the systematic variation

of the chosen preprocessing steps, i.e., the Cartesian product of all preprocessing steps' options. We chose the same preprocessing steps across all datasets, although the literature suggests a different range of preferred settings depending on the shape of the component. Furthermore, we only included steps that did not require manual intervention by an analyst. Manual intervention is practically not feasible in the multiverse setting and is less consistent, therefore limiting reproducibility⁵⁸.

Theoretically, one could extend the multiverse by additional preprocessing options, such as different methods for ocular artifact correction. However, we decided to limit the number of options for all preprocessing steps to keep the computation time within feasible limits. Furthermore, we did not systematically alter the order of the different preprocessing steps, as this would have led to a combinatorial explosion of forking paths. The selected order roughly followed two previous studies^{12,13}, however with ocular and muscle artifact corrections positioned at the beginning to avoid contamination of other preprocessing steps.

For most preprocessing steps, but also for later decoding analysis, we deliberately used the default (hyper-) parameters, if not specified otherwise. Furthermore, we stayed as close as possible at the corresponding tutorials provided from the software packages deployed. In the following passages, we briefly describe the individual preprocessing steps and their variations in the multiverse.

Ocular artifact correction.

In forking paths including ocular artifact correction, threshold-based ICA was performed using the corresponding *MNE* function. First, the raw signal was copied and a 1 Hz⁵⁹ HPF was applied to the copy (see table S6 for filter characteristics). Then an ICA was performed across EEG channels using the *picard* method⁶⁰, setting the maximum number of iterations to 500 and estimating 20 components. The *find_bads_eog* function with default parameters was used to correlate each component with the artificially generated EOG channels. Components were classified as ocular artifact if passing a threshold based on adaptive *z*-scoring. The ICA solution was then applied to the unfiltered data, effectively subtracting the artifact components from the raw signal. It should be noted that recent studies have found evidence of worse ocular artifact correction compared to using lower HPFs, likely due to ocular artifacts below 1 Hz⁶¹. The effects of ocular ICA on decoding performance may be stronger with more thorough ocular artifact correction methods. Similar to other processing steps, we closely followed the respective *MNE* tutorials when implementing ICA. However, there exist more sophisticated approaches that exploit, for instance, pretrained classifiers for component categorization⁵⁵.

Muscle artifact correction.

A similar procedure was deployed to that used for ocular artifact correction, using the *MNE* function *find_bads_muscle*^{62,63}. In short, three criteria were applied to determine if a component represented a muscle artifact^{62,63}, spectral slope, peripherality and spatial smoothness. Because the log-log spectral slope was measured in the range of 7 Hz to 45 Hz, muscle artifact correction was implemented before the LPF. As with ocular artifact correction, the ICA was estimated on a copy of the data filtered at 1 Hz (see table S6 for filter characteristics). The ICA solution was then applied to the unfiltered data to remove artifactual components.

Filtering.

The default filter function of *MNE* was applied to all channels of the raw time series, using a linear FIR filter with cutoffs defined in the respective forking paths (Fig. 1). The filters were one-pass, zero-phase, non-causal band-pass filters (in forking paths with both cutoffs, otherwise HPF or LPF) with a windowed time domain design method (*firwin*), and a Hamming window with 0.0194 passband ripple and 53 dB stopband attenuation. The lower and upper passband edges were defined by the HPF and LPF cutoffs of the respective forking path. Other characteristics were automatically determined by *MNE* using the cutoffs, and are illustrated in table S6 for the different forking paths. 45 Hz was defined as the upper limit for the LPF, since the AC of most countries is typically transmitted at a frequency of 50 Hz to 60 Hz. The LPF of 6 Hz was included to exclude alpha activity³². The HPF cutoffs were motivated by a range commonly used in EEG literature.

Referencing.

The channels of the raw data were re-referenced to either a single channel (Cz), the average of two channels near the mastoids (P9/P10), or the average of all channels (Fig. 1). According to previous studies, the average of P9 and P10 provided cleaner signals than the commonly used mastoids¹⁸. Cz or nearby FCz are often used both as an online reference and as a reference during analysis. For convenience, since some of the ERPs of the currently analyzed experiments use FCz as the channel of interest (Table 1), we deployed Cz as reference option in the multiverse. Finally, the average reference is often used to cancel common mode noise and to have a more intuitive interpretation of the topographic distributions of the signals.

Epoching.

Epochs were created for a time window of 1.2 s for each experiment (table S5). This interval included the same interval as the original study¹⁸. To be able to increase the baseline period in the multiverse, we added 0.2 s at the end for ERN and LRP, or added 0.2 s at the beginning for all other experiments (table S5).

Detrending.

In some forking paths, linear detrending was performed prior to baseline correction. When applied, a linear function with intercept and slope was fitted to each epoch and channel using least squares. The signal was detrended by retaining only the corresponding residuals.

Baseline correction.

Baseline correction was applied in a subset of forking paths by first averaging the predefined baseline window in each channel and epoch. The average was then subtracted from the epoch for the respective channel and epoch. The baseline period varied between forking paths (table S5). If applied, baseline correction was either set to the same 200 ms period for each experiment as in Kappenman et al.¹⁸ (but not for ERN), or extended to 400 ms. Crucially, for some response-locked ERPs such as the ERN, a response-locked baseline window is not optimal, since the conditions (error vs. correct) can already be

represented in pre-response components extending into the baseline⁴⁰. Further, systematic differences in reaction time between the two conditions can lead to overlap with different segments of the preceding stimulus ERPs⁴⁰. For this reason, we adjusted the baseline windows to precede the stimulus instead of the response in the ERN experiment (table S5). Finally, the baseline windows were chosen to end at the same time point within each experiment, resulting in identical post-baseline interval lengths across forking paths (table S5).

Artifact correction using autoreject.

For further artifact correction on the epochs, the *autoreject* package (v. 0.4.3) was used in a subset of forking paths^{16,17} (Fig. 1). In short, the package automatically detects and either rejects or interpolates bad sensors and bad trials based on their peak-to-peak voltages. The rejection thresholds were determined by 5-fold cross-validation. Here we used *autoreject* in two versions. In the *interpolate* version, the *autoreject* hyperparameters were set to values such that all bad sensors were interpolated rather than rejected, ensuring that the resulting number of trials for these forking paths remained identical. The advantage of this approach is, that all trials are kept for later analysis. In the *reject* version, we provided *autoreject* with reasonable hyperparameters for *consensus* (0.2, 0.4, 0.6, 0.8) and *n_interpolate* (4, 8, 16, 32). A grid search was performed to find optimal values^{16,17}. If only a few electrodes exceeded the estimated threshold, they were interpolated by neighboring electrodes. If many electrodes exceeded the threshold, the entire epoch was discarded. We used 25 % of the epochs to fit the *autoreject* model.

While the previous preprocessing steps did not change the number of epochs per condition, the second *autoreject* version could drastically reduce the number of epochs. If a forking path had too few epochs per condition for later cross-validation, the forking path of that participant was discarded. This happened only in rare cases. Note that *autoreject* shows substantial variability in the number of dropped epochs with different random seeds (fig. S29 & S30, Supplementary Text – Variability due to random seed in *autoreject*).

Evoked responses

We computed exemplary grand average evoked responses as a proof of principle to ensure that data processing worked as expected. Therefore, for each experiment, we chose a forking path that was related to the preprocessing reported in the original paper releasing the dataset¹⁸. That is, for all experiments except N170, re-referencing was done on mastoids (average of P9 & P10), with an HPF of 0.1 Hz, and no LPF applied. ICA was used for both ocular and muscle artifact correction, as well as *autoreject* in the *interpolate* version. We chose here to use all artifact correction steps in this example forking path, as the original study performed multiple – including manual – artifact correction steps. The baseline period was 200 ms and no detrending was performed. For N170, re-referencing was done using an average reference. The remaining steps were the same as for the other experiments (Fig. 1).

For LRP and N2pc, channels were combined to obtain signals from channels contralateral and ipsilateral to the target (N2pc) or response (LRP) (Table 1). This aggregation was performed only for visualization of evoked responses in accordance with Kappenman et al.¹⁸, but not for decoding.

Decoding models

We selected a neural network-based and a time-resolved framework for decoding. The former is more commonly used in BCI research¹⁹, whereas the latter is often used in basic research on the time course of category discrimination^{32,64–69}.

Trial-wise decoding using EEGNet.

The neural network-based decoding model employed was EEGNet (v. 4)¹⁹, implemented in the *braindecode* toolbox (v. 0.81)^{43,56}. For each forking path, the preprocessed trials were rescaled using exponential moving standardization. The MMN, P3, and ERN experiments had highly imbalanced classes, while the LRP experiment was only slightly imbalanced. Furthermore, autoreject introduced imbalance when used in the reject version. Therefore, class weights were computed separately for each forking path, experiment, and participant.

Next, the order of the trials was shuffled and a stratified 5-fold cross-validation split was defined. The model was initialized with its default hyperparameters, a batch size of 16, exponential linear unit activation function, a dropout rate of 0.25, a learning rate of 0.01, a stochastic gradient descent optimizer, and a negative log-likelihood loss function. The maximum number of epochs (i.e., training cycles, not electrophysiological epochs) was set to 200. See table S7 for a comprehensive list of hyperparameters, and table S8 for the layer structure. Scoring was performed using balanced accuracy for the 2-class case⁷⁰. Balanced accuracy is the mean of sensitivity and specificity, and is equivalent to accuracy for class-balanced data. For each cross-validation split, the model was fitted to 4/5 of the data and evaluated on the remaining 1/5 of the data. The resulting test accuracies across the 5 splits were averaged. The approach was repeated for each forking path, experiment, and participant.

Time-resolved decoding using logistic regression.

In the literature, raw electrode voltages^{32,67} or averaged pseudo-evoked potentials^{68,69} across trials but for each time point separately are used to train classifiers (fig. S31). In the present study, we used the raw trials for classification. Data of each participant, time point, and channel was standardized individually by removing the mean and scaling to unit variance across trials. As with EEGNet, balanced accuracy was used for scoring, and class weights were computed individually for each forking path, experiment, and participant. A logistic regression estimator (*sklearn* v. 1.3.1) was used with a *liblinear* solver⁷¹, L_2 penalty, $C=1$, tolerance of 0.0001, and a maximum number of iterations of 100, applied to each time point with the *SlidingEstimator* function within *MNE*. See table S9 for a comprehensive list of hyperparameters. Decoding windows corresponded to the entire trial length (including baseline) and were kept equal in length across experiments, but differed in onset and offset (table S5). A stratified 10-fold cross-validation was performed, and the test accuracies were averaged across folds, resulting in one decoding time series for each forking path, experiment, and participant.

The issue of data leakage in EEG decoding.

A topic that is closely monitored in the machine learning community, but often neglected in the neuroscience community, is data leakage^{72,73}. Through data leakage, information

from the test data is introduced into the training data⁷⁴, leading to an overestimation of decoding performance. Recent studies have investigated, how leakage is introduced when decoding is performed across participants without segment-based instead of subject-based holdout sets during cross-validation⁷². However, we are in the context of within-participant decoding. Others have investigated the leakage of test trials into the training data or the leakage of test data into the estimation of data features⁷⁵. In our analyses, we used k-fold cross-validations separating training and test epochs. However, the data were jointly preprocessed, leading to imperfect separation. First, the entire time series is used to estimate the ICA solution, meaning segments later assigned to the test set contribute to the removal of components from both the test and training sets. Second, when applying the HPF, test trials can influence training trials due to proximity in the raw time series. Lastly, autoreject involves both training and test data to jointly estimate hyperparameters and rejection thresholds. While this joint preprocessing does not directly resemble the estimation of predictive features for modeling, there could theoretically still be a nuanced influence between data segments, which we name *latent leakage*. This leakage could systematically lead to higher decoding accuracies for forking paths including the affected preprocessing steps. To the best of our knowledge, the potential of latent leakage has not been systematically analyzed and tends to be ignored in EEG studies.

One possible countermeasure for latent leakage would be to split the time series into a fixed number of temporally separated segments, the trials of which are then used in different cross-validation folds. Preprocessing operations should then be applied only within each segment. However, many algorithms (e.g., ICA or autoreject) may be less stable when run on less data. A different approach could be a separate preprocessing for each cross-validation fold, so that the training data (e.g., 80 %) is used to estimate the independent components and autoreject thresholds, and these models are then applied to the test data without separate estimation. However, such a procedure would increase the computation time enormously, and is computationally not feasible in the multiverse. Both approaches would also work more straightforward, if precautionary measures in paradigm designs were ensured, such as, for instance, an equal distribution of conditions in the different temporarily separated segments.

To preclude noticeable latent leakage in our data, we analyzed if perfect separation of train and test data decreases decoding performance by manipulating HPF, ocular ICA, and autoreject in a subset of forking paths to achieve perfect separation (see Supplementary Text - Influence of latent leakage on decoding performance). The results showed no increase in decoding performance, i.e., no influence of latent leakage (Fig. S32). However, we emphasize that latent leakage should be further investigated in the future in the context of different preprocessing steps outside the current multiverse.

Quantification of decoding performance

In the current article, we report only test accuracies, i.e., we use the terms accuracy and decoding accuracy synonymous to test accuracy, as an abbreviation for averaged, cross-validated, balanced test accuracy. We quantify decoding performance either by test accuracy (EEGNet) or by the *T*-sum of the calculated group statistics (time-resolved).

EEGNet.

For trial-wise decoding using EEGNet, we directly used the averaged, cross-validated, balanced test accuracies. This resulted in up to 2592 test accuracies for each of the 40 participants and each of the 7 experiments. We directly applied a linear mixed model (LMM) (see below), using these test accuracies as the dependent variable.

Time-resolved.

For time-resolved decoding using logistic regression, we first quantified significant clusters at the group level (i.e., across 40 participants) for each forking path and experiment. This was done using a one-tailed, one-sample permutation cluster mass test^{22,76,77}. Briefly, we first defined temporal clusters using a cluster-forming threshold of $p < 0.05$ separately at each time point ($256 \frac{1}{s}$) on the zero-centered averaged decoding time series. For each cluster – i.e., union of all neighboring time points above threshold – the sum of T -values (T -sum) was calculated.

Each participant's individual decoding accuracy time series was then randomly multiplied by either 1 or -1, averaged and zero-centered. Clusters were defined in these permuted datasets using the same cluster-forming threshold. By repeating the permutations 1024 times, we achieved a Monte Carlo sampling of the permutation distribution. The cluster with the highest T -sum per iteration was saved for each sample of the permutation distribution. The p -value was calculated by relating the T -sums of each cluster of the original dataset to those of the sampled permutations, and only clusters falling in the highest 5 % quantile were retained.

For each forking path and experiment, this procedure corrects the alpha error of a cluster being significant at the family-wise error rate⁷⁶. The T -sums over all significant clusters were then entered as the dependent variable into one linear model (LM) per experiment (see below).

As an alternative approach to quantifying time-resolved decoding performance, we averaged the cross-validated test accuracy values across time points after the baseline, for each forking path, experiment, and participant, and entered these values into one LMM per experiment, similar to the procedure applied to EEGNet accuracies. The results are reported in the Supplements (figs. S1 & S2). The rationale was that this approach uses accuracy estimates bounded by the interval between 0.5 and 1.0, which are more readily interpretable than T -sums. However, a typical study would likely rather be focused on delineating and interpreting significant clusters for a group. Therefore, the T -sum approach might be practically more relevant and was chosen to be followed in the main manuscript. Estimation of T -sums on the individual participant level would also be possible⁷⁶ but was avoided for computational reasons in the multiverse context.

Further, we explored the use of threshold-free cluster enhancement⁷⁷ ($TFCE$) instead of defining a fixed cluster-forming threshold. We summed the individual (time point-wise) $TFCE$ -values to $TFCE$ -sums instead of T -values to T -sums. Because $TFCE$ -sums and T -sums correlated strongly across forking paths per experiment (Pearson correlation, all $r > 0.96$, fig. S33), we anticipate similar conclusions from downstream analyses and only continued with the approach using a fixed cluster-forming threshold and corresponding T -sums.

Modeling the effects of preprocessing steps

EEGNet.

We constructed one LMM for each experiment separately. The test accuracies per participant and forking path in that experiment served as the dependent variable. All preprocessing steps were modeled as factors. Each step's version with the smallest intervention served as the reference level (upper option of each step in Figure 1). We also allowed for two-way interactions between all steps. To account for different levels of decoding performance per participant, a random intercept term for the participant was added. To further account for participant-dependent variability within each factor, and to avoid inflation of the alpha error^{78,79}, we added random slopes for all main effects and interactions. All LMMs were estimated using *MixedModels* (v. 4.23.1) for *Julia* (v. 1.10.2,⁸⁰) and transferred to *R*⁸¹ for further processing using *RCall* (v. 0.14.1) and *JellyMe4* (v. 1.2.1), and the *R* package *afex* (v. 1.3.1,⁸²).

Time-resolved.

After identifying significant clusters in the decoding time series of each experiment and forking path, we calculated the total *T*-sum across all significant clusters for each experiment and forking path as a proxy for decoding performance. We then constructed one LM for each experiment separately with the *T*-sum as dependent variable. All single preprocessing steps were modeled as factors, resulting in a full factorial design. As reference-level for each preprocessing step served the variation with the smallest intervention (upper row in Figure 1). Two-way interactions were added between all terms. LMs were estimated using the *stats::lm* function in base *R*⁸¹ (v. 4.2.2).

Modeling interactions.

Since preprocessing steps build on each other, they are likely to interact. The recommended way to include interactions is to define the most complete model possible⁷⁸. On the other hand, more model terms make it more difficult to estimate and ultimately interpret the resulting model. We tested whether the addition of interaction terms added value by first testing whether a considerably higher proportion of variance (R^2) was explained, and second, whether Akaike information criterion (AIC) decreased. Figure S34 shows that a considerable amount of variance is already explained by the main effects when modeling EEGNet decoding performance, but less so for time-resolved decoding performance. Especially for time-resolved decoding performance, interaction terms added substantial value in terms of explained variance (fig. S34). More importantly, including interactions always decreased AIC values (fig. S34).

To keep the model computationally traceable and the results interpretable, we decided for two limitations regarding model interactions. First, we included only two-way but not higher-order interactions, as the number of model terms (both fixed and random effects) increased drastically. Second, we restricted the model to not estimate the correlations between random effect terms, which significantly shortened the computation time.

Estimation of marginal means.

Marginal means and contrasts were estimated using the *emmeans* package (v. 1.10.0)⁸³ in R. Briefly, *emmeans* extracts the mean responses from statistical models, and returns average response variables – in our case model decoding performance operationalized via accuracy or *T*-sum – for each level of a categorical predictor variable. First, we estimated marginal means for all main (fixed) effects to interpret the influence of each preprocessing choice on model decoding performance. Second, we also estimated marginal means for each interaction effect. This step yielded marginal means for each factor level of a given preprocessing choice, grouped into the factor levels of another preprocessing choice. Similarly, contrasts were computed between all pairs of levels.

Statistical significance was calculated model-wise, i.e., per experiment and decoding framework. On the marginal means of each LMM and LM we applied omnibus *F*-tests to each preprocessing step (main effects and interactions) to determine a significant contribution of the preprocessing step to the decoding accuracy, without further correction for multiple comparisons. Then, pairwise *T*-ratios and *p*-values were computed for the main effects between the factor levels of each preprocessing step using Tukey adjustment within each preprocessing step⁸⁴.

Evaluating the impact of manipulating a single preprocessing step.

In an additional analysis, we analyzed the impact of changing one single preprocessing step on decoding performance. For this, we used the example forking path (Fig. 1) as reference. This forking path was defined as reference with the same rationale than for the ERP visualization, because it is loosely related to the preprocessing pipeline used in the accompanying article released with the dataset¹⁸. We then systematically tested how decoding performance changes when we manipulating one single processing step, but leaving all others unchanged.

Impact of preprocessing on baseline artifacts.

We analyzed which preprocessing steps facilitate baseline artifacts. First, we defined the presence of a baseline artifact when significant clusters occurred within or across the baseline windows (table S5), e.g., for N170, clusters extending to a time point ≤ 0.0 s. For ERN, the baseline period was not tied to the response onset and may therefore be outside the decoding range (table S5). Therefore, clusters in ERN emerging before the 0.4 s pre-response time point were defined as baseline artifacts, similar to LRP (table S5).

To assess the contribution of each preprocessing step on the presence of a baseline artifact, we modeled the presence of an artifact in a forking path as a function of all preprocessing steps separately for each experiment. Binary logistic regressions were applied using maximum likelihood estimation with default optimization settings (i.e., convergence threshold of 10^{-8} and a maximum of 25 iterations). We computed likelihood ratio tests to obtain χ^2 statistics and *p*-values, indicating if the exclusion of a preprocessing step significantly reduced model fit ($\alpha = 0.01$).

Treatment of statistical significance.

We deliberately try not to emphasize statistical significance on the multiverse outputs in the remainder of the manuscript. First, by its very nature, the multiverse could theoretically be inflated by adding more preprocessing choices, either entire steps or variations of steps. If we assume that we add another step with two options, and for simplicity assume no interaction with the previous steps, we effectively doubled the number of forking paths for each group. Thus, small effects could be driven to significance by arbitrarily inflating the multiverse. Second, we used both LMMs (EEGNet) and LMs (time-resolved) to infer the influence of preprocessing steps. Due to the random effects in LMMs and the larger number of data points entering the model (factor 40), both parameter estimation and the diagnostic performance of the statistical analyses could vary greatly between the two approaches. Third, the dependent variables were different in LMMs and LMs. A reader might be tempted to compare significances of processing steps between EEGNet and time-resolved approaches, which is not possible for the present analyses. For these reasons, we highlight steps that appear important by analyzing the charts rather than only p -values.

Acknowledgments

This work was supported by German Research Foundation, DFG Heisenberg Program Grant 433758790 (MAS) and Jacobs Foundation, Research Fellowship (MAS).

Author contributions

Conceptualization: RK, AE
Formal analysis: RK
Funding acquisition: MAS
Investigation: RK
Methodology: RK, AE
Project administration: RK
Resources: RK, MAS
Software: RK
Visualization: RK
Writing – original draft: RK
Writing – review & editing: RK, AE, MAS

Competing interests

Authors declare that they have no competing interests.

Data and materials availability

Large files are shared via Zenodo (<https://zenodo.org/records/14223514>), including test accuracies or T -sum values per participant, forking path, experiment, and time point. To allow for a simple comparison of individual preprocessing pipelines and their impact on decoding performance, we deployed an online dashboard at <https://multiverse.streamlit.app>. The raw dataset used in our analyses is shared by its authors¹⁸ at <https://osf.io/thsgq/>.

Code availability statement

A GitHub repository containing all scripts is available at <https://github.com/kesslerr/m4d>, including *Bash & Python* scripts handling the complete multiverse preprocessing and decoding on a high-performance computing cluster. The repository also comprises all analysis scripts to compute LMMs in *Julia*, and to perform all remaining analyses in *R*

based on a *targets* pipeline⁸⁵. Comprehensive lists of package versions in all used programming languages are available at <https://github.com/kessler/m4d/tree/main/env>.

Materials & Correspondence

For any requests, please contact Roman Kessler (rkesslerx@gmail.com).

References

1. Carrasco, C., Bahle, B., Simmons, A. & Luck, S. Using Multivariate Pattern Analysis to Increase Effect Sizes for Event-Related Potential Analyses. *Psychophysiology* (2024).
2. Kriegeskorte, N., Mur, M. & Bandettini, P. Representational similarity analysis – connecting the branches of systems neuroscience. *Front. Syst. Neurosci.* (2008)
doi:10.3389/neuro.06.004.2008.
3. Haxby, J. V., Connolly, A. C. & Guntupalli, J. S. Decoding Neural Representational Spaces Using Multivariate Pattern Analysis. *Annu. Rev. Neurosci.* **37**, 435–456 (2014).
4. Marsicano, G., Bertini, C. & Ronconi, L. Decoding cognition in neurodevelopmental, psychiatric and neurological conditions with multivariate pattern analysis of EEG data. *Neurosci. Biobehav. Rev.* 105795 (2024).
5. Watts, D. *et al.* Predicting treatment response using EEG in major depressive disorder: A machine-learning meta-analysis. *Transl. Psychiatry* **12**, 332 (2022).
6. Aggarwal, S. & Chugh, N. Review of Machine Learning Techniques for EEG Based Brain Computer Interface. *Arch. Comput. Methods Eng.* **29**, 3001–3020 (2022).
7. Pan, J., Li, Y., Gu, Z. & Yu, Z. A comparison study of two P300 speller paradigms for brain–computer interface. *Cogn. Neurodyn.* **7**, 523–529 (2013).
8. Pavlov, Y. G. *et al.* #EEGManyLabs: Investigating the replicability of influential EEG experiments. *Cortex* **144**, 213–229 (2021).

9. Trübtschek, D. *et al.* EEGManyPipelines: A Large-scale, Grassroots Multi-analyst Study of Electroencephalography Analysis Practices in the Wild. *J. Cogn. Neurosci.* **36**, 217–224 (2024).
10. Botvinik-Nezer, R. *et al.* Variability in the analysis of a single neuroimaging dataset by many teams. *Nature* **582**, 84–88 (2020).
11. Yücel, M. A. *et al.* The fNIRS Reproducibility Study Hub (FRESH): Exploring Variability and Enhancing Transparency in fNIRS Neuroimaging Research. Preprint at <https://doi.org/10.31222/osf.io/pc6x8> (2024).
12. Šoškić, A., Styles, S. J., Kappenman, E. S. & Kovic, V. Garden of forking paths in ERP research – effects of varying pre-processing and analysis steps in an N400 experiment. Preprint at <https://doi.org/10.31234/osf.io/8rjah> (2022).
13. Clayson, P. E., Baldwin, S. A., Rocha, H. A. & Larson, M. J. The data-processing multiverse of event-related potentials (ERPs): A roadmap for the optimization and standardization of ERP processing and reduction pipelines. *NeuroImage* **245**, 118712 (2021).
14. Cantone, G. G. & Tomaselli, V. Theory and methods of the multiverse: an application for panel-based models. *Qual. Quant.* **58**, 1447–1480 (2024).
15. Del Giudice, M. & Gangestad, S. W. A Traveler’s Guide to the Multiverse: Promises, Pitfalls, and a Framework for the Evaluation of Analytic Decisions. *Adv. Methods Pract. Psychol. Sci.* **4**, 251524592095492 (2021).
16. Jas, M., Engemann, D. A., Bekhti, Y., Raimondo, F. & Gramfort, A. Autoreject: Automated artifact rejection for MEG and EEG data. *NeuroImage* **159**, 417–429 (2017).
17. Jas, M., Engemann, D., Raimondo, F., Bekhti, Y. & Gramfort, A. Automated rejection and repair of bad trials in MEG/EEG. in *6th International Workshop on Pattern Recognition in Neuroimaging (PRNI)* (Trento, Italy, 2016).

18. Kappenman, E. S., Farrens, J. L., Zhang, W., Stewart, A. X. & Luck, S. J. ERP CORE: An open resource for human event-related potential research. *NeuroImage* **225**, 117465 (2021).
19. Lawhern, V. J. *et al.* EEGNet: a compact convolutional neural network for EEG-based brain–computer interfaces. *J. Neural Eng.* **15**, 056013 (2018).
20. Gramfort, A. *et al.* MNE software for processing MEG and EEG data. *NeuroImage* **86**, 446–460 (2014).
21. King, J.-R. *et al.* Encoding and Decoding Neuronal Dynamics: Methodological Framework to Uncover the Algorithms of Cognition. (2018).
22. Sassenhagen, J. & Draschkow, D. Cluster-based permutation tests of MEG/EEG data do not establish significance of effect latency or location. *Psychophysiology* **56**, e13335 (2019).
23. Frossard, J. & Renaud, O. The cluster depth tests: Toward point-wise strong control of the family-wise error rate in massively univariate tests with application to M/EEG. *NeuroImage* **247**, (2022).
24. Cesnaite, E. EEGManyPipelines: Robustness of EEG results across analysis pipelines. Cutting Gardens Conference. (2023).
25. Widmann, A., Schröger, E. & Maess, B. Digital filter design for electrophysiological data – a practical approach. *J. Neurosci. Methods* **250**, 34–46 (2015).
26. Ehinger, B. V. & Bonasch, H. Decoding accuracies as well as ERP amplitudes do not show between-task correlations. Preprint at (2023).
27. Bailey, N. W. *et al.* EEG is better when cleaning effectively targets artifacts. *bioRxiv* 2024–06 (2024).
28. Lundberg, S. M. & Lee, S.-I. A Unified Approach to Interpreting Model Predictions. in *Advances in Neural Information Processing Systems 30* (eds. Guyon, I. *et al.*) 4765–4774 (Curran Associates, Inc., 2017).

29. Haufe, S. *et al.* On the interpretation of weight vectors of linear models in multivariate neuroimaging. *NeuroImage* **87**, 96–110 (2014).
30. McDermott, E. J. *et al.* Artifacts in EEG-Based BCI Therapies: Friend or Foe? *Sensors* **22**, 96 (2022).
31. Thompson, D. E., Mowla, Md. R., Dhuyvetter, K. J., Tillman, J. W. & Huggins, J. E. Automated Artifact Rejection Algorithms Harm P3 Speller Brain-Computer Interface Performance. *Brain Comput. Interfaces Abingdon Engl.* **6**, 141–148 (2019).
32. Bae, G.-Y. The Time Course of Face Representations during Perception and Working Memory Maintenance. *Cereb. Cortex Commun.* **2**, tgaa093 (2021).
33. Zhang, G., Garrett, D. R. & Luck, S. J. Optimal filters for ERP research II: Recommended settings for seven common ERP components. *Psychophysiology* **61**, e14530 (2024).
34. Goncharova, I. I., McFarland, D. J., Vaughan, T. M. & Wolpaw, J. R. EMG contamination of EEG: spectral and topographical characteristics. *Clin. Neurophysiol.* **114**, 1580–1593 (2003).
35. Tanner, D., Morgan-Short, K. & Luck, S. J. How inappropriate high-pass filters can produce artifactual effects and incorrect conclusions in ERP studies of language and cognition. *Psychophysiology* **52**, 997–1009 (2015).
36. Gennari, G., Dehaene, S., Valera, C. & Dehaene-Lambertz, G. Spontaneous supra-modal encoding of number in the infant brain. *Curr. Biol.* **33**, 1906-1915.e6 (2023).
37. Van Driel, J., Olivers, C. N. L. & Fahrenfort, J. J. High-pass filtering artifacts in multivariate classification of neural time series data. *J. Neurosci. Methods* **352**, 109080 (2021).
38. Delorme, A. EEG is better left alone. *Sci. Rep.* **13**, 2372 (2023).
39. Eriksen, B. A. & Eriksen, C. W. Effects of noise letters upon the identification of a target letter in a nonsearch task. *Percept. Psychophys.* **16**, 143–149 (1974).
40. Feuerriegel, D. & Bode, S. Bring a map when exploring the ERP data processing multiverse: A commentary on Clayson *et al.* 2021. *NeuroImage* **259**, 119443 (2022).

41. Saeidi, M. *et al.* Neural Decoding of EEG Signals with Machine Learning: A Systematic Review. *Brain Sci.* **11**, 1525 (2021).
42. Xiao, R. & Ding, L. EEG resolutions in detecting and decoding finger movements from spectral analysis. *Front. Neurosci.* **9**, 308 (2015).
43. Schirrneister, R. T. *et al.* Deep learning with convolutional neural networks for EEG decoding and visualization. *Hum. Brain Mapp.* (2017) doi:10.1002/hbm.23730.
44. Hebart, M. N. *et al.* THINGS: A database of 1,854 object concepts and more than 26,000 naturalistic object images. *PLOS ONE* **14**, e0223792 (2019).
45. Grootswagers, T., Zhou, I., Robinson, A. K., Hebart, M. N. & Carlson, T. A. Human EEG recordings for 1,854 concepts presented in rapid serial visual presentation streams. *Sci. Data* **9**, 3 (2022).
46. Quek, G., Zeng, Z., Varlet, M. & Grootswagers, T. Human infant EEG recordings for 200 object images presented in rapid visual streams. Preprint at <https://doi.org/10.31234/osf.io/dzrkq> (2024).
47. Akça, M., Vuoskoski, J. K., Laeng, B. & Bishop, L. Recognition of brief sounds in rapid serial auditory presentation. *Plos One* **18**, e0284396 (2023).
48. Franco, A., Eberlen, J., Destrebecqz, A., Cleeremans, A. & Bertels, J. Rapid serial auditory presentation. *Exp. Psychol.* (2015).
49. Paul, M., Govaart, G. H. & Schettino, A. Making ERP research more transparent: Guidelines for preregistration. *Int. J. Psychophysiol.* **164**, 52–63 (2021).
50. Schroeder, P. A. *et al.* Using preregistration as a tool for transparent fNIRS study design. *Neurophotonics* **10**, (2023).
51. Alday, P. M. How much baseline correction do we need in ERP research? Extended GLM model can replace baseline correction while lifting its limits. *Psychophysiology* **56**, e13451 (2019).

52. Hill, A. T. *et al.* Neural differences in conflict monitoring and stimulus expectancy processes in experienced meditators are likely driven by enhanced attention. Preprint at <https://doi.org/10.1101/2024.12.23.630201> (2024).
53. Gratton, G., Coles, M. G. H. & Donchin, E. A new method for off-line removal of ocular artifact. *Electroencephalogr. Clin. Neurophysiol.* **55**, 468–484 (1983).
54. Bigdely-Shamlo, N., Mullen, T., Kothe, C., Su, K.-M. & Robbins, K. A. The PREP pipeline: standardized preprocessing for large-scale EEG analysis. *Front. Neuroinformatics* **9**, (2015).
55. Pion-Tonachini, L., Kreutz-Delgado, K. & Makeig, S. ICLabel: An automated electroencephalographic independent component classifier, dataset, and website. *NeuroImage* **198**, 181–197 (2019).
56. Gramfort, A. *et al.* MEG and EEG data analysis with MNE-Python. *Front. Neurosci.* **7**, 267 (2013).
57. Maier, M. *et al.* Neural dynamics of mental state attribution to social robot faces. *Soc. Cogn. Affect. Neurosci.* nsaf027 (2025).
58. Delorme, A. & Martin, J. A. Automated Data Cleaning for the Muse EEG. in *2021 IEEE International Conference on Bioinformatics and Biomedicine (BIBM)* (2021). doi:10.1109/BIBM52615.2021.9669415.
59. Winkler, I., Debener, S., Muller, K.-R. & Tangermann, M. On the influence of high-pass filtering on ICA-based artifact reduction in EEG-ERP. in *2015 37th Annual International Conference of the IEEE Engineering in Medicine and Biology Society (EMBC)* 4101–4105 (IEEE, Milan, 2015). doi:10.1109/EMBC.2015.7319296.
60. Ablin, P., Cardoso, J.-F. & Gramfort, A. Faster Independent Component Analysis by Preconditioning With Hessian Approximations. *IEEE Trans. Signal Process.* **66**, 4040–4049 (2018).

61. Bailey, N. W. *et al.* RELAX part 2: A fully automated EEG data cleaning algorithm that is applicable to Event-Related-Potentials. *Clin. Neurophysiol.* **149**, 202–222 (2023).
62. Dharmaprani, D. *et al.* A comparison of independent component analysis algorithms and measures to discriminate between EEG and artifact components. in *2016 38th Annual International Conference of the IEEE Engineering in Medicine and Biology Society (EMBC)* (IEEE, 2016).
63. Whitham, E. M. *et al.* Scalp electrical recording during paralysis: Quantitative evidence that EEG frequencies above 20Hz are contaminated by EMG. *Clin. Neurophysiol.* **118**, 1877–1888 (2007).
64. Grootswagers, T., Wardle, S. G. & Carlson, T. A. Decoding Dynamic Brain Patterns from Evoked Responses: A Tutorial on Multivariate Pattern Analysis Applied to Time Series Neuroimaging Data. *J. Cogn. Neurosci.* **29**, 677–697 (2017).
65. Cichy, R. M. & Pantazis, D. Multivariate pattern analysis of MEG and EEG: A comparison of representational structure in time and space. *NeuroImage* **158**, 441–454 (2017).
66. Bae, G.-Y., Leonard, C. J., Hahn, B., Gold, J. M. & Luck, S. J. Assessing the information content of ERP signals in schizophrenia using multivariate decoding methods. *NeuroImage Clin.* **25**, 102179 (2020).
67. Kaneshiro, B., Perreau Guimaraes, M., Kim, H.-S., Norcia, A. M. & Suppes, P. A Representational Similarity Analysis of the Dynamics of Object Processing Using Single-Trial EEG Classification. *PLOS ONE* **10**, e0135697 (2015).
68. Xie, S. *et al.* Visual category representations in the infant brain. *Curr. Biol.* **32**, 5422-5432.e6 (2022).
69. Ashton, K. *et al.* Time-resolved multivariate pattern analysis of infant EEG data: A practical tutorial. *Dev. Cogn. Neurosci.* **54**, 101094 (2022).

70. Thölke, P. *et al.* Class imbalance should not throw you off balance: Choosing the right classifiers and performance metrics for brain decoding with imbalanced data. *NeuroImage* **277**, 120253 (2023).
71. Fan, R.-E., Chang, K.-W., Hsieh, C.-J., Wang, X.-R. & Lin, C.-J. LIBLINEAR: A Library for Large Linear Classification. *J. Mach. Learn. Res.* **9**, 1871–1874 (2008).
72. Brookshire, G. *et al.* Data leakage in deep learning studies of translational EEG. *Front. Neurosci.* **18**, 1373515 (2024).
73. Kapoor, S. & Narayanan, A. Leakage and the reproducibility crisis in machine-learning-based science. *Patterns* **4**, 100804 (2023).
74. Kaufman, S., Rosset, S. & Perlich, C. Leakage in data mining: formulation, detection, and avoidance. *ACM Trans. Knowl. Discov. Data TKDD* **6**, 1–21 (2011).
75. Kinahan, S., Saidi, P., Daliri, A., Liss, J. & Berisha, V. Achieving Reproducibility in EEG-Based Machine Learning. in *The 2024 ACM Conference on Fairness, Accountability, and Transparency* 1464–1474 (ACM, Rio de Janeiro Brazil, 2024).
doi:10.1145/3630106.3658983.
76. Maris, E. & Oostenveld, R. Nonparametric statistical testing of EEG- and MEG-data. *J. Neurosci. Methods* **164**, 177–190 (2007).
77. Smith, S. & Nichols, T. Threshold-free cluster enhancement: Addressing problems of smoothing, threshold dependence and localisation in cluster inference. *NeuroImage* **44**, 83–98 (2009).
78. Barr, D. J., Levy, R., Scheepers, C. & Tily, H. J. Random effects structure for confirmatory hypothesis testing: Keep it maximal. *J. Mem. Lang.* **68**, 255–278 (2013).
79. Ehinger, B. LMM type-1 error for 1+condition+(1|subject).
<https://benediktehinger.de/blog/science/lmm-type-1-error-for-1condition1subject/> (2023).

80. Bezanson, J., Edelman, A., Karpinski, S. & Shah, V. B. Julia: A fresh approach to numerical computing. *SIAM Rev.* **59**, 65–98 (2017).
81. R Core Team. R: A language and environment for statistical computing. R Foundation for Statistical Computing (2021).
82. Singmann, H. & Kellen, D. An introduction to mixed models for experimental psychology. in *New methods in cognitive psychology* 4–31 (Routledge, 2019).
83. Lenth, R. V. emmeans: Estimated Marginal Means, aka Least-Squares Means. (2024).
84. Tukey, J. W. Comparing Individual Means in the Analysis of Variance. *Biometrics* **5**, 99–114 (1949).
85. Landau, W. M. The targets R package: a dynamic Make-like function-oriented pipeline toolkit for reproducibility and high-performance computing. *J. Open Source Softw.* **6**, 2959 (2021).
86. Shrout, P. E. & Fleiss, J. L. Intraclass correlations: uses in assessing rater reliability. *Psychol. Bull.* **86**, 420 (1979).
87. Cicchetti, D. V. Guidelines, criteria, and rules of thumb for evaluating normed and standardized assessment instruments in psychology. *Psychol. Assess.* **6**, 284 (1994).
88. Benjamini, Y. & Hochberg, Y. Controlling the false discovery rate: a practical and powerful approach to multiple testing. *J. R. Stat. Soc. Ser. B Methodol.* **57**, 289–300 (1995).

Supplementary Materials for

How EEG preprocessing shapes decoding performance

Roman Kessler *et al.*

*Corresponding author. Email: rkesslerx@gmail.com

This PDF file includes:

Supplementary Text

- Variability due to random seed in autoreject
- Influence of latent leakage on decoding performance
- Alternative order of preprocessing steps
- Influence of the participant in the LMMs

Figures S1 to S34

Tables S1 to S9

Supplementary Text

Variability due to random seed in autoreject

The *autoreject* package^{16,17} shows considerable variability in the number of dropped epochs, when applied to the same data but using a different random seed. To illustrate this, we used in a first analysis one example participant in the ERN experiment to show the influences of the random seed in the autoreject function, and a random seed in trial sampling prior to fitting the autoreject model. Some variability due to the seed in sampling the epochs for fitting autoreject is expected. We therefore tested 19 random seeds at both stages. Figure S29 illustrates, that substantial variability is introduced by random seeds at both stages. However, figure S30 illustrates, that similar epochs are rejected for different seeds, i.e., if a seed rejects more epochs, it usually contains epochs also rejected using a different seed.

In a second analysis, using all participants, we tested the intraclass correlation coefficient⁸⁶ (ICC, version 1,1) to illustrate the reliability of accuracy values across different random seeds using the Python package *pingouin* (v. 0.5.5). We used the N170 experiment and randomly selected three example pipelines (1. ocular ICA, muscle ICA, 45 Hz LPF, 0.5 Hz HPF, average reference, linear detrending, 200 ms baseline, 2. no ICAs, 45 Hz LPF, 0.5 Hz HPF, average reference, linear detrending, 200 ms baseline, and 3. no ICAs, 45 Hz LPF, 0.1 Hz HPF, average reference, linear detrending, no baseline) without autoreject, and added an autoreject step in the *interpolate* version and in the *reject* version, resulting in 6 forking paths. For each forking path, we applied autoreject with 5 different seeds set in the autoreject estimation (seeds 0, 1, 2, 3, 4) while keeping the sampling seed constant (seed 0). Further, we kept the seed in autoreject constant (seed 0), and varied the sampling seed (seeds 0, 1, 2, 3, 4). The resulting data were used for decoding with EEGNet. This was repeated for all 40 participants.

We computed ICCs separately across different seed numbers and participants, for each pipeline and for all seed types (autoreject seed or sampling seed). All resulting ICCs were greater than 0.867 (all $p < 0.05$, false discovery rate-corrected), indicating excellent agreement⁸⁷ between different seeds when evaluating participant test accuracies.

Lastly, we calculated the ICCs of the average accuracies (across participants) for each forking path, with the seeds as raters. All ICCs were greater than 0.466 (all $p < 0.05$, false discovery rate-corrected), indicating fair agreement⁸⁷ between different seeds when evaluating the test accuracies across forking paths.

Influence of latent leakage on decoding performance

To investigate latent leakage caused by joint preprocessing of the data later used in the different cross-validation splits, we analyzed the N170 dataset including all participants. We investigated ocular ICA, autoreject, and HPF in separate analyses, by choosing a simple preprocessing pipeline for each step (i.e., corresponding to one forking path). We sealed the respective preprocessing step by meticulously separating train and test sets. We decoded from the leaky and the sealed processing pipelines and compared decoding performances.

HPF: For the leaky pipeline, we filtered the participants entire raw time series in one step using a HPF cutoff of 0.1 Hz, corresponding to a filter length of 33 s (table S6). We divided the raw time

series into 5 segments of equal length and extracted epochs from each segment (baseline correction of 200 ms, no detrending). We used Cz as reference. No other artifact correction steps were performed. We trained and tested an EEGNet classifier similarly to before, using a 5-fold cross-validation with balanced accuracy. For the sealed pipeline, we divided the raw time series into 5 segments prior to applying the HPFs on each segment individually. The remaining steps were the same.

ICA: For both pipelines, we first applied a HPF of 0.5 Hz, and a LPF of 45 Hz. For the leaky pipeline, we estimated the ICA, detected and rejected the artifactual components on the entire time series. The time series was divided into 5 segments, epochs were extracted from each segment as before, and these were used in the separate cross-validation folds. For the sealed pipeline, we split already the filtered time series into 5 segments, and fitted the ICA only on the 4 (out of 5) segments that were later used for training. We applied the ICA to the train and test segments. This effectively excluded the test segment from the estimation of the ICA and the rejection thresholds. We repeated this for all 5 folds, extracted the epochs, and used them for the respective training and testing. Balanced accuracies were averaged across folds. To ensure an equal number of trials across the leaky and sealed versions of a pipeline, we always discarded trials near the segment boundaries.

Autoreject: For both pipelines, we first deployed HPFs and LPFs as before. Then we epoched the data as before. We used the "interpolate" version of autoreject (see Methods). For the leaky pipeline, we estimated the autoreject thresholds using all epochs. The epochs were then divided into 5 parts to be used in cross-validation. For the sealed version, we divided the epochs before the autoreject step. For each fold of the cross-validation, the autoreject parameters were estimated on the 4 segments in the train set, and the rejection threshold was applied to train and test sets. Balanced accuracies were averaged across folds.

We used a one-tailed, paired sample T -test for each preprocessing step to evaluate, whether the leaky pipeline resulted in higher decoding accuracies than the sealed pipeline. Figure S32 illustrates, that there was no higher decoding accuracies for leaky pipelines as compared to sealed pipelines (all $p > 0.638$).

Alternative order of preprocessing steps

We tested one alternative order of preprocessing steps in a reduced multiverse. There we applied the steps in the order of (1) re-referencing, (2) HPF & LPF, (3) ocular artifact correction, (4) muscle artifact correction, (5) baseline correction & detrending, and (6) autoreject. In this version, we always performed a baseline correction (either 200 ms or 400 ms). For detrending, we chose between offset (subtract mean) and linear (apply linear function and keep residuals). We either used autoreject in the interpolate version, or did not apply it. The remaining choices were the same. Following a similar intuition than with the main multiverse, we also filtered the data with 1 Hz prior to ICA⁵⁹.

Figure S26 illustrates the decoding performances (accuracies and T -sums) for classifiers trained on data preprocessed with the alternative multiverse order. The magnitudes were comparable to those reported in our main multiverse pipeline (Fig. 3). We also computed the corresponding

marginal means (fig. S27). Most effects were in a similar direction as in our main multiverse results (Fig. 5). However, the LPF in the EEGNet framework had quite opposite effects. This can be explained by the fact that it is followed by the muscle artifact correction step, which had no effect (i.e., did not drop any components) when a LPF of 6 Hz or 20 Hz was applied. This, in turn, resulted in all forking paths with these filter settings having no muscle artifacts removed, which in turn were predictive and increased decoding performance.

Influence of the participant in the LMMs

Within the LMMs constructed to explain the accuracies of trained EEGNet models, we included random intercepts for the 40 participants. Figure S22 illustrates, how the distribution of age, sex, handedness corresponds to the random intercept, i.e., to the individual participants offset in decoding accuracy. Age and handedness did not show any noticeable pattern. We further tested the difference of random intercepts between sexes using a Mann–Whitney U test with Benjamini Hochberg false discovery rate adjustment⁸⁸ for 7 experiments (fig. S22, middle column). No significant differences were observed. We repeated the same analysis for time-resolved LMM results, which were fitted with the averaged decoding accuracies over time as dependent variables (fig. S23). No significant differences were observed.

In addition, figure S24 illustrates the estimated random intercepts for each participant across the 7 experiments. One might hypothesize that participants with a high random intercept in one experiment would also have a high random intercept in the other experiments, indicating that it is easier to decode of EEG signals from some participants, but not others. For each pair of experiments, we computed Pearson correlation coefficients between the random intercepts of the same participants, and corrected for the false discovery rate using Benjamini Hochberg procedure. Figure S24 generally shows no such a relationship. The only significant correlations were observed between the random intercepts of LRP and N170 (fig. S24)²⁶. We repeated the same analysis for time-resolved LMM results, which were fitted with the individual-participant averaged decoding accuracies over time as dependent variables instead of group T-sum values (fig. S25). No significant correlations were observed.

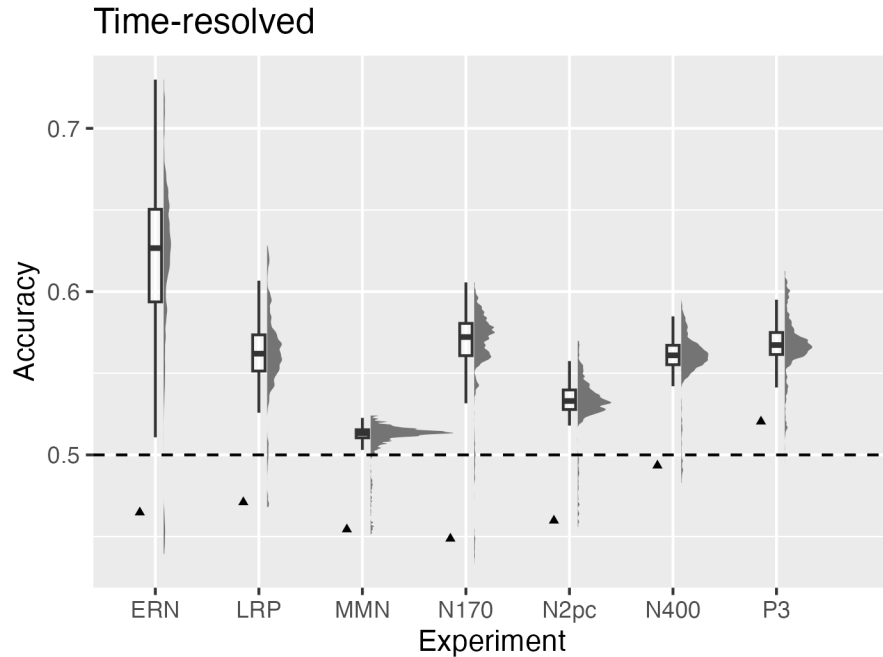


Fig. S1. Overview of average time-resolved decoding accuracies.

Average post-baseline decoding accuracies (y-axis) are plotted for each forking path, further averaged across participants, separately for each experiment (x-axis). Unlike Figure 3B, it is the average decoding accuracy that is plotted, not the T -sum. Triangles indicate the forking path without any preprocessing. Boxes represent the interquartile range (25th to 75th percentile), with the median indicated by a solid black line. Whiskers extend to the most extreme values within 1.5 times the interquartile range from the lower and upper quartiles.

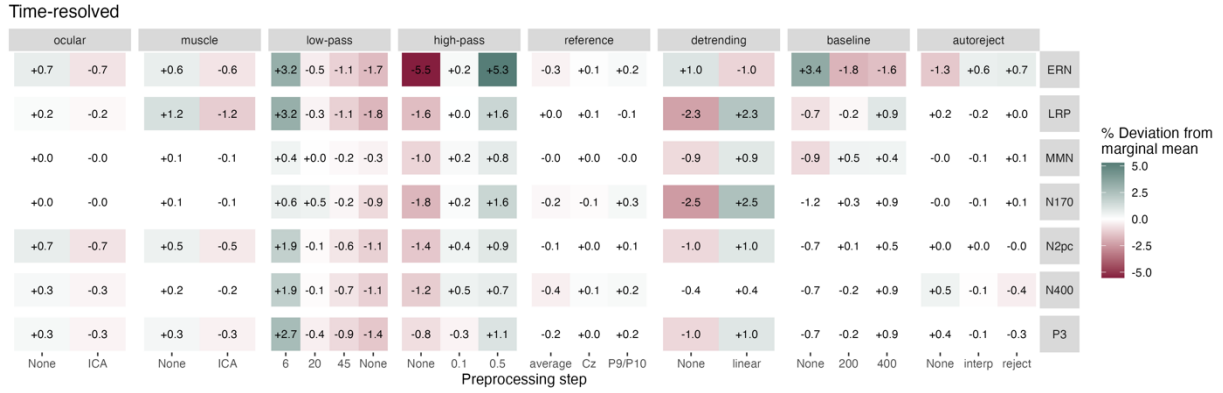


Fig. S2. Influence of preprocessing steps on time-resolved decoding performance. The average post-baseline decoding accuracy is used as a proxy for decoding performance instead of T -sum. Only cells with significant F -test ($p < 0.05$) are colored. See Figure 5 for more details.

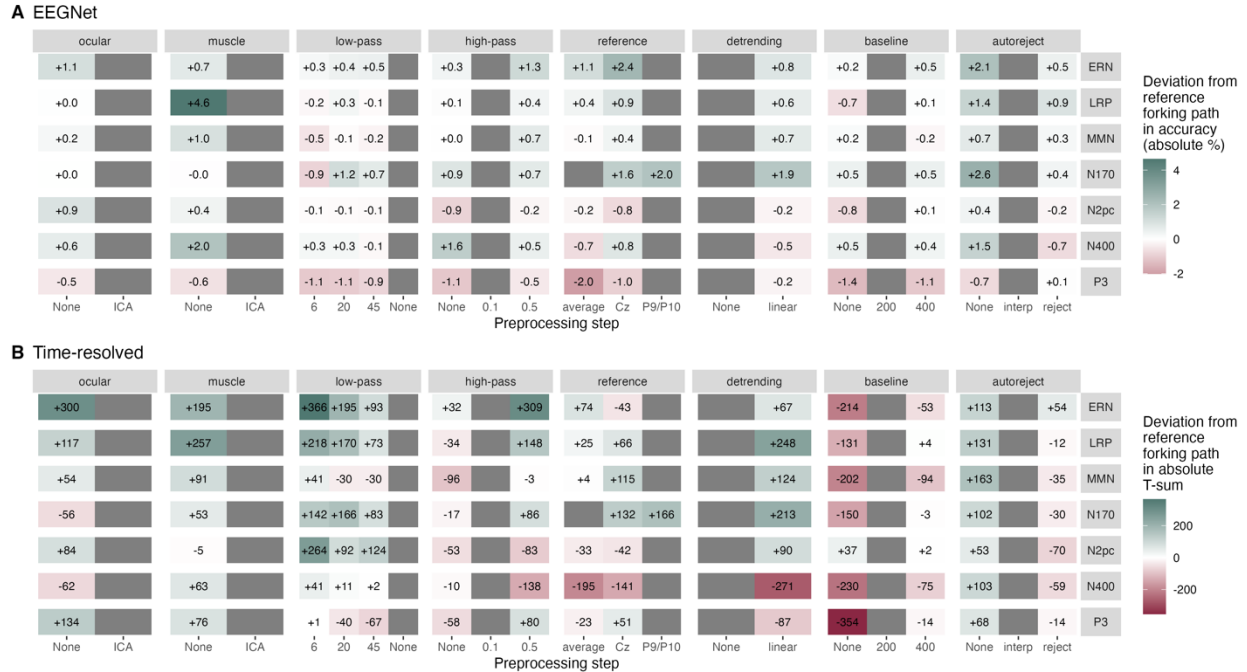


Fig. S3. Influence of varying one single preprocessing steps on decoding performance. Absolute increase or decrease in decoding performance – either accuracy (EEGNet, **A**) or T -sum (time-resolved, **B**) – is depicted within each tile. Change in decoding performance for each level (x-axis) of preprocessing step (horizontal panels) are illustrated in comparison to the example forking path (asterisks in Fig. 1) for each respective experiment (vertical panels). Grey tiles indicate steps of the respective reference forking path. Color scales differ in **A** and **B**. *Ocular*: ocular artifact correction; *muscle*: muscle artifact correction; *ICA*: independent component analysis, *low-pass*: low-pass filter in Hertz; *high-pass*: high-pass filter in Hertz; *baseline*: baseline interval in milliseconds; *autoreject* version either interpolate (*interp*) or reject artifact-contaminated trials (*reject*).

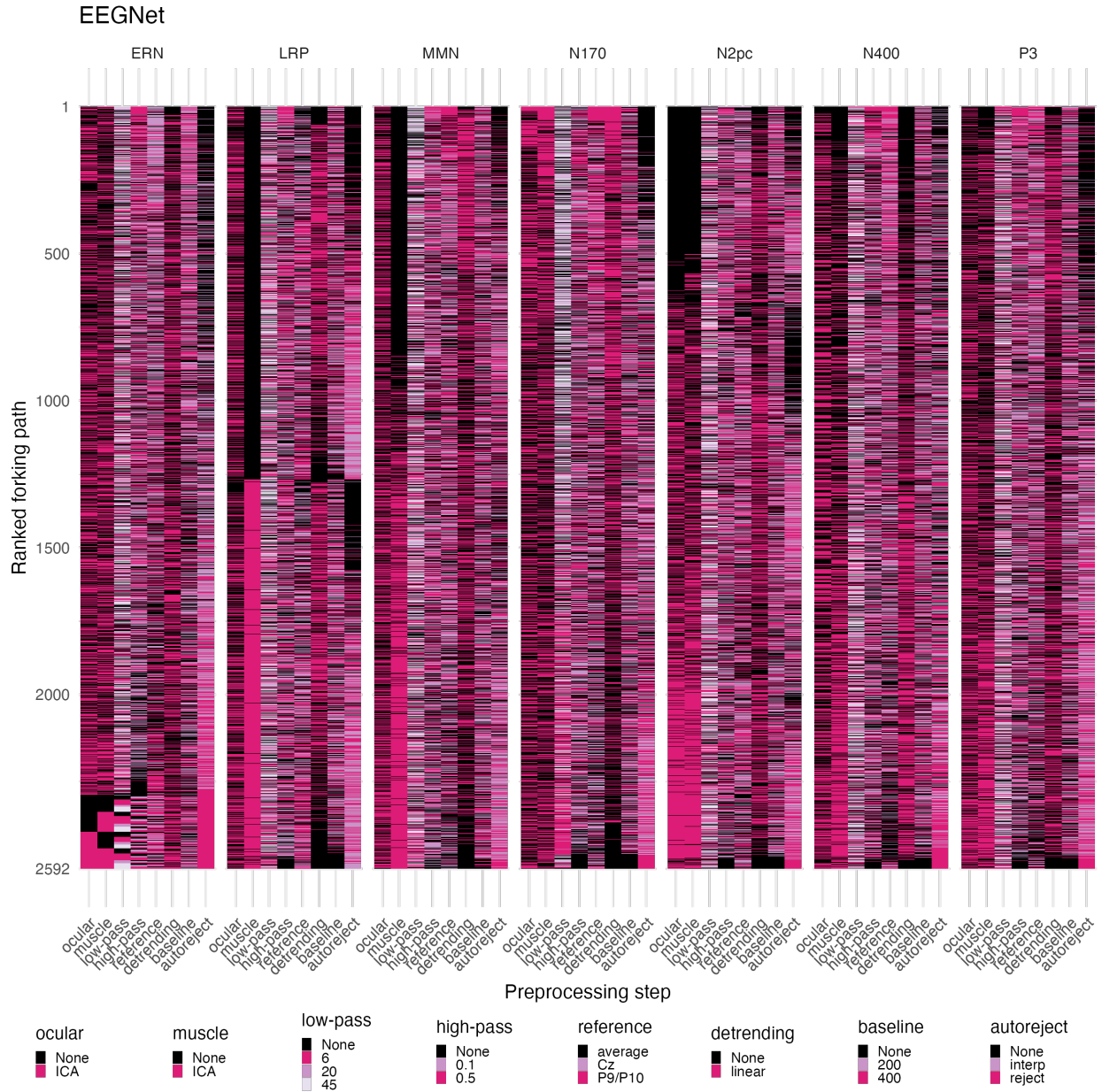


Fig. S4. Ranked forking path performances (EEGNet decoding).

For each experiment (horizontal panels), the forking paths were ranked from highest (#1) to lowest (#2592) decoding performance. The individual variations of each preprocessing step (x-axes) are color-coded. Each individual row corresponds to one data point in Figure 3A. *Ocular*: ocular artifact correction; *muscle*: muscle artifact correction; *ICA*: independent component analysis, *low-pass*: low-pass filter in Hertz; *high-pass*: high-pass filter in Hertz; *baseline*: baseline interval in milliseconds; *autoreject* version either interpolate (*interp*) or reject artifact-contaminated trials (*reject*).

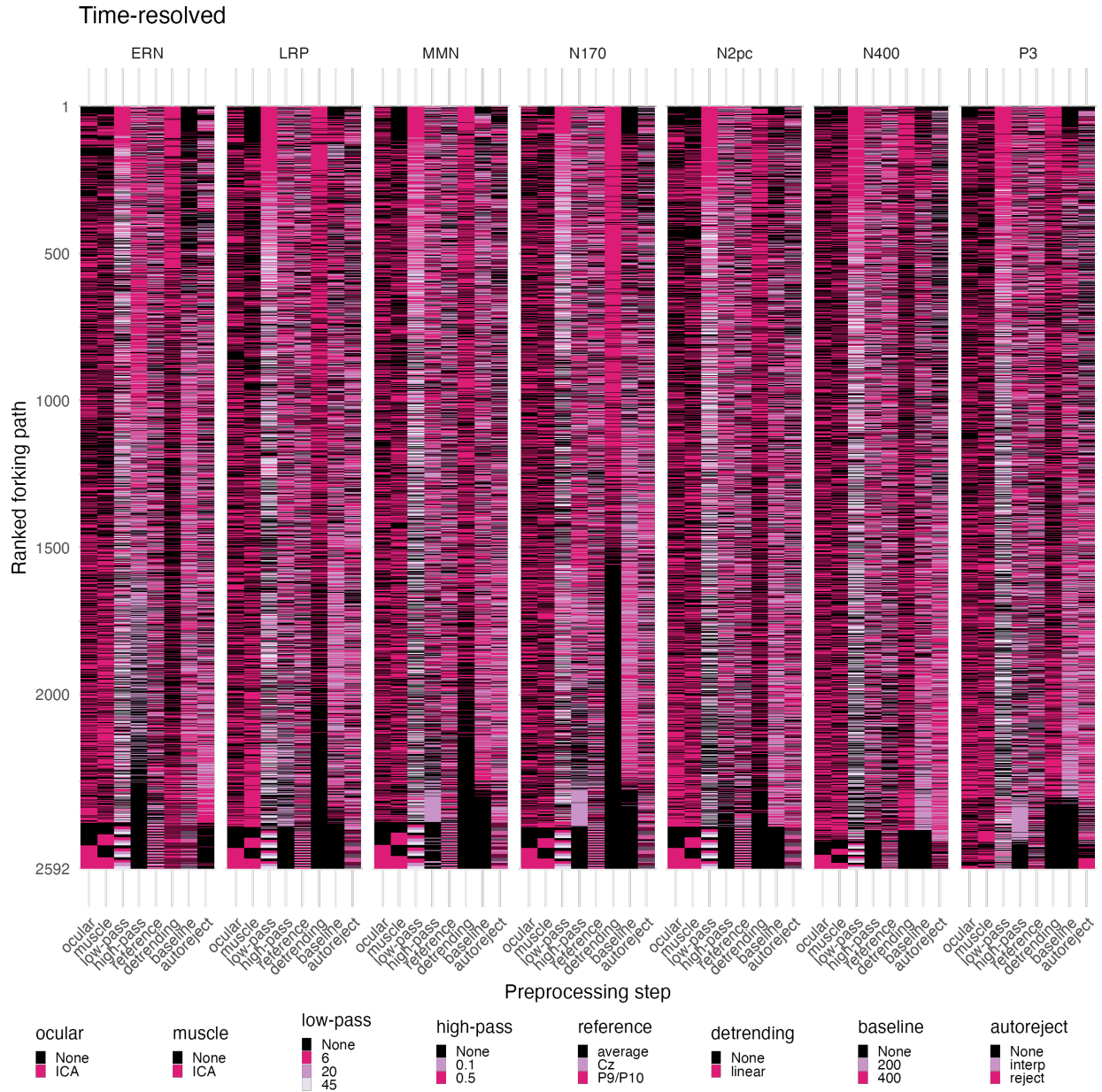


Fig. S5. Ranked forking path performances (time-resolved decoding).

For each experiment (horizontal panels), the forking paths were ranked from highest (#1) to lowest (#2592) decoding performance. The individual variations of each preprocessing step (x-axes) are color-coded. Each individual row corresponds to one data point in Figure 3B. *Ocular*: ocular artifact correction; *muscle*: muscle artifact correction; *ICA*: independent component analysis, *low-pass*: low-pass filter in Hertz; *high-pass*: high-pass filter in Hertz; *baseline*: baseline interval in milliseconds; *autoreject* version either interpolate (*interp*) or reject artifact-contaminated trials (*reject*).

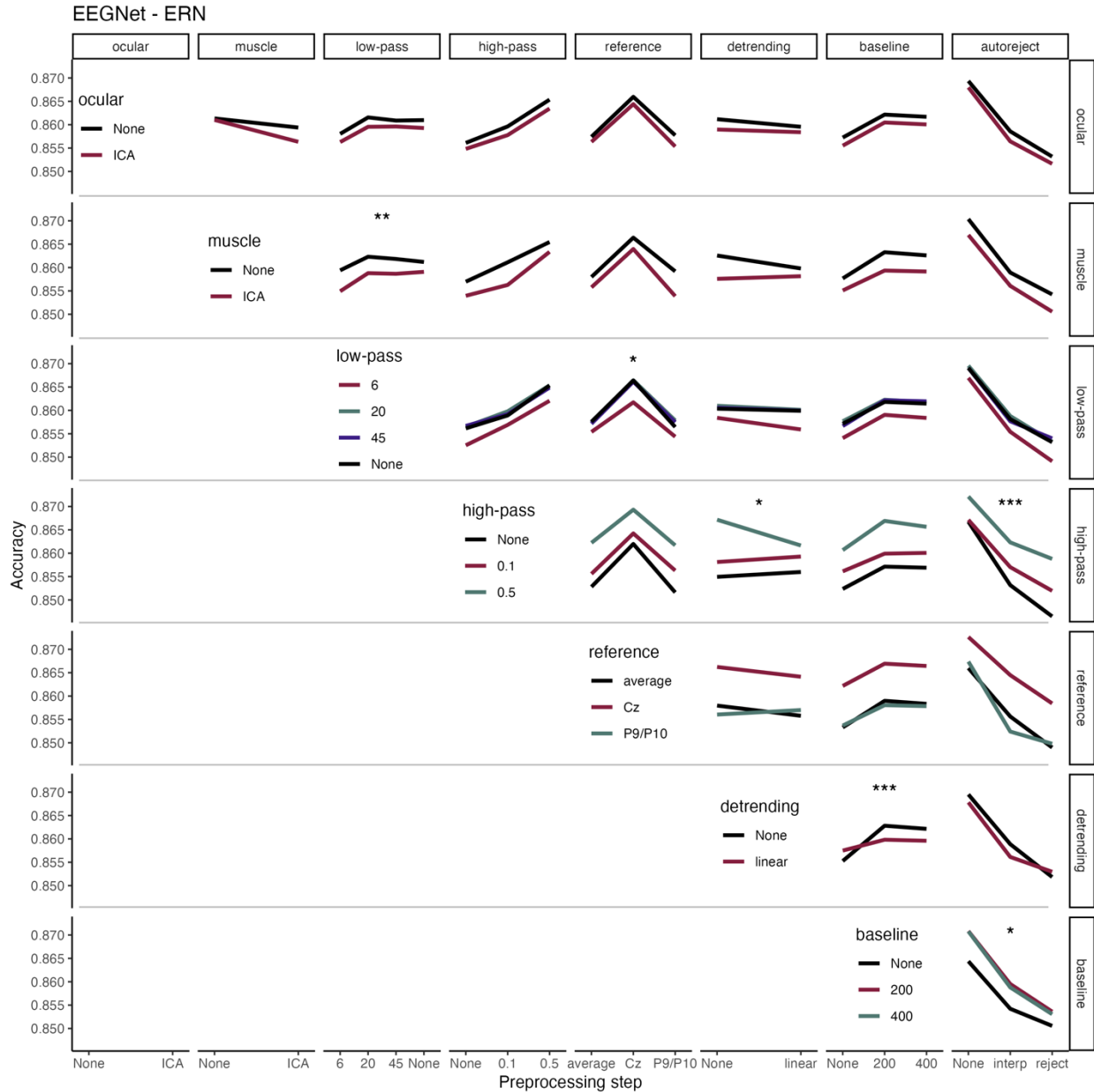


Fig. S6. Interactions between preprocessing steps on decoding performance for ERN and EEGNet decoding.

Horizontal and vertical panels illustrate the different preprocessing steps. The individual preprocessing choices are illustrated on the x-axes and color-coded. The color legends on the diagonal refer to each horizontal panel. (Balanced) Decoding accuracies are shown on the y-axes. Stars indicate the significance (* $p < 0.05$; ** $p < 0.01$; *** $p < 0.001$). *Ocular*: ocular artifact correction; *muscle*: muscle artifact correction; *ICA*: independent component analysis, *low-pass*: low-pass filter in Hertz; *high-pass*: high-pass filter in Hertz; *baseline*: baseline interval in milliseconds; *autoreject* version either interpolate (*interp*) or reject artifact-contaminated trials (*reject*).

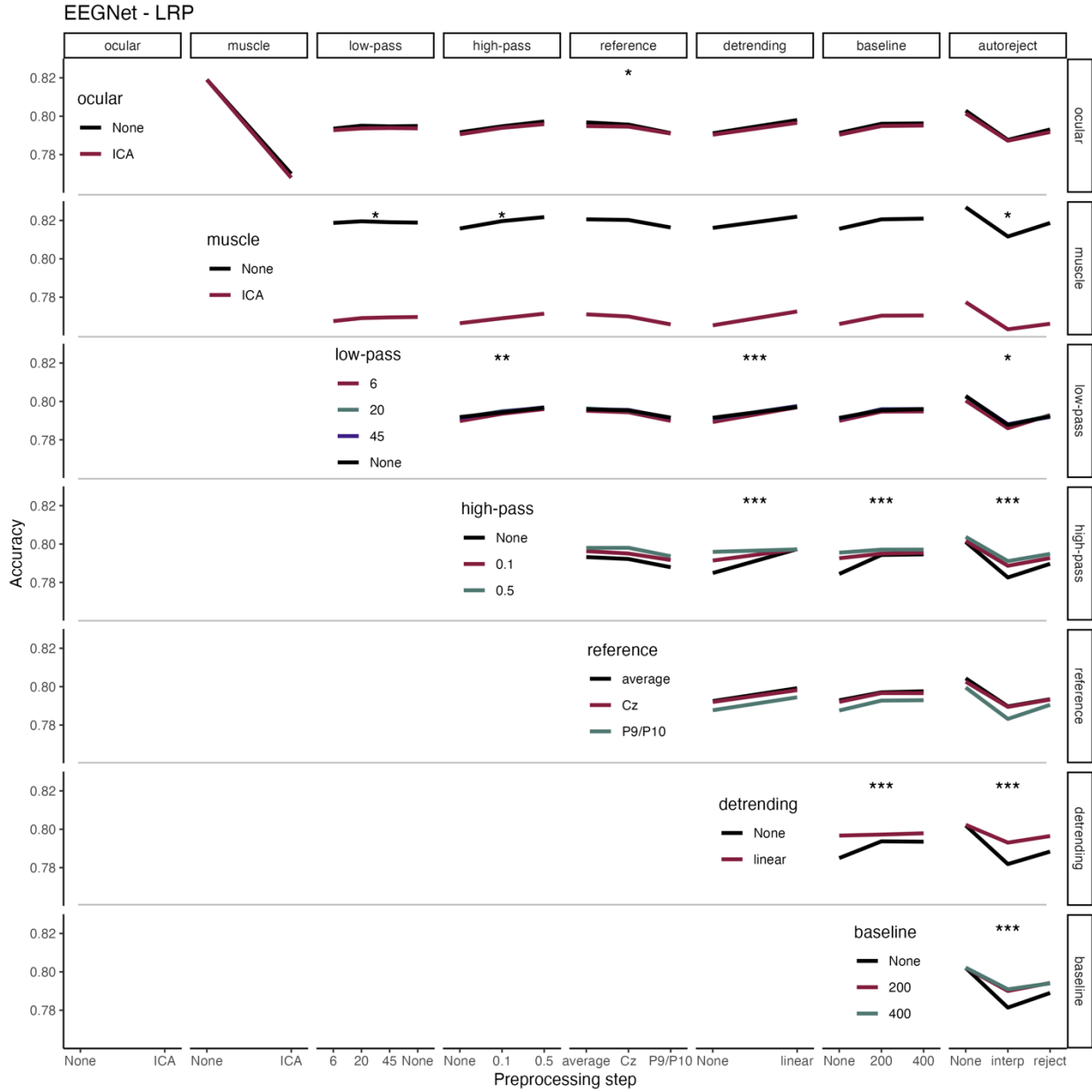


Fig. S7. Interactions between preprocessing steps on decoding performance for LRP and EEGNet decoding.
 See Figure S5 for details.

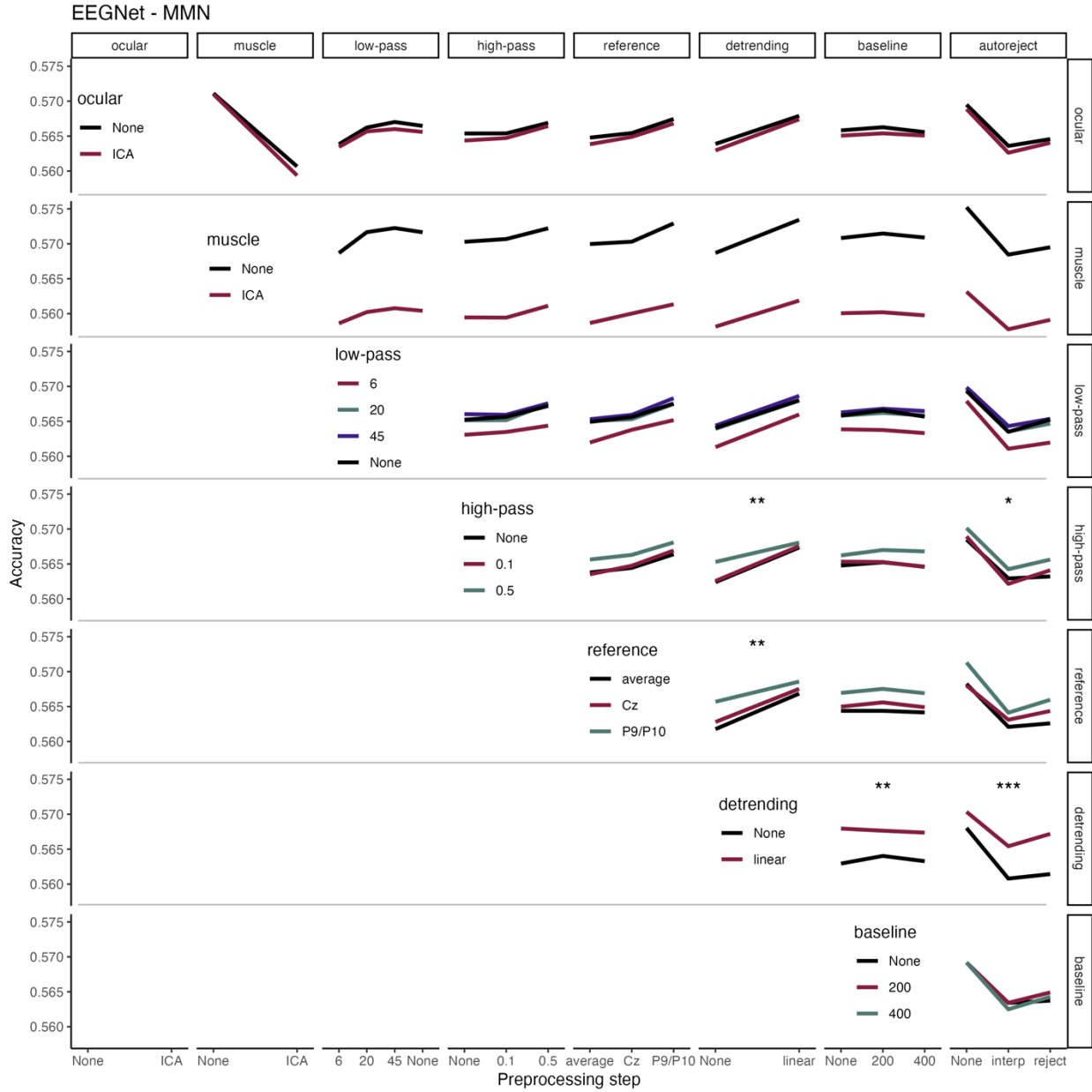


Fig. S8. Interactions between preprocessing steps on decoding performance for MMN and EEGNet decoding.
See Figure S6 for details.

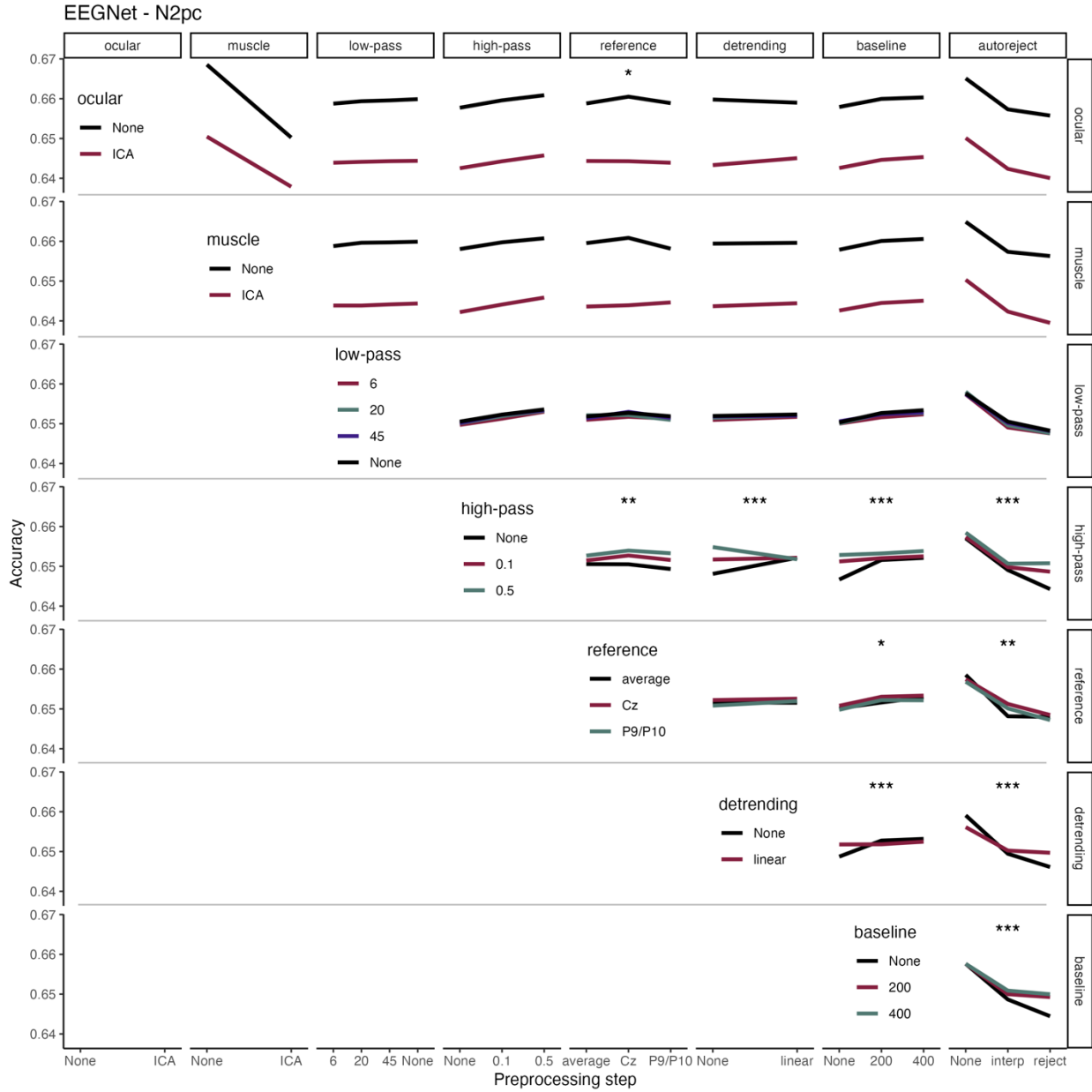


Fig. S9. Interactions between preprocessing steps on decoding performance for N2pc and EEGNet decoding.

See Figure S6 for details.

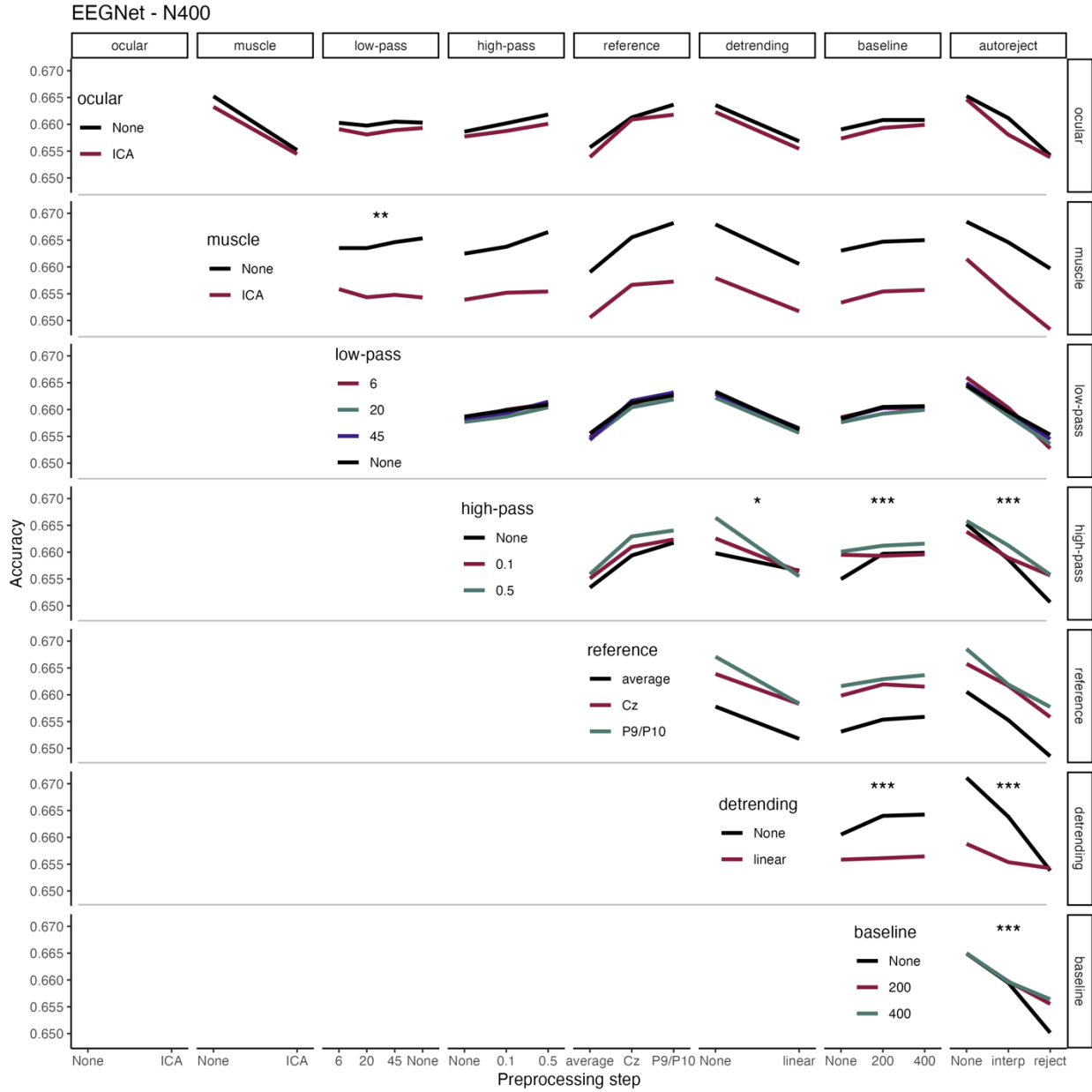


Fig. S10. Interactions between preprocessing steps on decoding performance for N400 and EEGNet decoding.

See Figure S6 for details.

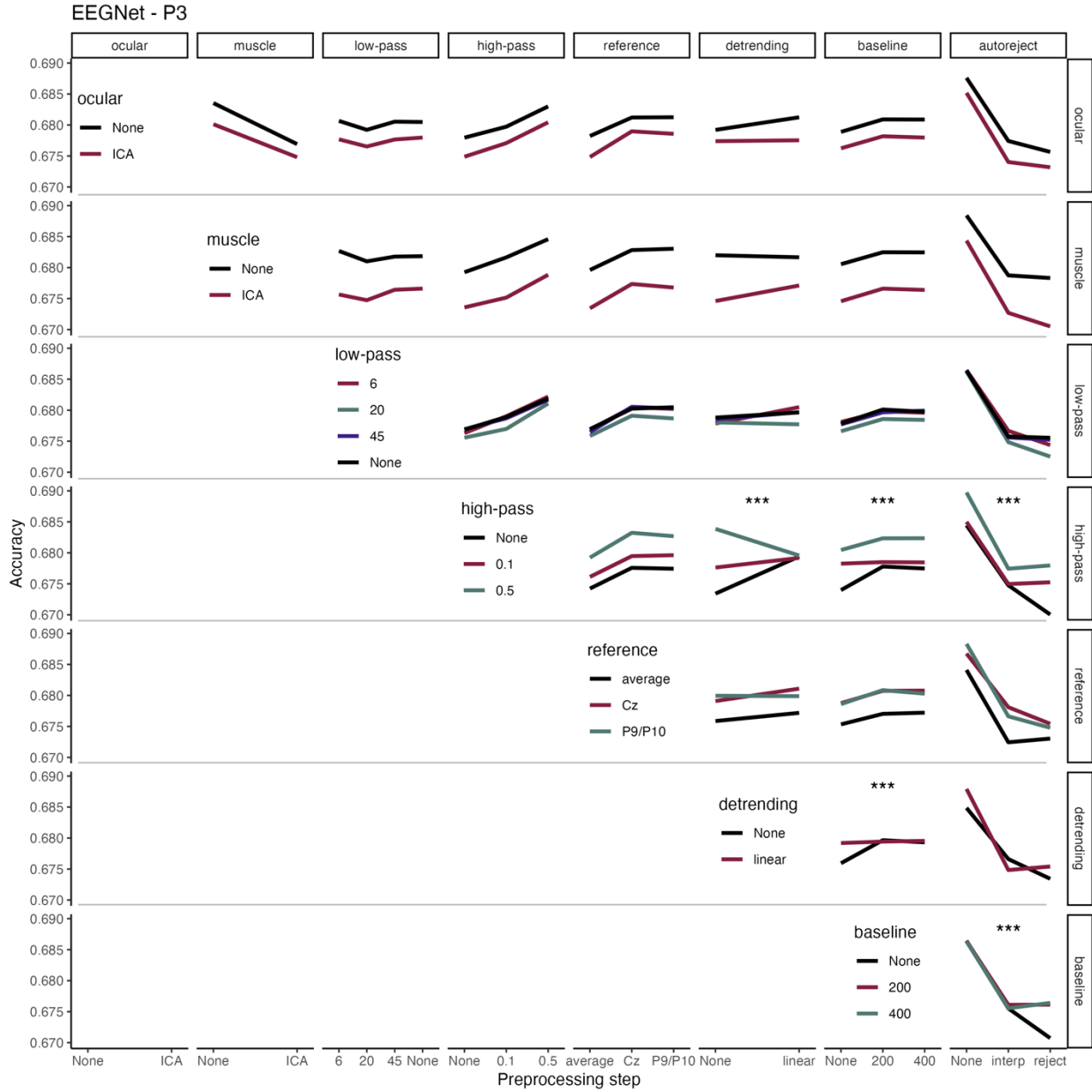


Fig. S11. Interactions between preprocessing steps on decoding performance for P3 and EEGNet decoding.

See Figure S6 for details.

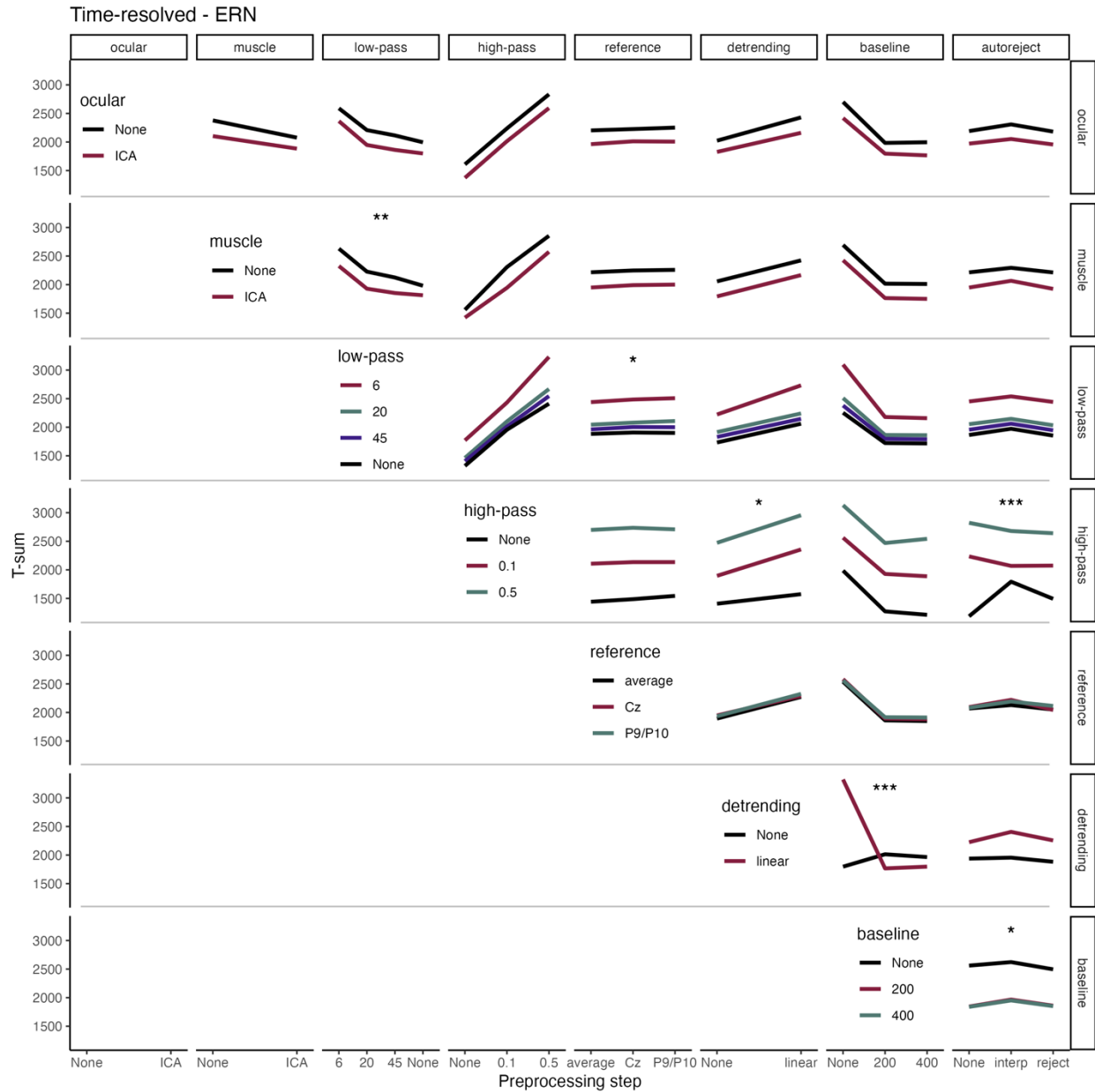


Fig. S12. Interactions between preprocessing steps on decoding performance for ERN and time-resolved decoding.

Horizontal and vertical panels illustrate the different preprocessing steps. The individual preprocessing choices are illustrated on the x-axes and color-coded. The color legends on the diagonal refer to each horizontal panel. T-sum is shown on the y-axes. Stars indicate the significance (*' $p < 0.05$; '**' $p < 0.01$; '***' $p < 0.001$). *Ocular*: ocular artifact correction; *muscle*: muscle artifact correction; *ICA*: independent component analysis, *low-pass*: low-pass filter in Hertz; *high-pass*: high-pass filter in Hertz; *baseline*: baseline interval in milliseconds; *autoreject* version either interpolate (*interp*) or reject artifact-contaminated trials (*reject*).

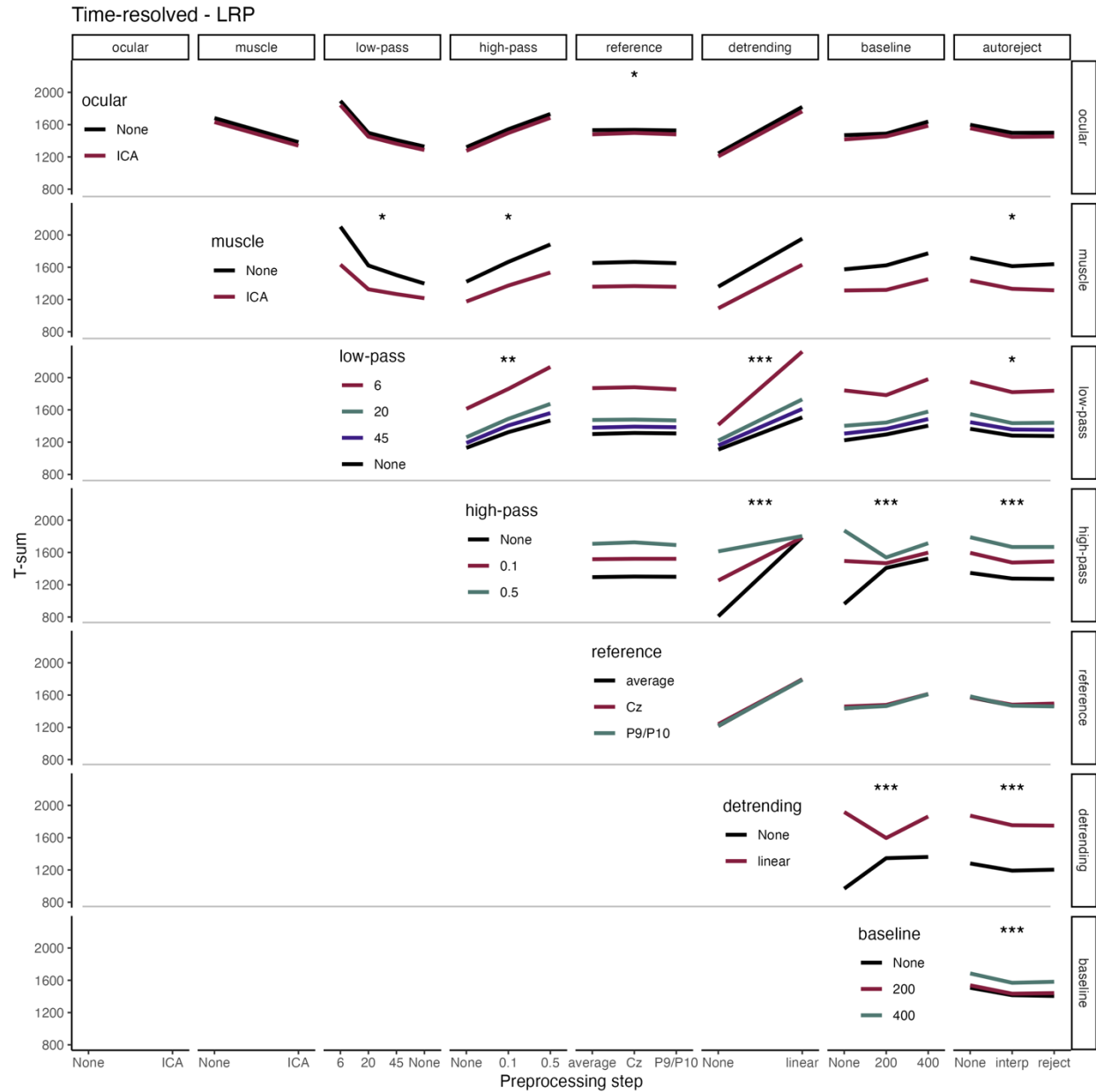


Fig. S13. Interactions between preprocessing steps on decoding performance for LRP and time-resolved decoding.
See Figure S12 for details.

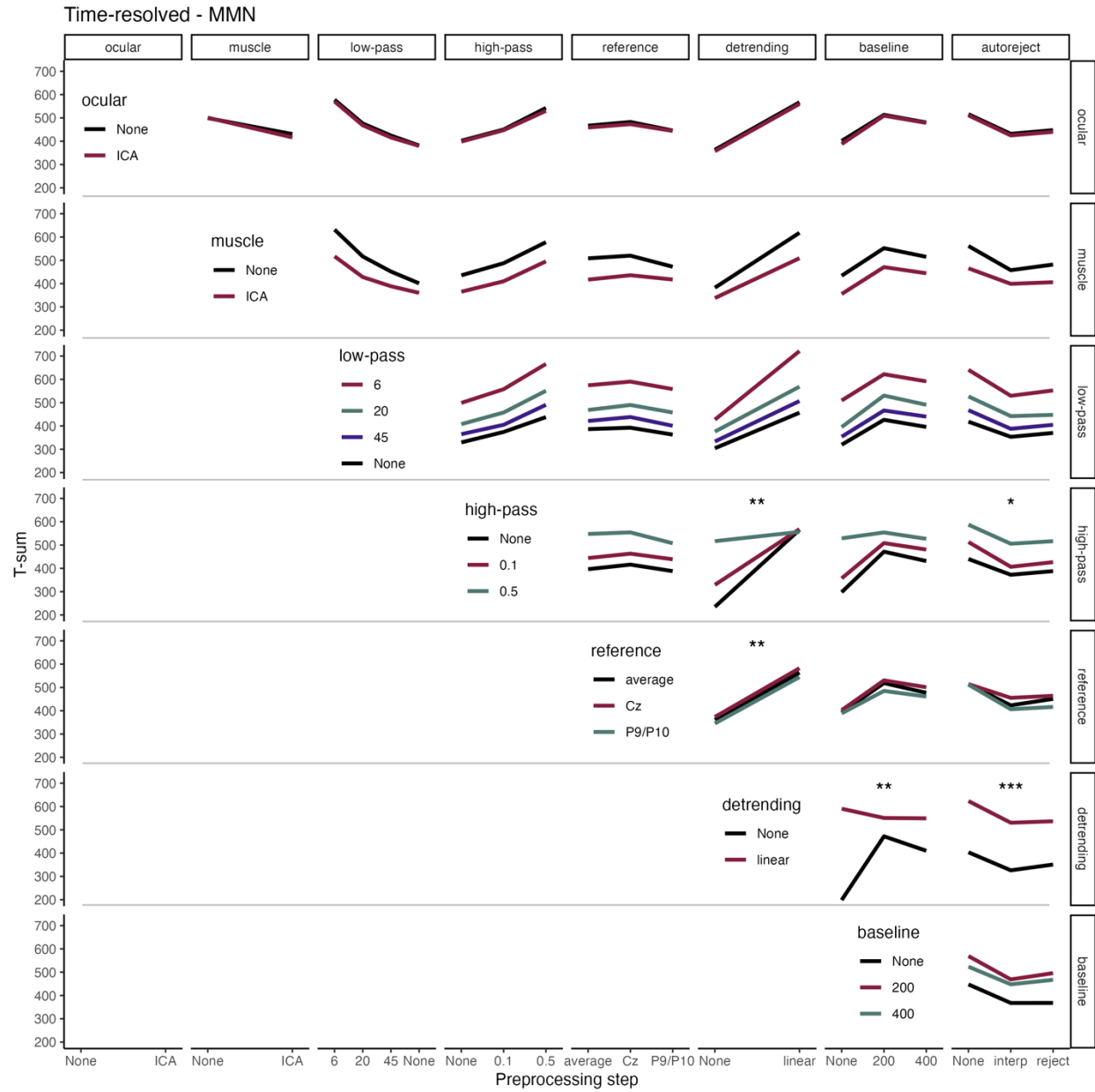


Fig. S14. Interactions between preprocessing steps on decoding performance for MMN and time-resolved decoding.
See Figure S12 for details.

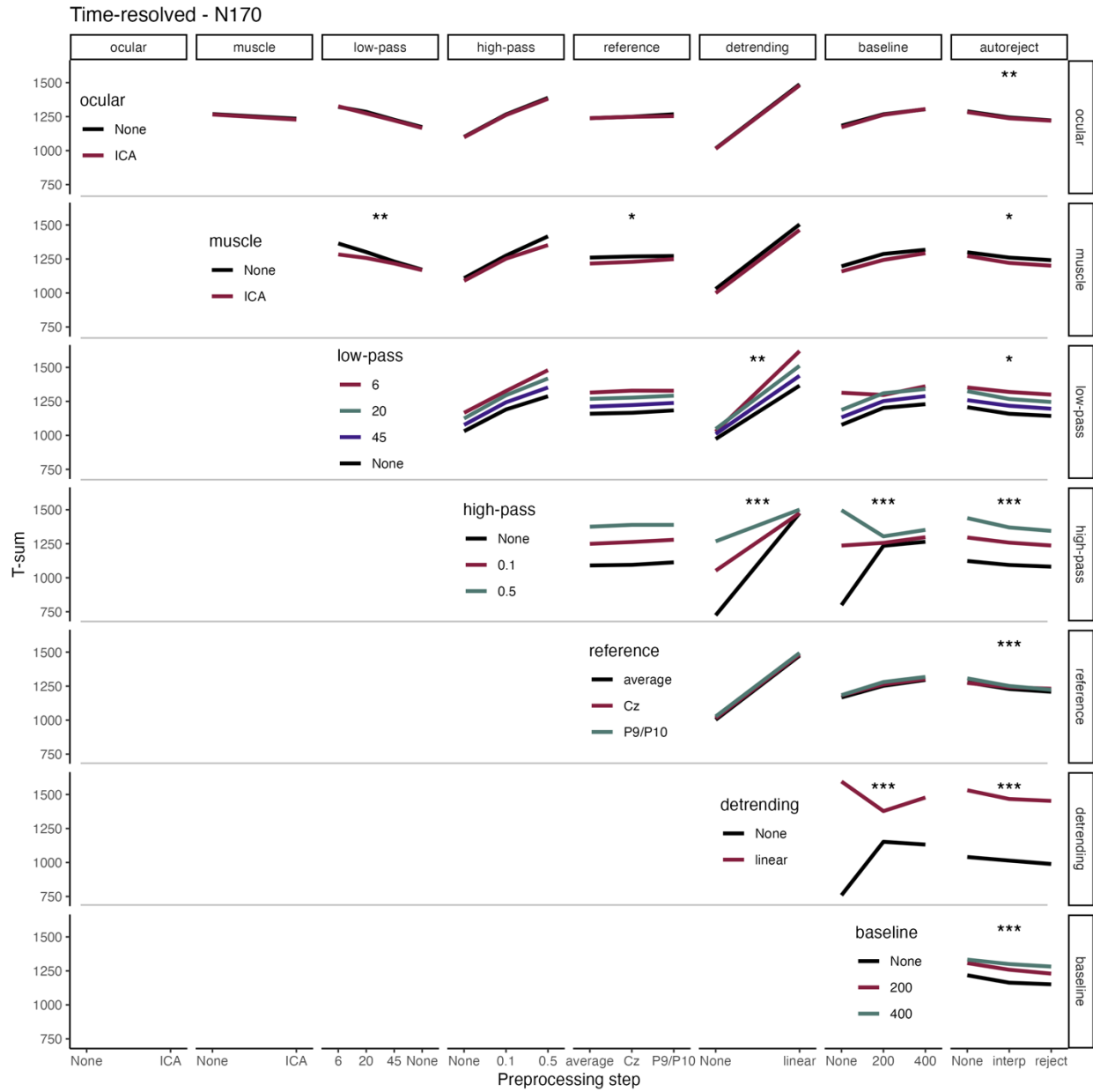


Fig. S15. Interactions between preprocessing steps on decoding performance for N170 and time-resolved decoding.
See Figure S12 for details.

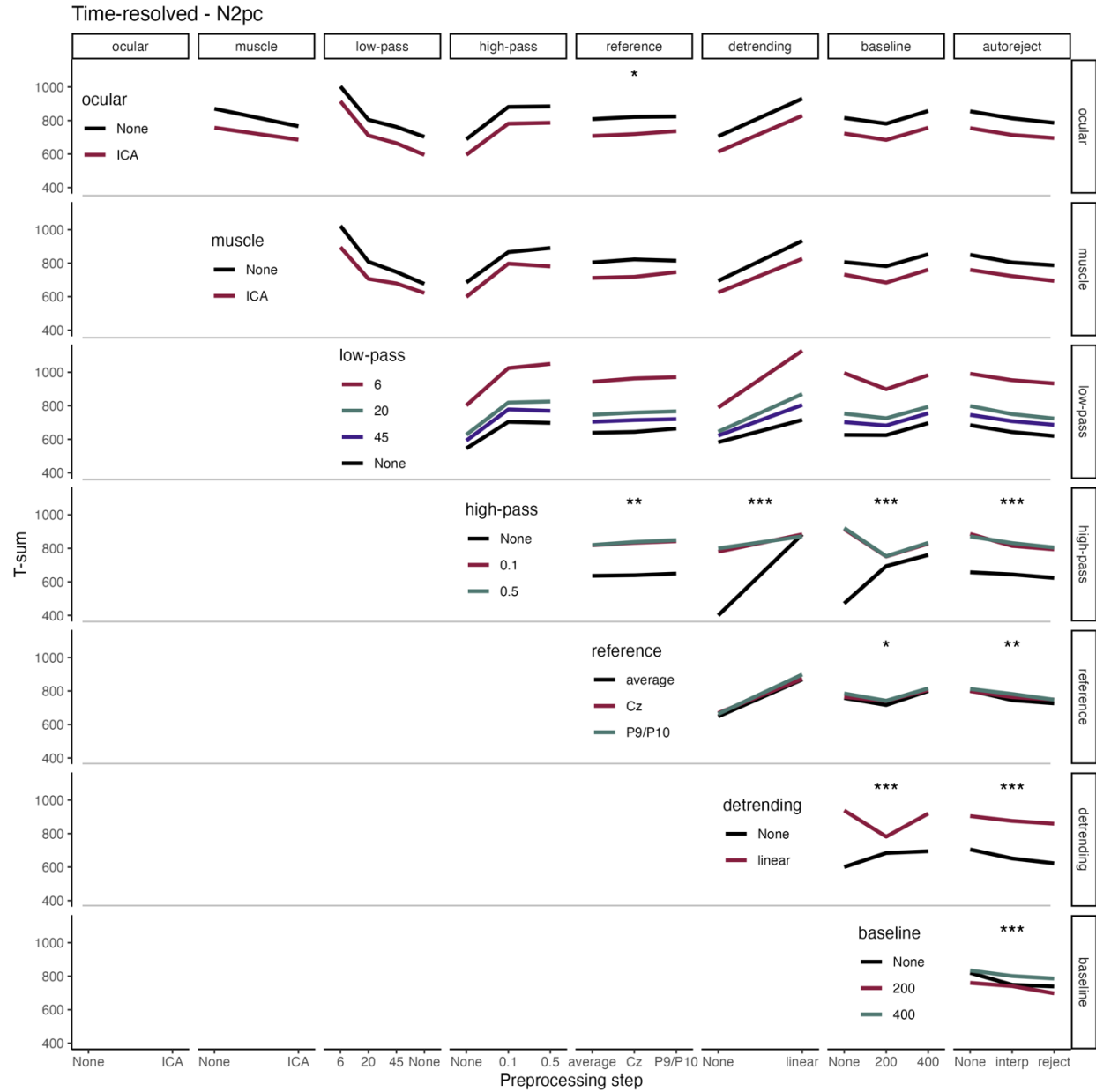


Fig. S16. Interactions between preprocessing steps on decoding performance for N2pc and time-resolved decoding.

See Figure S12 for details.

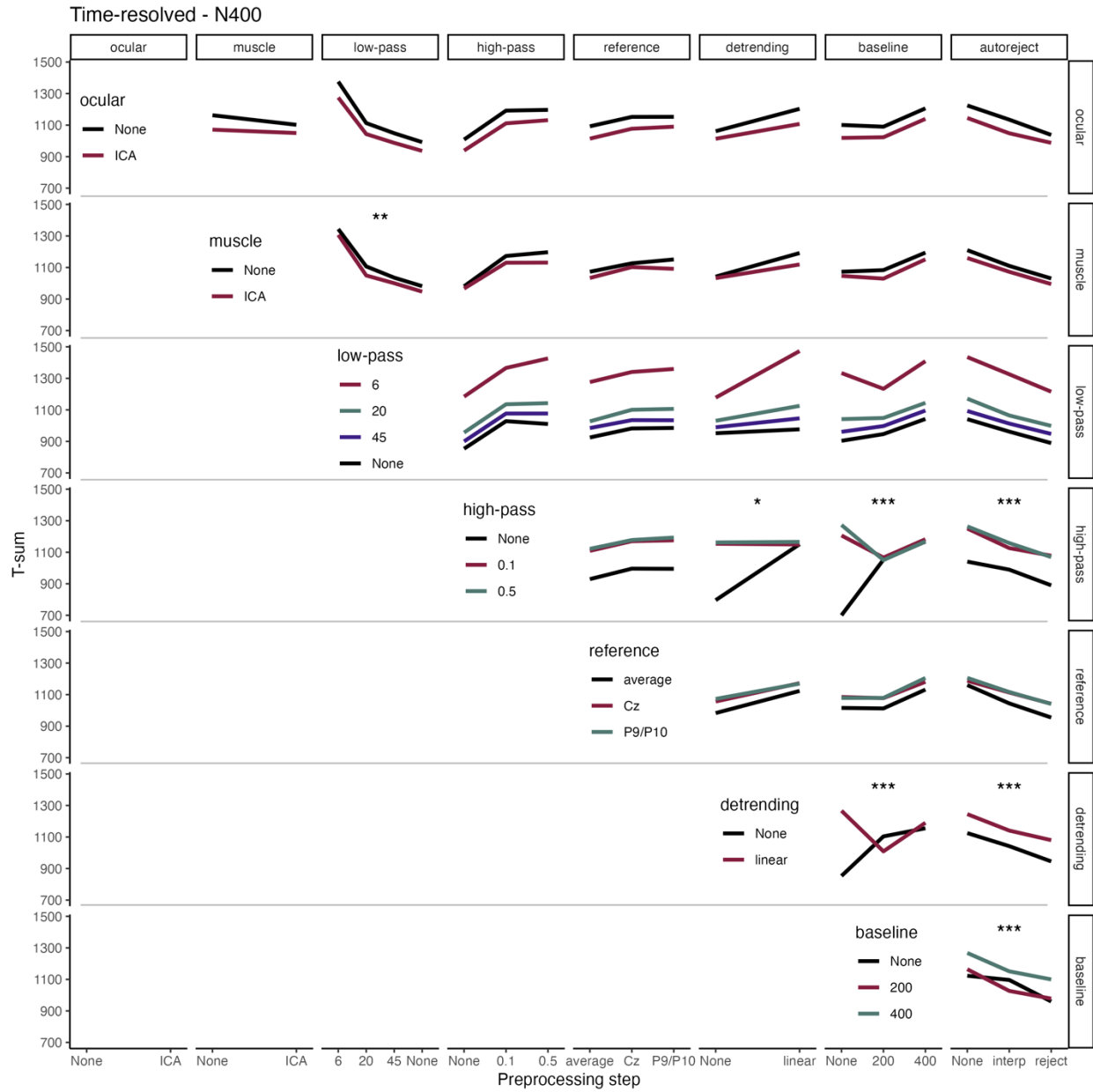


Fig. S17. Interactions between preprocessing steps on decoding performance for N400 and time-resolved decoding.
See Figure S12 for details.

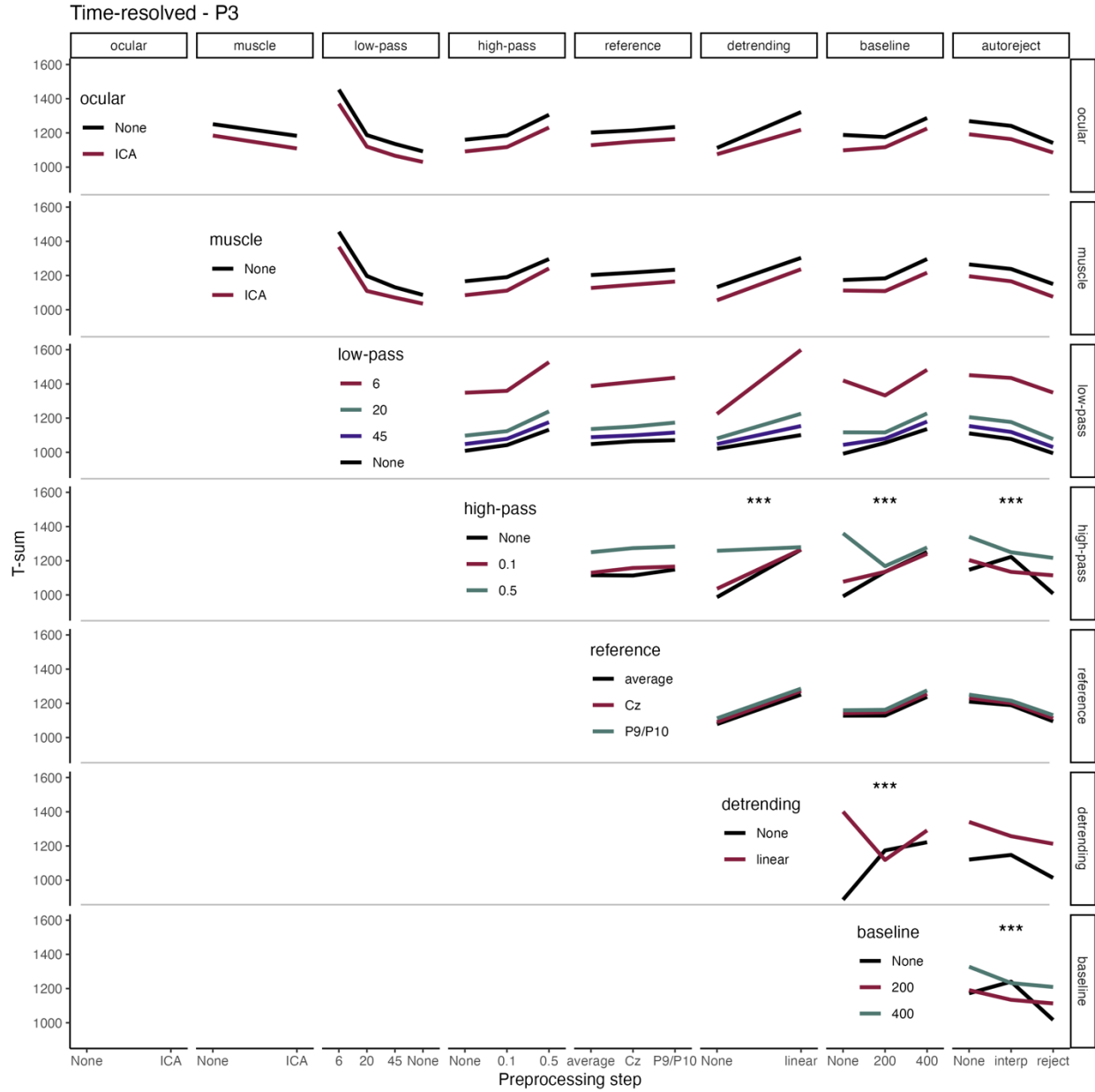


Fig. S18. Interactions between preprocessing steps on decoding performance for P3 and time-resolved decoding.
See Figure S12 for details.

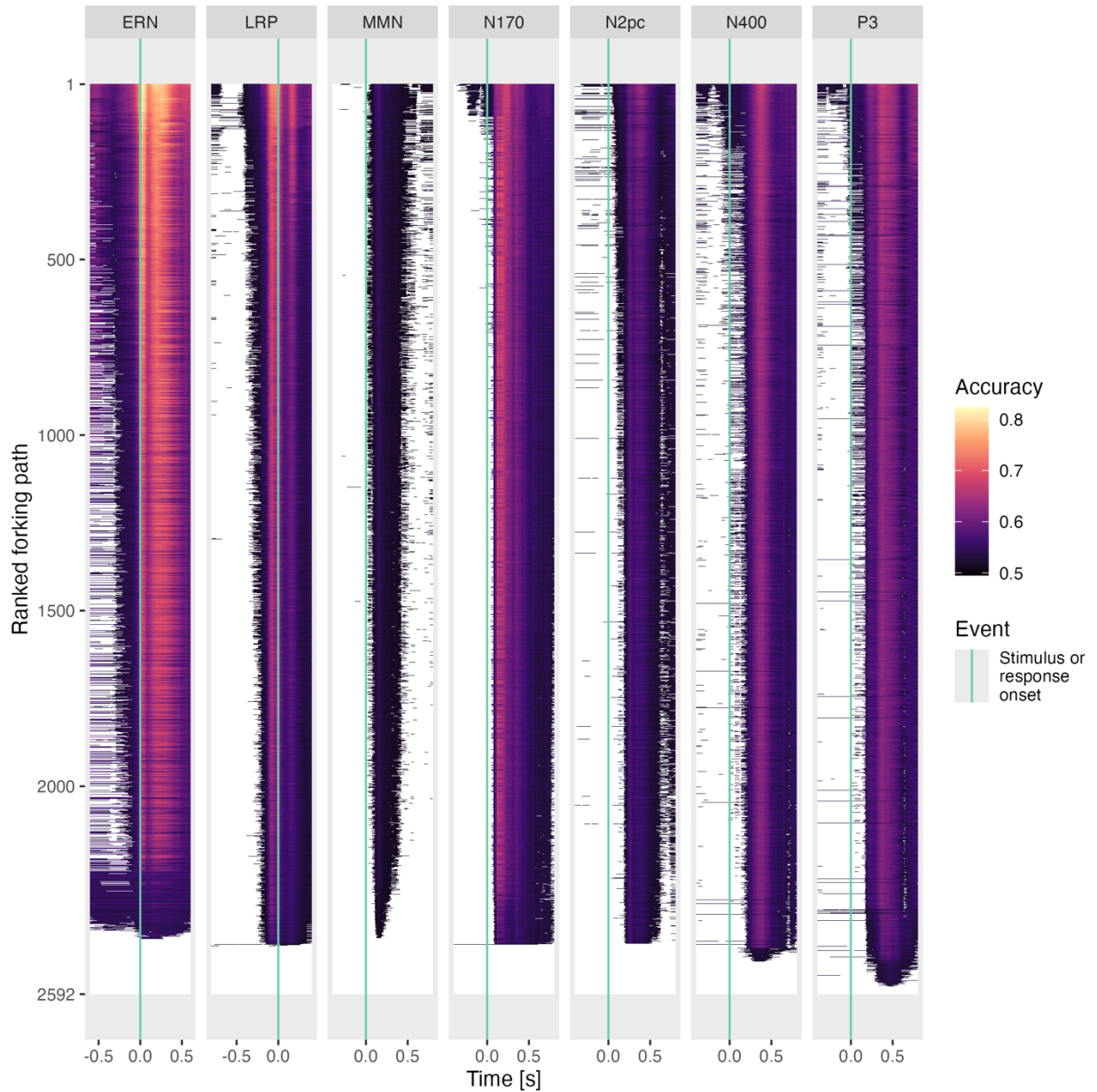


Fig. S19. Time-resolved decoding accuracy for all forking paths.

The decoding accuracy for each time point (x-axes) is color-coded. The forking paths of each experiment (horizontal panels) are ranked based on their T -sum from #1 (best) to #2592 (worst) on the y-axes, and therefore correspond to the forking paths of Figure S5. The vertical aquamarine line illustrates stimulus or response onset (Table S5). Only time points are color-coded, which fall in a significant cluster as defined by cluster-permutation testing.

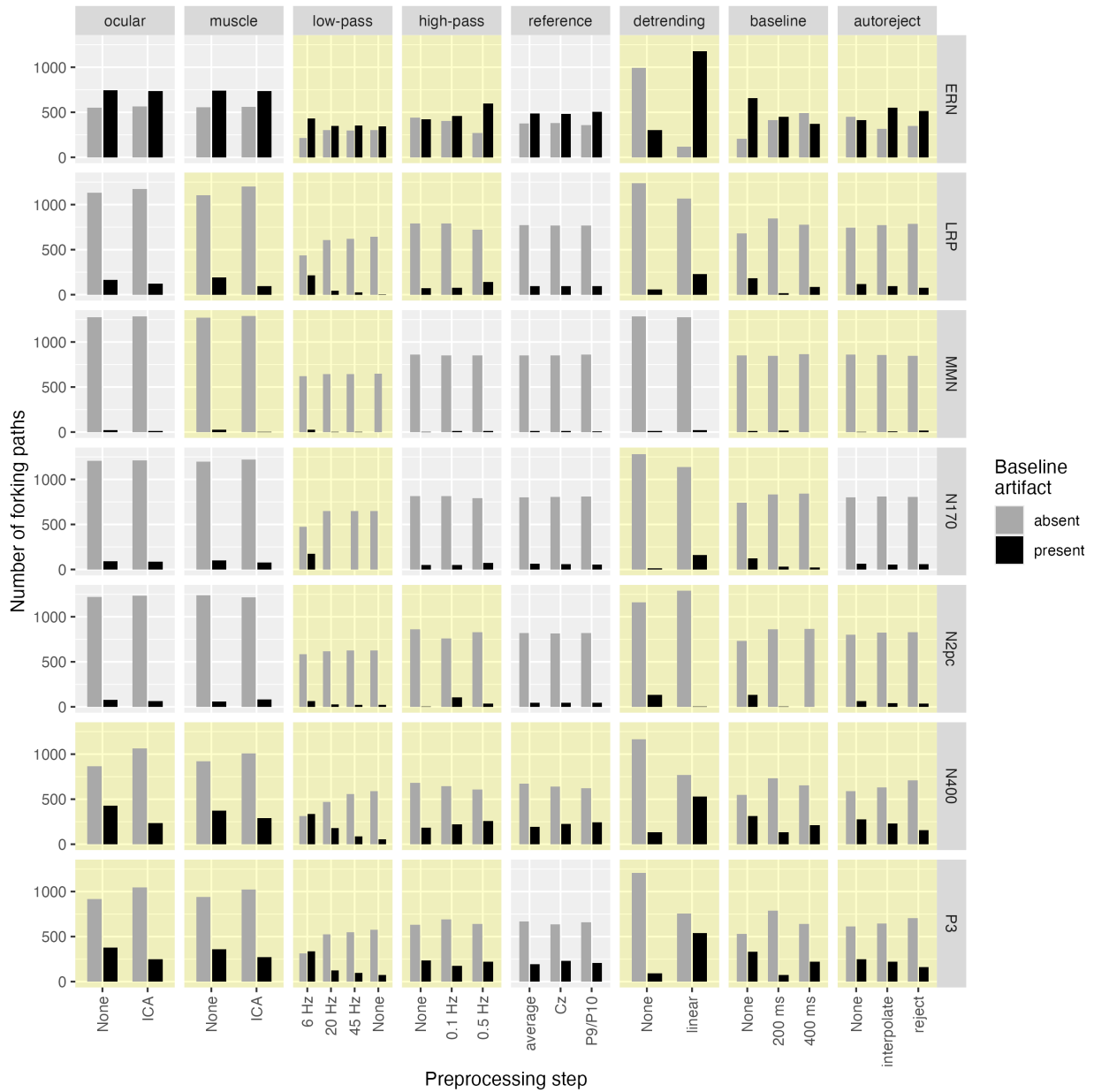


Fig. S20. Influence of preprocessing steps on the presence or absence of a baseline artifact in time-resolved decoding.

For each experiment (vertical panels) and preprocessing step (horizontal panels) and its respective version (x-axes), the number of forking paths producing a so-called baseline artifact during time-resolved decoding is counted (y-axes). Grey bars illustrate the number of forking paths without such an artifact, and black bars the number of forking paths with such an artifact. Yellow facets indicate significant likelihood ratio tests ($p < 0.01$) of a processing step within an experiment.

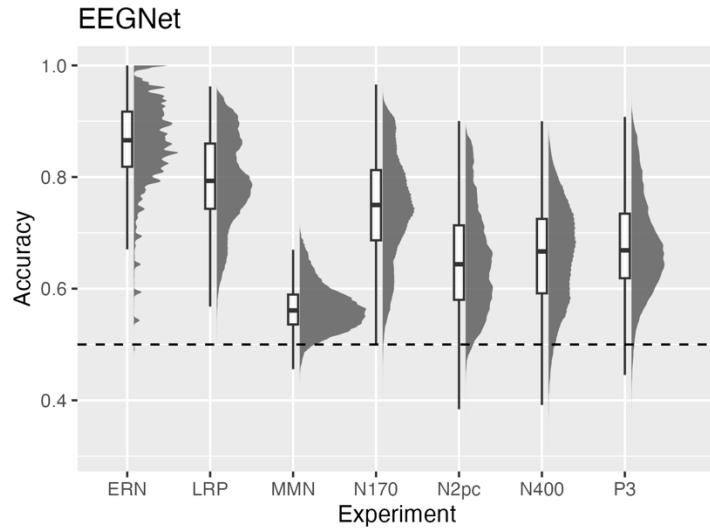


Fig. S21. Overview of EEGNet decoding accuracies.

(Balanced) Decoding accuracies (y-axis) are illustrated for each forking path and participant, separately for each experiment (x-axis). Contrary to Figure 3A, no averaging across participants was performed for each forking path. One can observe the higher variability in decoding accuracy when not removing the participant variability compared to Figure 3A. Boxes represent the interquartile range (25th to 75th percentile), with the median indicated by a solid black line. Whiskers extend to the most extreme values within 1.5 times the interquartile range from the lower and upper quartiles.

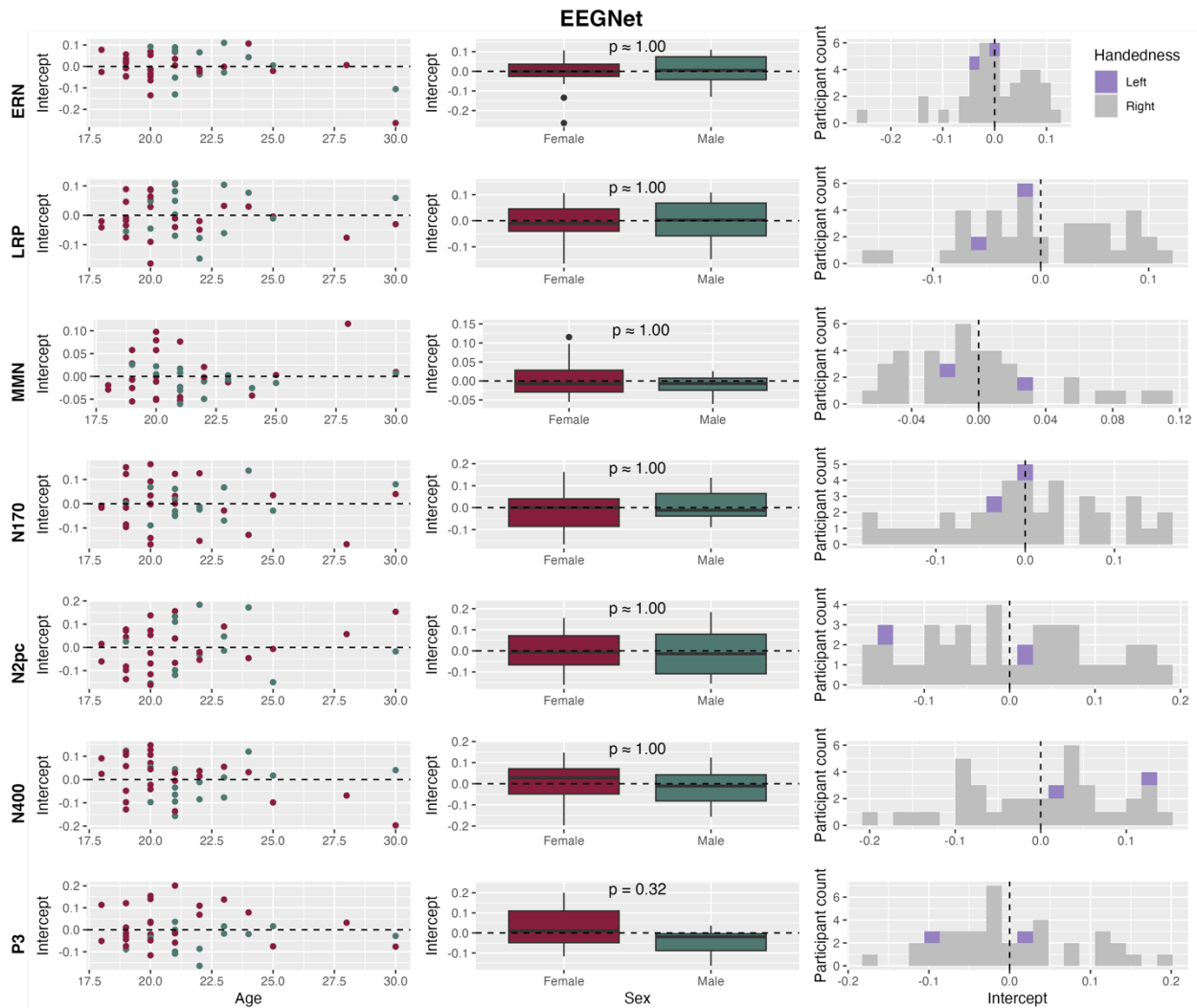


Fig. S22. Relation between random intercepts and participant demographics using EEGNet.

For each experiment (row), each participant's random intercept – i.e., the individual offset in decoding accuracy – are plotted against demographic variables (see Supplementary Text – Influence of the participant in the LMMs). Left column: The relationship between age and random intercept, grouped by sex (red = female, green = male). Middle column: The association between sex and random intercept. P -values represent the results of a false discovery rate-corrected Man-Whitney U test using the Benjamini Hochberg adjustment. No association was significant. Boxes represent the interquartile range (25th to 75th percentile), with the median indicated by a solid black line. Whiskers extend to the most extreme values within 1.5 times the interquartile range from the lower and upper quartiles. Data points beyond this range are shown as outliers. Right column: Histogram of the relationship between random intercept and handedness. Only two participants in the dataset were left-handed.

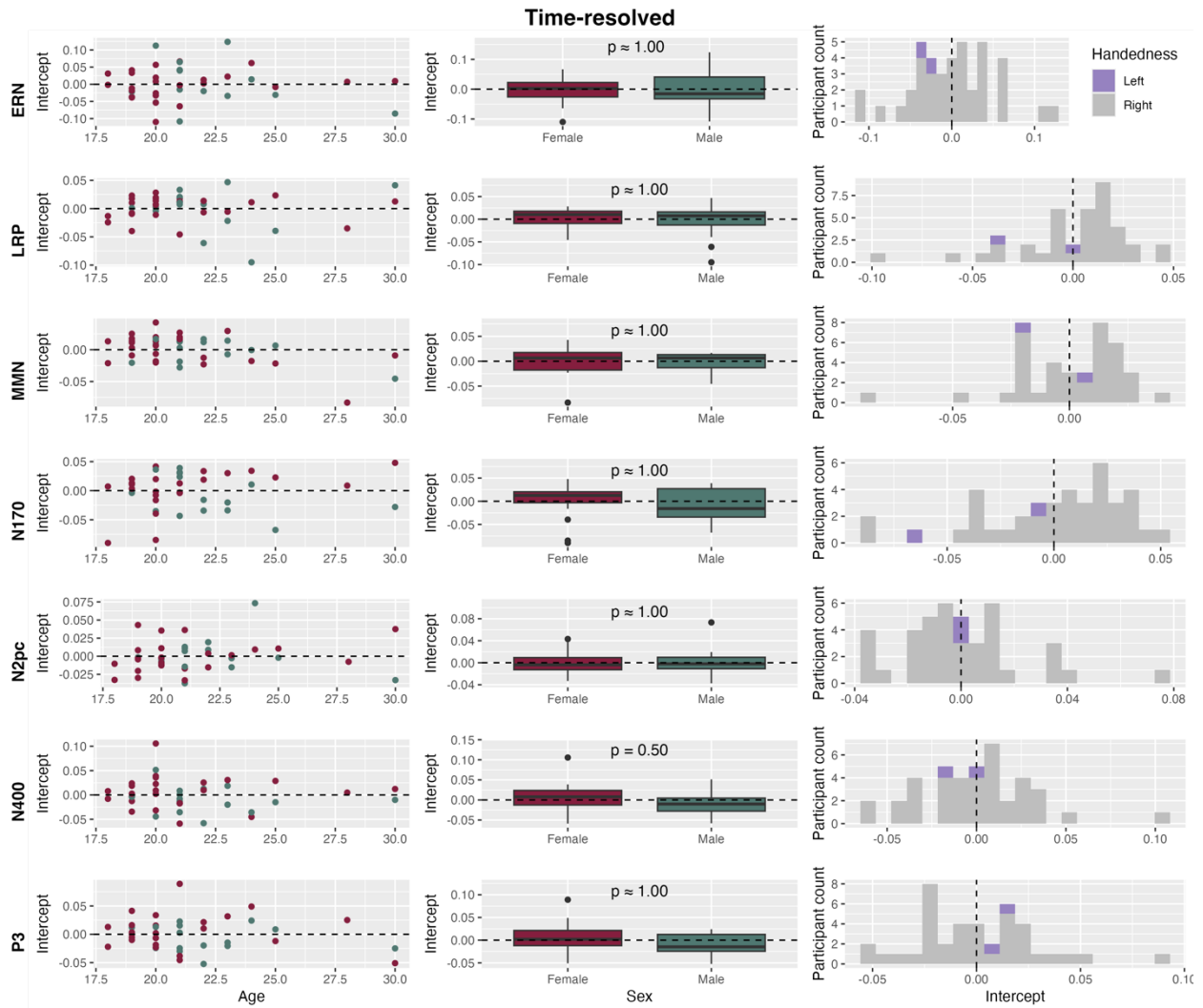


Fig. S23. Relation between random intercepts and participant demographics using time-resolved decoding.

See Figure S22 for details. No association was significant.

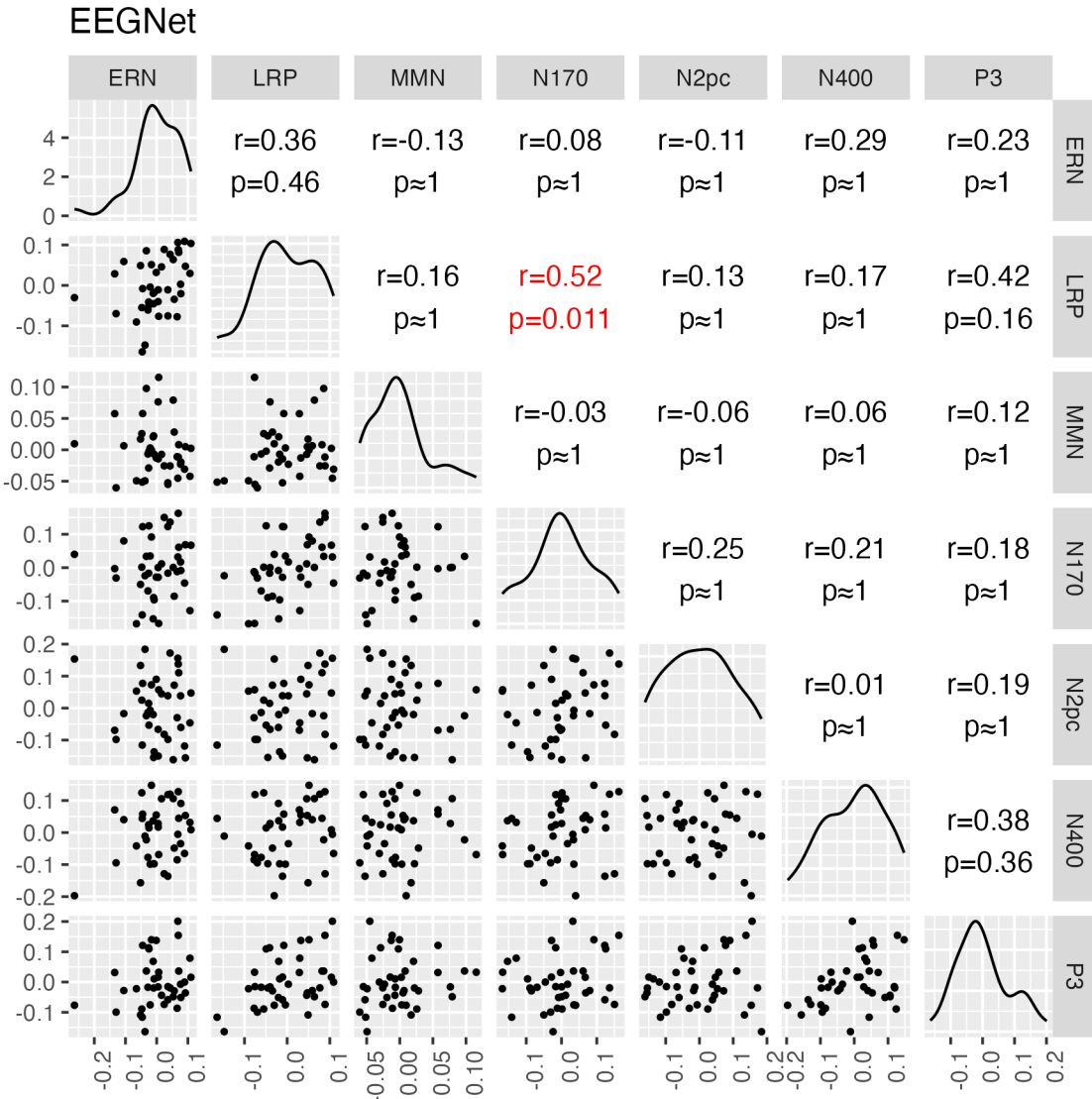


Fig. S24. Correlations of random intercepts between experiments (EEGNet decoding). Pairwise Pearson correlations were computed, correlating the random intercepts of the same participants but in two different experiments and therefore extracted from two different LMMs (see Supplementary Text – Influence of the participant in the LMMs). The lower diagonal illustrates the random intercepts of the same participants but across two experiments and LMMs, extracted from these LMMs. The on-diagonal elements show a kernel density estimate of the distributions. The upper diagonal illustrates the Pearson correlation coefficients and associated false discovery rate-corrected p -values.

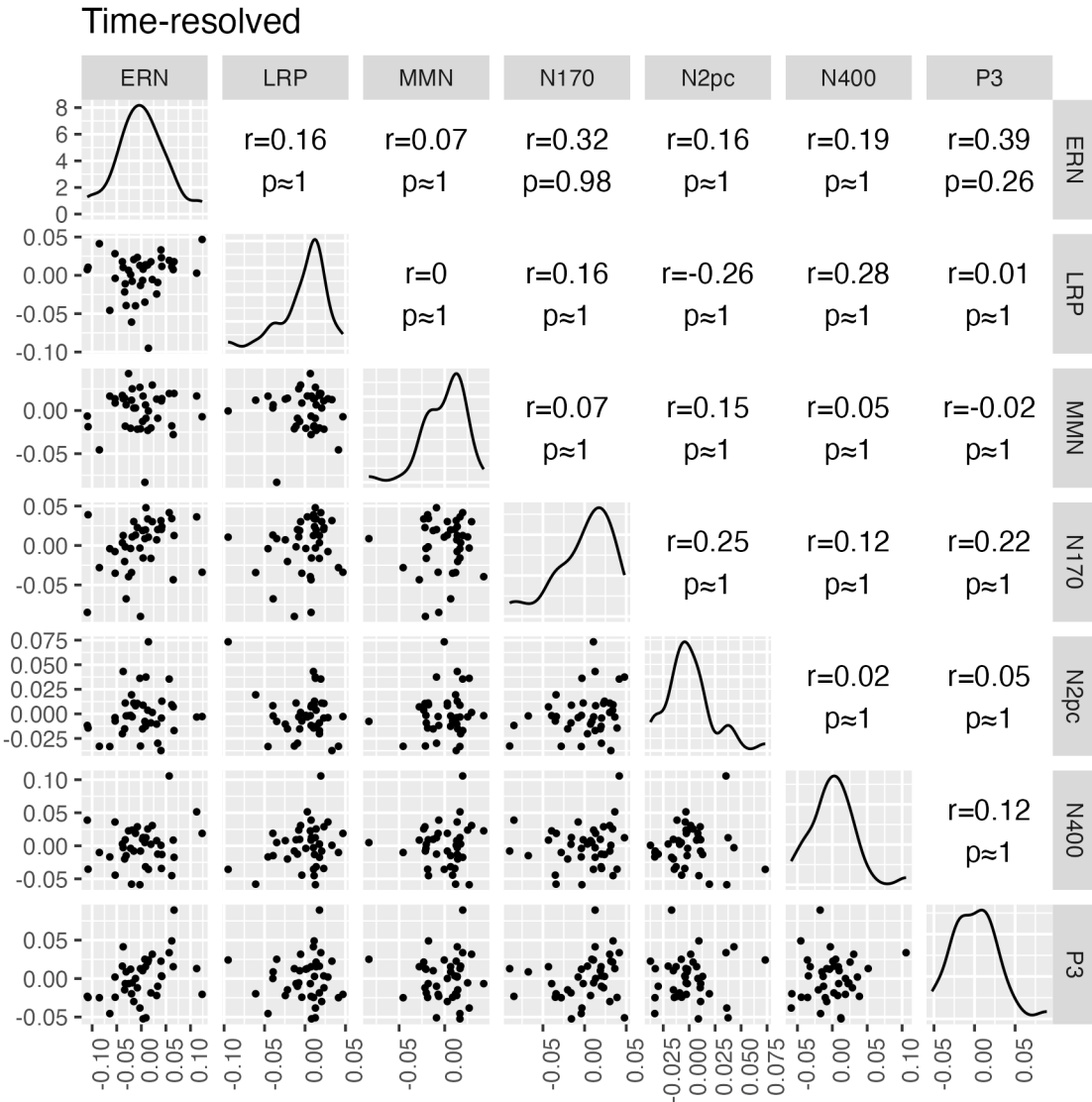


Fig. S25. Correlations of random intercepts between experiments (time-resolved decoding).
See Figure S24 for details.

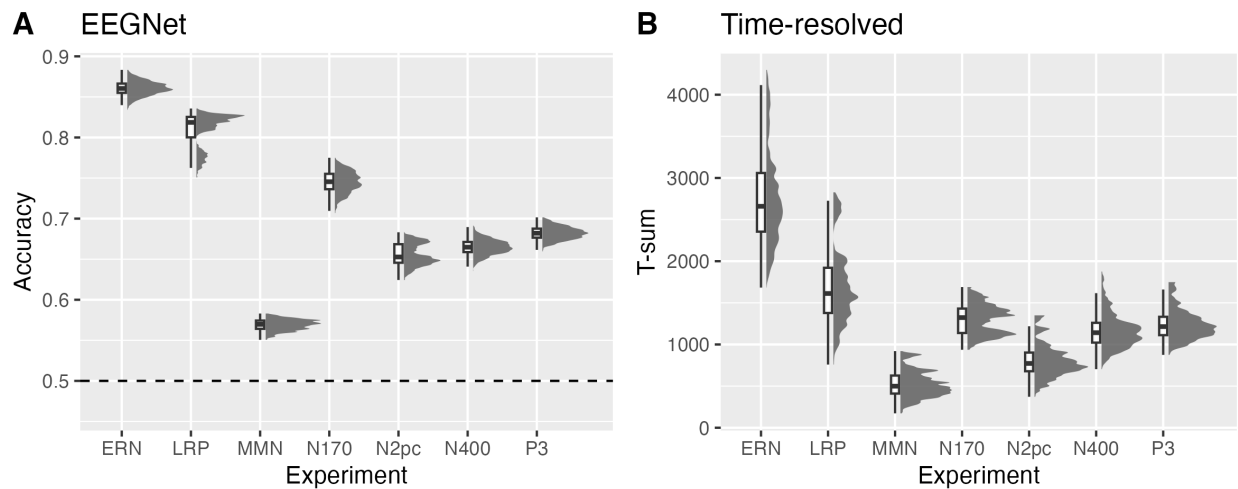


Fig. S26. Overview of decoding performances in an alternative multiverse.

The alternative multiverse comprised a different order of preprocessing steps, i.e. (1) re-referencing, (2) HPF & LPF, (3) ocular artifact correction, (4) muscle artifact correction, (5) baseline correction & detrending, and (6) autoreject (see Supplementary Text – Alternative order of preprocessing steps). **A:** (Balanced) Decoding accuracies (y-axis) are plotted for each forking path (averaged across participants), separately for each experiment (x-axis). **B:** *T*-sums (y-axis) are plotted for each forking path and across participants, separately for each experiment (x-axis). Boxes represent the interquartile range (25th to 75th percentile), with the median indicated by a solid black line. Whiskers extend to the most extreme values within 1.5 times the interquartile range from the lower and upper quartiles.



Fig. S27. Influence of preprocessing steps on decoding performance in an alternative multiverse.

The alternative multiverse comprised a different order of preprocessing steps, i.e. (1) re-referencing, (2) HPF & LPF, (3) ocular artifact correction, (4) muscle artifact correction, (5) baseline correction & detrending, and (6) autoreject (see Supplementary Text – Alternative order of preprocessing steps). Percentage deviation from marginal means of either decoding accuracy (EEGNet, **A**) or *T*-sum (time-resolved, **B**) are depicted within each tile. Marginal means for each level (x-axis) of preprocessing step (horizontal panels) are normalized to the mean of the respective experiment (vertical panels), and shows the percentage differences in relation to this mean value, and not the absolute improvement or decline in decoding accuracy as a percentage. Color scales differ in **A** and **B**. All cells are colored. The horizontal panels are ordered according to the preprocessing steps in the pipeline. The order differs with respect to Figure 5. See Figure 5 for details.

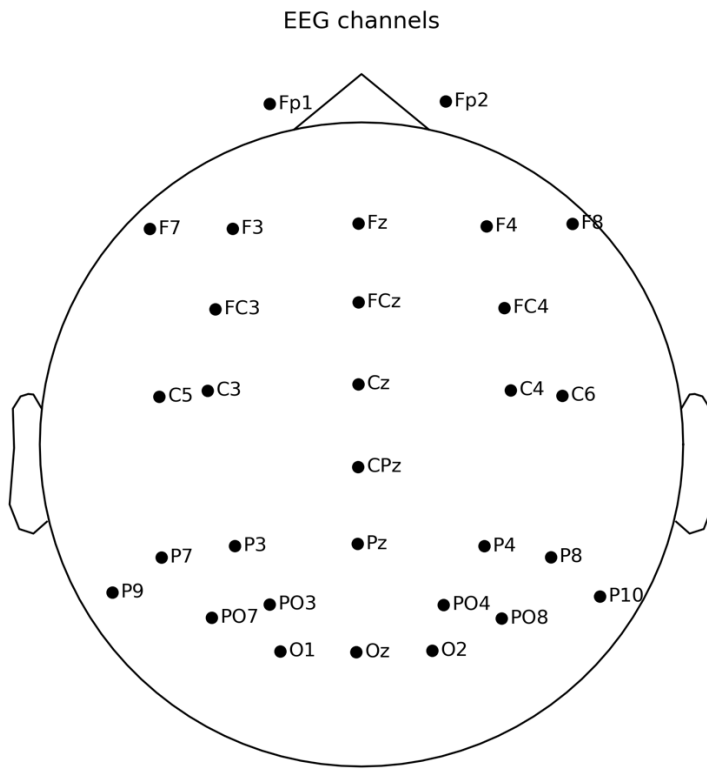


Fig. S28. Schematic of the EEG montage.

30 scalp electrodes were recorded along with three EOG electrodes (not shown).

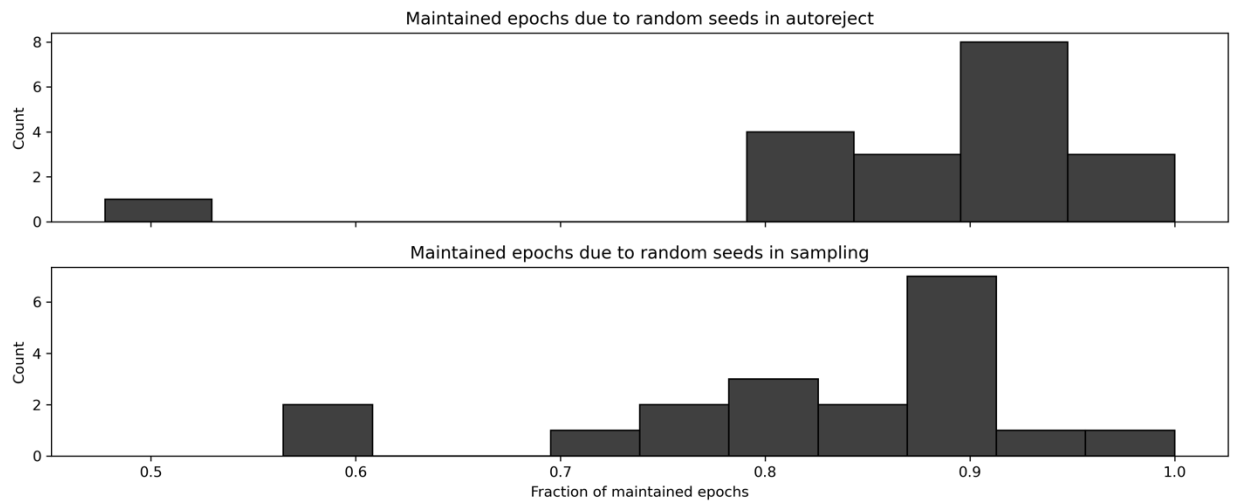


Fig. S29. Fraction of maintained epochs for different seeds.

Autoreject was deployed using one example participant of the ERN experiment (see Supplementary Text – Variability due to random seed in autoreject). The fraction of maintained epochs (x-axes) for different random seeds was counted across seeds (y-axes). Upper panel: Seed varied in autoreject function. Lower panel: Seed varied in epoch sampling.

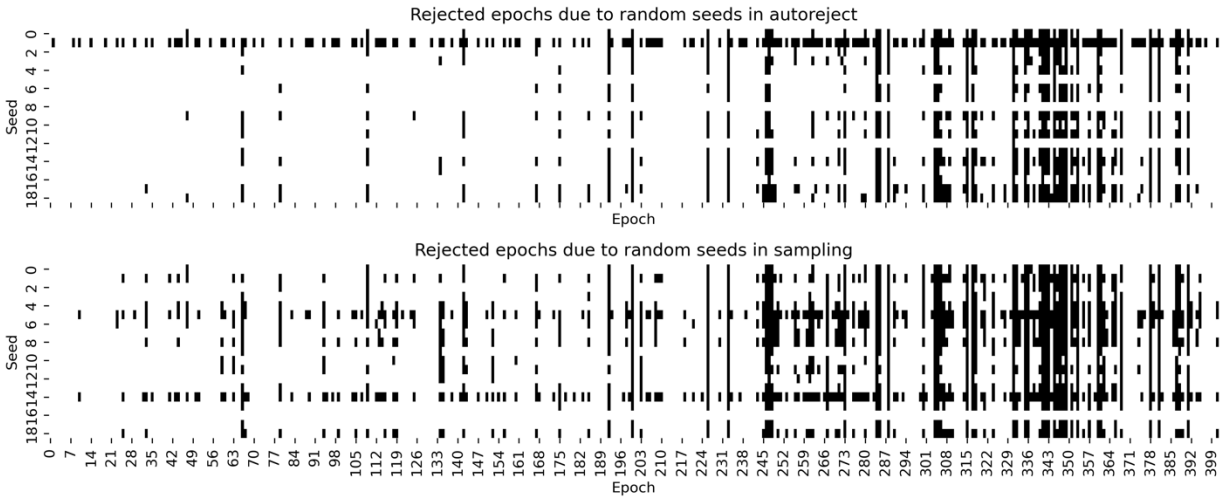


Fig. S30. Rejected epochs for different seeds.

Autoreject was deployed using one example participant of the ERN experiment (see Supplementary Text – Variability due to random seed in autoreject). For each epoch (x-axes) and random seed (y-axes), black tiles indicate rejection of an epoch due to exceeding the estimated threshold, whereas white tiles indicate epochs which were maintained. Upper panel: Seed varied in autoreject function. Lower panel: Seed varied in epoch sampling.

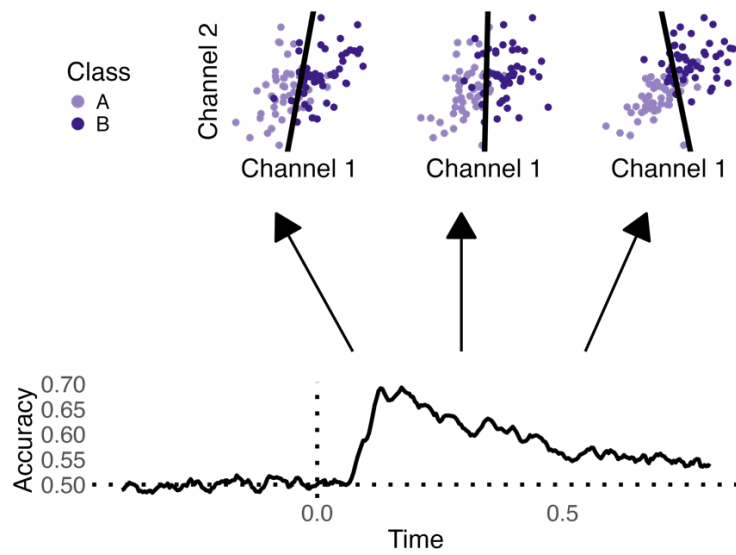


Fig. S31. Schematic of time-resolved decoding.

In time-resolved decoding analysis, all channel values (here, electrode voltages) from all trials at each respective time point are used to train and test binary classifiers (top panel). In the present study, logistic regressions were used. The (cross-validated, balanced) test accuracies are then written into a decoding time series (lower panel), which is further analyzed across participants.

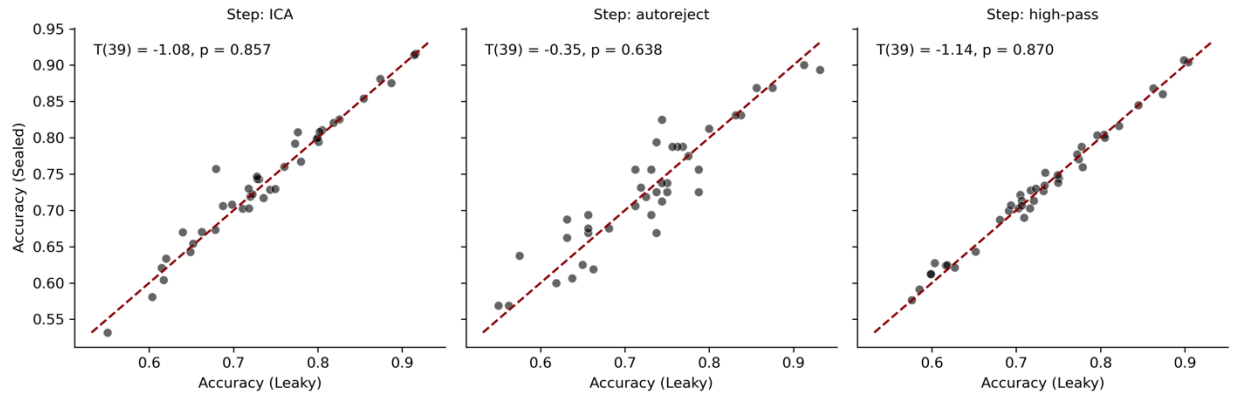


Figure S32: The influence of latent leakage on decoding performance. For the N170 experiment and some example forking paths, we preprocessed the data using a sealed and a leaky version of some processing steps, i.e., ICA, autoreject, and HPF (see Supplementary Text – Influence of latent leakage on decoding performance). We fitted an EEGNet classifier for each participant and pipeline. Balanced accuracy estimates are plotted for the sealed (y-axes) versus the leaky (x-axes) versions and each processing step (horizontal facets). The dashed red line indicates the identity line. One-tailed paired-sampled T -tests did not indicate higher accuracies for leaky pipelines (all $p > 0.638$).

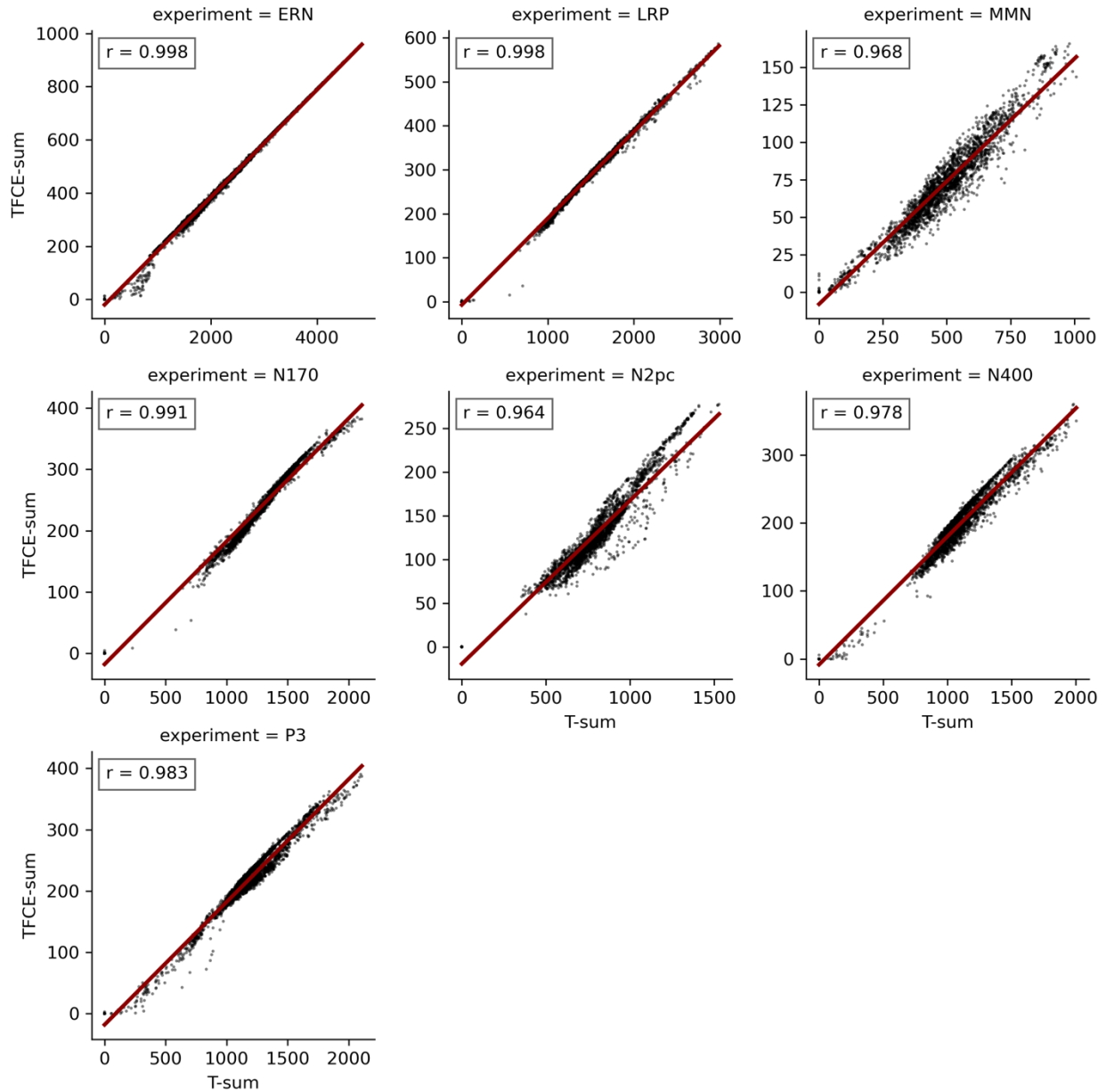


Figure S33: Correlation between $TFCE$ -sum and T -sum per experiment. We first used an arbitrary cluster-forming threshold (corresponding to $p < 0.05$) and secondly $TFCE$ (hyperparameters: start = 0, step = 0.2), and quantified the T -sums (x-axes) or $TFCE$ -sums (y-axes), separately for each forking path and experiment across participants. Red lines represent linear fits to the data. Both measures were strongly correlated across forking paths (Pearson correlation, all $r > 0.96$).

Model performance with and without interactions

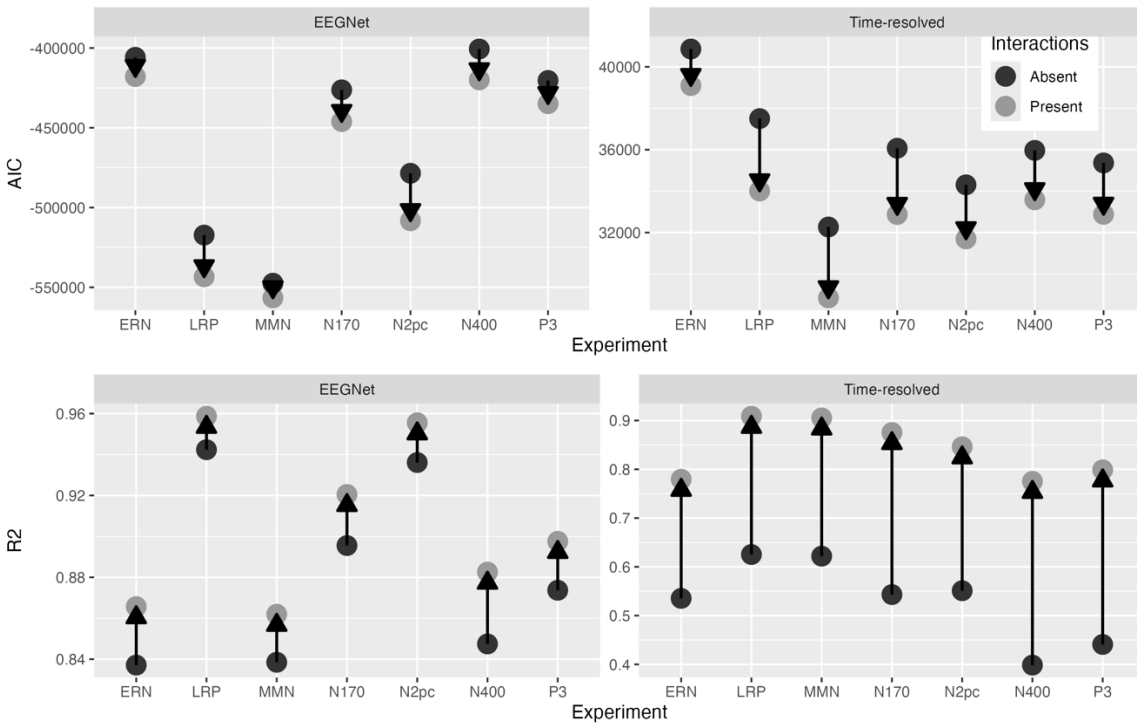


Fig. S34. AIC and R^2 values for models without interactions and models with two-way interactions included.

AIC values (upper facets) and R^2 values (lower panels) are illustrated for models without interactions (black dots) or with two-way interactions (gray dots). Models are LMMs for EEGNet (left panels) and LMs for time-resolved decoding (right panels). Arrows indicate the change from models without interactions towards models with interactions. Including interaction terms consistently decreased AIC values, supporting the decision to include these terms in our model. The R^2 values from EEGNet compared to time-resolved models were already high without interaction values (note different scales of y-axes), indicating that a large fraction of variance was already explained by the main effects.

Table S1.

Significant effects of preprocessing on EEGNet decoding performance, separately for each experiment. *F*-tests were performed for each processing step. Stars indicate the significance ('. ' $p < 0.1$; '*' $p < 0.05$; '**' $p < 0.01$; '***' $p < 0.001$). *Ocular*: ocular artifact correction; *muscle*: muscle artifact correction; *ICA*: independent component analysis, *low-pass*: low-pass filter; *high-pass*: high-pass filter.

model term	ERN	LRP	MMN	N170	N2pc	N400	P3
ocular					*		
muscle		***	**		*	.	
low-pass	.			***			
high-pass	***	***		**	*		
reference	**	.	.	*		**	
detrending		**	**	***			
baseline	*	***		***	***	***	***
autoreject	***	***	**	***	**	.	***
ocular:muscle	.						
ocular:low-pass							
ocular:high-pass			.				
ocular:reference		*			*		
ocular:detrending					.		
ocular:baseline							
ocular:autoreject				**			
muscle:low-pass	**	*		**		**	
muscle:high-pass		*					
muscle:reference				*			
muscle:detrending	.		.				
muscle:baseline		.					
muscle:autoreject		*		*			.
low-pass:high-pass		**					
low-pass:reference	*			.			
low-pass:detrending	.	***		**			.
low-pass:baseline							
low-pass:autoreject		*		*			.
high-pass:reference					**		
high-pass:detrending	*	***	**	***	***	*	***
high-pass:baseline		***	.	***	***	***	***
high-pass:autoreject	***	***	*	***	***	***	***
reference:detrending			**				
reference:baseline					*		
reference:autoreject		.		***	**		
detrending:baseline	***	***	**	***	***	***	***
detrending:autoreject		***	***	***	***	***	.
baseline:autoreject	*	***	.	***	***	***	***

Table S2.

Significant effects of preprocessing on time-resolved decoding performance, separately for each experiment. See Table S1 for details.

model term	ERN	LRP	MMN	N170	N2pc	N400	P3
ocular	***	***	**		***	***	***
muscle	***	***	***	***	***	***	***
low-pass	***	***	***	***	***	***	***
high-pass	***	***	***	***	***	***	***
reference	.		***	**	***	***	***
detrending	***	***	***	***	***	***	***
baseline	***	***	***	***	***	***	***
autoreject	***	***	***	***	***	***	***
ocular:muscle	*		***		***	**	
ocular:low-pass						*	
ocular:high-pass							
ocular:reference							
ocular:detrending	*					***	***
ocular:baseline	.						*
ocular:autoreject						*	
muscle:low-pass	*	***	***	***	***		*
muscle:high-pass	***	***		***	***	**	.
muscle:reference			***		**	.	
muscle:detrending		***	***		***	***	
muscle:baseline		***			.		
muscle:autoreject		**	***				
low-pass:high-pass	***	***	***	*	***	**	***
low-pass:reference							
low-pass:detrending	***	***	***	***	***	***	***
low-pass:baseline	***	***	*	***	***	***	***
low-pass:autoreject			***			**	
high-pass:reference			***				
high-pass:detrending	***	***	***	***	***	***	***
high-pass:baseline	**	***	***	***	***	***	***
high-pass:autoreject	***	*	***	*	***	***	***
reference:detrending					*	*	
reference:baseline			***				
reference:autoreject			***		.	*	
detrending:baseline	***	***	***	***	***	***	***
detrending:autoreject	***	*	***	*	**	.	***
baseline:autoreject			***		***	***	***

Table S3.

For each experiment, pairwise post-hoc comparisons in EEGNet decoding performance within each preprocessing step using Tukey adjustment. See Table S1 for details.

variable	level 1	level 2	ERN	LRP	MMN	N170	N2pc	N400	P3
ocular	None	ICA					*		
muscle	None	ICA		***	**		*	.	
low-pass	None	6 Hz	.			***			
low-pass	None	20 Hz							
low-pass	None	45 Hz							
low-pass	6 Hz	20 Hz	*			***			
low-pass	6 Hz	45 Hz	*			***			
low-pass	20 Hz	45 Hz							
high-pass	None	0.1 Hz	.	**		*			
high-pass	None	0.5 Hz	**	***	.	*			
high-pass	0.1 Hz	0.5 Hz							
reference	average	Cz	**					*	
reference	average	P9/P10		*	.	*		*	
reference	Cz	P9/P10	*						
detrending	None	linear		**	**	***			
baseline	None	200 ms		***		**	***	*	**
baseline	None	400 ms		***		***	***	**	***
baseline	200 ms	400 ms							
autoreject	None	interpolate	**	***	*	***	.		***
autoreject	None	reject	**	***		**	*		*
autoreject	interpolate	reject							

Table S4.

For each experiment, pairwise post-hoc comparisons in time-resolved decoding performance within each preprocessing step using Tukey adjustment. See Table S1 for details.

variable	level 1	level 2	ERN	LRP	MMN	N170	N2pc	N400	P3
ocular	None	ICA	***	***	**		***	***	***
muscle	None	ICA	***	***	***	***	***	***	***
low-pass	None	6 Hz	***	***	***	***	***	***	***
low-pass	None	20 Hz	***	***	***	***	***	***	***
low-pass	None	45 Hz	**	***	***	***	***	***	***
low-pass	6 Hz	20 Hz	***	***	***	***	***	***	***
low-pass	6 Hz	45 Hz	***	***	***	***	***	***	***
low-pass	20 Hz	45 Hz	**	***	***	***	***	***	***
high-pass	None	0.1 Hz	***	***	***	***	***	***	***
high-pass	None	0.5 Hz	***	***	***	***	***	***	***
high-pass	0.1 Hz	0.5 Hz	***	***	***	***			***
reference	average	Cz			***		.	***	*
reference	average	P9/P10	.		***	*	***	***	***
reference	Cz	P9/P10			***				*
detrending	None	linear	***	***	***	***	***	***	***
baseline	None	200 ms	***	**	***	***	***		
baseline	None	400 ms	***	***	***	***	***	***	***
baseline	200 ms	400 ms		***	***	***	***	***	***
autoreject	None	interpolate	***	***	***	***	***	***	***
autoreject	None	reject		***	***	***	***	***	***
autoreject	interpolate	reject	***		***	**	***	***	***

Table S5.

Time-locking events, epoch intervals, and baseline reference and intervals. The total duration of the epochs is kept equal across experiments. The baseline interval varied per forking path, either not applied, or a window of 200 ms or 400 ms. The illustrated baseline intervals are with respect to the baseline reference. The illustrated epoch intervals are with respect to the time-locking event. The length of the entire trials and the post-baseline time windows was kept equal between forking paths.

experiment/ component	time-locking event	epoch interval [ms]	baseline reference	baseline interval [ms]	
				200 ms	400 ms
ERN	response	(-600; 600)	stimulus	(-200; 0)	(-400; 0)
LRP	response	(-800; 400)	response	(-600; -400)	(-800; -400)
MMN	stimulus	(-400; 800)	stimulus	(-200; 0)	(-400; 0)
N170	stimulus	(-400; 800)	stimulus	(-200; 0)	(-400; 0)
N2pc	stimulus	(-400; 800)	stimulus	(-200; 0)	(-400; 0)
N400	stimulus	(-400; 800)	stimulus	(-200; 0)	(-400; 0)
P3	stimulus	(-400; 800)	stimulus	(-200; 0)	(-400; 0)

Table S6.

High-, low-, and band-pass filter characteristics during multiverse preprocessing. All filters used a Hamming window, a passband ripple of 0.0194 and a stopband attenuation of 53 dB. The filters were automatically determined by *MNE* based on low- and high-pass cutoffs in the respective forking path (first two columns). The bottom row shows the filter applied to the raw data prior to ICA.

Low-pass (Hz)	High-pass (Hz)	Filter type	Transition bandwidth (Hz)	-6 dB Cutoff frequency (Hz)	Filter length (samples)	Filter duration (s)
None	0.1	high-pass	0.1	0.05	8449	33.004
None	0.5	high-pass	0.5	0.25	1691	6.605
6	None	low-pass	2	7	423	1.652
6	0.1	band-pass	0.10 / 2.00	0.05 / 7.00	8449	33.004
6	0.5	band-pass	0.50 / 2.00	0.25 / 7.00	1691	6.605
30	None	low-pass	7.5	33.75	113	0.441
30	0.1	band-pass	0.10 / 7.50	0.05 / 33.75	8449	33.004
30	0.5	band-pass	0.50 / 7.50	0.25 / 33.75	1691	6.605
45	None	low-pass	11.25	50.62	77	0.301
45	0.1	band-pass	0.10 / 11.25	0.05 / 50.62	8449	33.004
45	0.5	band-pass	0.50 / 11.25	0.25 / 50.62	1691	6.605
Filter preceding ICA:						
None	1.0	high-pass	1.0	0.5	845	3.301

Table S7.
EEGNet hyperparameters.

name	value	default or manual
n_chans / in_chans	30	manual
n_outputs / n_classes	2	manual
n_times /	308	manual
input_window_samples		
final_conv_length	'auto'	
pool_mode	'mean'	
F1	8	default
D	2	default
F2	16	default
depthwise_kernel_length	16	default
pool1_kernel_size	4	default
pool2_kernel_size	8	default
kernel_length	64	default
conv_spatial_max_norm	1	default
activation	ELU	default
batch_norm_momentum	0.01	default
batch_norm_affine	True	default
batch_norm_eps	0.001	default
final_layer_with_constraint	False	default
norm_rate	0.25	default
drop_prob	0.25	
input_window_seconds	None	
sfreq	256	manual
max_epochs	200	manual
batch_size	16	manual
lr (learning rate)	0.01	default
optimizer	torch.optim.SGD	default
criterion	torch.nn.NLLLoss	default

Table S8.

EEGNet architecture. EEGNet was deployed for trials with length 1.2 s (308 samples) and 30 channels.

Layer	Input Shape	Output Shape	Param #	Kernel Shape
EEGNetv4 (EEGNetv4)	[1, 30, 308]	[1, 2]	--	--
├─ Ensure4d (ensuredims): 1-1	[1, 30, 308]	[1, 30, 308, 1]	--	--
├─ Rearrange (dimshuffle): 1-2	[1, 30, 308, 1]	[1, 1, 30, 308]	--	--
├─ Conv2d (conv_temporal): 1-3	[1, 1, 30, 308]	[1, 8, 30, 309]	512	[1, 64]
├─ BatchNorm2d (bnorm_temporal): 1-4	[1, 8, 30, 309]	[1, 8, 30, 309]	16	--
├─ Conv2dWithConstraint (conv_spatial): 1-5	[1, 8, 30, 309]	[1, 16, 1, 309]	480	[30, 1]
├─ BatchNorm2d (bnorm_1): 1-6	[1, 16, 1, 309]	[1, 16, 1, 309]	32	--
├─ Expression (elu_1): 1-7	[1, 16, 1, 309]	[1, 16, 1, 309]	--	--
├─ AvgPool2d (pool_1): 1-8	[1, 16, 1, 309]	[1, 16, 1, 77]	--	[1, 4]
├─ Dropout (drop_1): 1-9	[1, 16, 1, 77]	[1, 16, 1, 77]	--	--
├─ Conv2d (conv_separable_depth): 1-10	[1, 16, 1, 77]	[1, 16, 1, 78]	256	[1, 16]
├─ Conv2d (conv_separable_point): 1-11	[1, 16, 1, 78]	[1, 16, 1, 78]	256	[1, 1]
├─ BatchNorm2d (bnorm_2): 1-12	[1, 16, 1, 78]	[1, 16, 1, 78]	32	--
├─ Expression (elu_2): 1-13	[1, 16, 1, 78]	[1, 16, 1, 78]	--	--
├─ AvgPool2d (pool_2): 1-14	[1, 16, 1, 78]	[1, 16, 1, 9]	--	[1, 8]
├─ Dropout (drop_2): 1-15	[1, 16, 1, 9]	[1, 16, 1, 9]	--	--
├─ Sequential (final_layer): 1-16	[1, 16, 1, 9]	[1, 2]	--	--
│ ├─ Conv2d (conv_classifier): 2-1	[1, 16, 1, 9]	[1, 2, 1, 1]	290	[1, 9]
│ ├─ Rearrange (permute_back): 2-2	[1, 2, 1, 1]	[1, 2, 1, 1]	--	--
│ └─ Expression (squeeze): 2-3	[1, 2, 1, 1]	[1, 2]	--	--

Table S9.
Time-resolved logistic regression hyperparameters.

name	value	default or manual
C	1.0	default
class_weight	balanced	manual
penalty	L2	default
dual	False	default
tolerance	0.0001	default
solver	liblinear	manual
dual	False	default
fit_intercept	True	default
intercept_scaling	1	default
l1_ratio	None	default
max_iter	100	default
multi_class	auto	default
warm_start	False	default